JCI The Journal of Clinical Investigation

Laminar flow downregulates Notch activity to promote lymphatic sprouting

Dongwon Choi, … , Alex K. Wong, Young-Kwon Hong

J Clin Invest. 2017;127(4):1225-1240. https://doi.org/10.1172/JCI87442.

Research Article **Vascular biology**

The major function of the lymphatic system is to drain interstitial fluid from tissue. Functional drainage causes increased fluid flow that triggers lymphatic expansion, which is conceptually similar to hypoxia-triggered angiogenesis. Here, we have identified a mechanotransduction pathway that translates laminar flow–induced shear stress to activation of lymphatic sprouting. While low-rate laminar flow commonly induces the classic shear stress responses in blood endothelial cells and lymphatic endothelial cells (LECs), only LECs display reduced Notch activity and increased sprouting capacity. In response to flow, the plasma membrane calcium channel ORAI1 mediates calcium influx in LECs and activates calmodulin to facilitate a physical interaction between Krüppel-like factor 2 (KLF2), the major regulator of shear responses, and PROX1, the master regulator of lymphatic development. The PROX1/KLF2 complex upregulates the expression of *DTX1* and *DTX3L*. DTX1 and DTX3L, functioning as a heterodimeric Notch E3 ligase, concertedly downregulate NOTCH1 activity and enhance lymphatic sprouting. Notably, overexpression of the calcium reporter GCaMP3 unexpectedly inhibited lymphatic sprouting, presumably by disturbing calcium signaling. Endothelial-specific knockouts of *Orai1* and *Klf2* also markedly impaired lymphatic sprouting. Moreover, *Dtx3l* loss of function led to defective lymphatic sprouting, while *Dtx3l* gain of function rescued impaired sprouting in *Orai1* KO embryos. Together, the data reveal a molecular mechanism underlying laminar flow–induced lymphatic sprouting.

Laminar flow downregulates Notch activity to promote lymphatic sprouting

Dongwon Choi,[1] Eunkyung Park,[1] Eunson Jung,[1] Young Jin Seong,[1] Jaehyuk Yoo,[1] Esak Lee,[2] Mingu Hong,[1] Sunju Lee,[1] Hiroaki Ishida,[3] James Burford,[4] Janos Peti-Peterdi,[4] Ralf H. Adams,[5] Sonal Srikanth,[6] Yousang Gwack,[6] Christopher S. Chen,[2] Hans J. Vogel,[3] Chester J. Koh,[7] Alex K. Wong,[1] and Young-Kwon Hong[1]

[1]Division of Plastic and Reconstructive Surgery, Department of Surgery, Norris Comprehensive Cancer Center, Keck School of Medicine, University of Southern California, Los Angeles, California, USA. [2]Department of Biomedical Engineering and the Biological Design Center, Boston University; and Wyss Institute for Biologically Inspired Engineering, Harvard University, Boston, Massachusetts, USA. [3]Department of Biological Sciences, University of Calgary, Calgary, Alberta, Canada. [4]Department of Physiology and Biophysics, Zilkha Neurogenetic Institute, Keck School of Medicine, University of Southern California, Los Angeles, California, USA. [5]Max Planck Institute for Molecular Biomedicine, Department of Tissue Morphogenesis, and University of Münster, Faculty of Medicine, Münster, Germany. [6]Department of Physiology, David Geffen School of Medicine at UCLA, Los Angeles, California, USA. [7]Division of Pediatric Urology, Texas Children's Hospital, Baylor College of Medicine, Houston, Texas, USA.

The major function of the lymphatic system is to drain interstitial fluid from tissue. Functional drainage causes increased fluid flow that triggers lymphatic expansion, which is conceptually similar to hypoxia-triggered angiogenesis. Here, we have identified a mechanotransduction pathway that translates laminar flow–induced shear stress to activation of lymphatic sprouting. While low-rate laminar flow commonly induces the classic shear stress responses in blood endothelial cells and lymphatic endothelial cells (LECs), only LECs display reduced Notch activity and increased sprouting capacity. In response to flow, the plasma membrane calcium channel ORAI1 mediates calcium influx in LECs and activates calmodulin to facilitate a physical interaction between Krüppel-like factor 2 (KLF2), the major regulator of shear responses, and PROX1, the master regulator of lymphatic development. The PROX1/KLF2 complex upregulates the expression of *DTX1* and *DTX3L*. DTX1 and DTX3L, functioning as a heterodimeric Notch E3 ligase, concertedly downregulate NOTCH1 activity and enhance lymphatic sprouting. Notably, overexpression of the calcium reporter GCaMP3 unexpectedly inhibited lymphatic sprouting, presumably by disturbing calcium signaling. Endothelial-specific knockouts of *Orai1* and *Klf2* also markedly impaired lymphatic sprouting. Moreover, *Dtx3l* loss of function led to defective lymphatic sprouting, while *Dtx3l* gain of function rescued impaired sprouting in *Orai1* KO embryos. Together, the data reveal a molecular mechanism underlying laminar flow–induced lymphatic sprouting.

Introduction

The lymphatic system consists of lymphatic networks and lymphoid organs (1). Unlike the blood vascular system, where the fluid (blood) leaves and returns to the same organ (the heart), lymphatic vessels start from the tissue interstitium as capillary lymphatics, become the collectors, and eventually end at the venous connection as the thoracic duct, the biggest-caliber lymphatic vessel. While capillary lymphatics are composed of a single layer of overlapping lymphatic endothelial cells (LECs) and are devoid of mural cells and continuous basement membrane, collecting lymphatic vessels are equipped with luminal valves, as well as mural cells and basement membrane. Whereas LECs in lymphatic capillaries are expected to experience a basal-to-apical interstitial flow, followed by unidirectional laminar flow to downstream compartments, the cells in the collecting lymphatics are more likely exposed to oscillatory flow.

Blood vessels carry a relatively constant volume of blood and remain distended at normal steady state. Lymphatic capillaries, however, remain collapsed until a significant volume of interstitial fluid flows into the lumen. As tissue fluid drainage is a primary function of lymphatic vessels, fluid flow was hypothesized to serve as an important nonbiological lymphangiogenic stimulus (2). Indeed, the initial pioneering studies using in vivo models showed that interstitial fluid flow caused by functional drainage serves as a critical morphogenic mediator of lymphatic vessel organization by controlling LEC migration, VEGF-C expression, and lymphatic capillary network formation (3–5). An increase in embryonic fluid drainage was previously found to coincide with the initial lymphatic development and serve as a signal for embryonic lymphatic expansion (6). Lymph drainage and flow were also shown to regulate collecting lymphatic vessel maturation as well as luminal valve formation and development in vivo (7, 8). A recent study using a 3D in vitro biomimetic model showed that interstitial flow alone is sufficient to activate lymphatic sprouting, and that this mechanical force synergizes with biological stimuli to enhance lymphatic growth (9). Therefore, flow-induced mechanical signals, together with biological stimuli, seem to play critical roles in lymphatic growth, expansion, maturation, valve formation, and remodeling (10).

Studies have shown that steady laminar flow at a rate equivalent to blood flow (greater than ~10 dyn/cm^2) causes a variety of responses in blood vessel endothelial cells (BECs), including elongated cell morphology, cell proliferation arrest, increased

Conflict of interest: The authors have declared that no conflict of interest exists.
Submitted: March 9, 2016; **Accepted:** January 11, 2017.
Reference information: *J Clin Invest*. 2017;127(4):1225–1240.
https://doi.org/10.1172/JCI87442.

calcium entry, Notch activation, and upregulation of Krüppel-like factor 2 (KLF2), the master regulator of the shear stress response (11–17). Moreover, fluid shear stress can promote endothelial differentiation of bone marrow–derived progenitor cells and embryonic stem cells in vitro (16). Similarly, blood flow reprograms lymphatic vessels to blood vessels in mice (18). Thus, it is clear that fluid flow has a substantial effect on establishment and maintenance of the blood vascular system. In comparison, the molecular basis of functional drainage-induced lymphatic expansion remains undefined. In this study, we aimed to gain a mechanistic understanding of how the flow functions as a growth stimulus for lymphatic vessels during development. Our data show that laminar flow activates ORAI1, a major component of the calcium release–activated calcium (CRAC) channel, and results in calcium influx in LECs. Increased intracellular calcium, in turn, activates calmodulin (CaM) to promote a complex formation between a key shear stress regulator, KLF2, and the master regulator of lymphatic development, PROX1. The resulting KLF2/PROX1/Ca^{2+}-CaM protein complex upregulates a heterodimeric Notch E3 ligase, encoded by *Dtx1* (deltex E3 ubiquitin ligase 1) and *Dtx3l* (deltex E3 ubiquitin ligase 3L), which activates lymphatic sprouting through suppression of Notch activity. Together, our findings uncover a molecular mechanism underlying the laminar flow–induced lymphatic expansion.

Results

Laminar flow selectively suppresses NOTCH activity in LECs and increases lymphatic sprouting. We aimed to study the impact of low-rate laminar flow generated from functional lymphatic drainage on lymphatic development. Currently, the shear force levels in the developing embryonic lymphatic network are unknown. Thus, we applied various levels of laminar shear force on cultured LECs and found that steady laminar flow at approximately 2 dyn/cm^2 or higher clearly and consistently generated the classic endothelial shear stress responses, such as elongated cell morphology, upregulation of KLF2 and endothelial NOS, and calcium influx (Figure 1A; Supplemental Figure 1, A and B, and Supplemental Figure 2, A and B; supplemental material available online with this article; doi:10.1172/JCI87442DS1). Unexpectedly, the laminar flow at this shear force caused downregulation of the NOTCH target genes *NRARP*, *HEY1*, and *HEY2* in LECs (Figure 1B). BECs, in comparison, did not show the same regulation of the Notch pathway (Supplemental Figure 1C), possibly because the applied shear force (~2 dyn/cm^2) was much lower than the physiological levels in blood vessels (10–20 dyn/cm^2). Moreover, whereas the mRNA level of *NOTCH1* was not altered (Supplemental Figure 1D), the protein level of the NOTCH1 intracellular domain (NICD1) was significantly reduced in LECs, but not in BECs, by the laminar flow (Figure 1C and Supplemental Figure 1E). In comparison, NICD4 protein level was not changed in either cell type by laminar flow (Supplemental Figure 1, F and G). Consistent with these findings, a Notch activity reporter assay using an RBP-JK–responsive luciferase vector confirmed that the steady laminar flow decreased Notch activity in LECs (Figure 1D). Notably, the PROX1 protein level was not changed by this experimental condition (Supplemental Figure 1H), although a higher flow rate (20 dyn/cm^2) downregulated PROX1 with loss of the LEC identity (18).

Because Notch activity has been shown to be a key regulator of lymphatic sprouting (19–23), we next evaluated the effect of the low-rate laminar flow on the in vitro sprouting potential of LECs by spheroid-based sprouting and microfluidic vascular mimetic assays (24–27). In spheroid-based sprouting assays (24, 25), flow-exposed LECs displayed increased sprout-forming capacity, whereas the same treatment in BECs did not show the same phenotype (Figure 1E). We next created a 3D vascular mimetic model by lining microfluidic channels with single-donor-derived BECs and LECs and subsequently subjected them to steady intraluminal laminar flow (26, 27). Consistent with the spheroid-based sprouting assays, laminar flow strongly enhanced LEC sprouting, but did not induce the same response in BECs (Figure 1F and Supplemental Figure 1I). These data show that although LECs and BECs similarly exhibit the conventional shear stress responses to the low-rate steady laminar flow, only LECs increase their sprouting capability by suppressing Notch.

Calcium influx through ORAI1 is essential for the laminar flow–induced suppression of Notch activity and enhanced sprouting in LECs. As intracellular calcium mobilization is a hallmark immediate response to shear stress in endothelial cells, we next studied the dynamics of laminar flow–induced calcium influx in LECs. The calcium signal was activated in LECs within the first minute of the onset of laminar flow, after which it gradually decreased despite the continuous presence of laminar flow (Figure 2, A and B), consistent with a previous study (28). Since the calcium channel responsible for the flow-induced intracellular calcium increase has not been identified in LECs, we searched for the key calcium channel protein that may control the downstream shear stress responses in LECs, particularly Notch downregulation. Our search found that inhibition of store-operated calcium entry (SOCE) (29) with low concentrations of SKF-96365 (a nonspecific inhibitor of SOCE) could efficiently block the laminar flow–induced calcium mobilization in LECs (Figure 2, A and B). More specifically, when we knocked down ORAI1, a pore subunit of the CRAC channel that is involved in the SOCE process (30), the flow-mediated reduction of NICD1 as well as the increased calcium influx in LECs was completely abrogated (Figure 2C and Supplemental Figure 2), suggesting that ORAI1 is responsible for the laminar flow–induced calcium mobilization and NOTCH1 downregulation in LECs. Moreover, ORAI1 knockdown also significantly reversed the flow-induced downregulation of Notch pathway genes in LECs, but did not yield any effects in BECs (Figure 2D). In addition, ORAI1 knockdown abolished the in vitro sprouting capacity of LECs stimulated by laminar flow, while not altering BEC sprouting (Figure 2E). These data imply that ORAI1, responsible for the laminar flow–induced calcium entry, is essential for the NOTCH1 suppression and enhanced sprouting in LECs.

ORAI1 function is required for lymphatic sprouting during development. We next investigated the vascular phenotypes in *Orai1* KO mice (31). Conventional *Orai1* KO embryos and rarely surviving postnatal mice displayed abnormally enlarged lymphatic vessels with reduced number of sprouts and branches in their back skins and ears, respectively (Figure 3, A and B, and Supplemental Figure 3). Morphometric analyses revealed that *Orai1* knockout caused defective lymphatic development, characterized by reduced number (~50%) of lymphatic branching points and increased distance

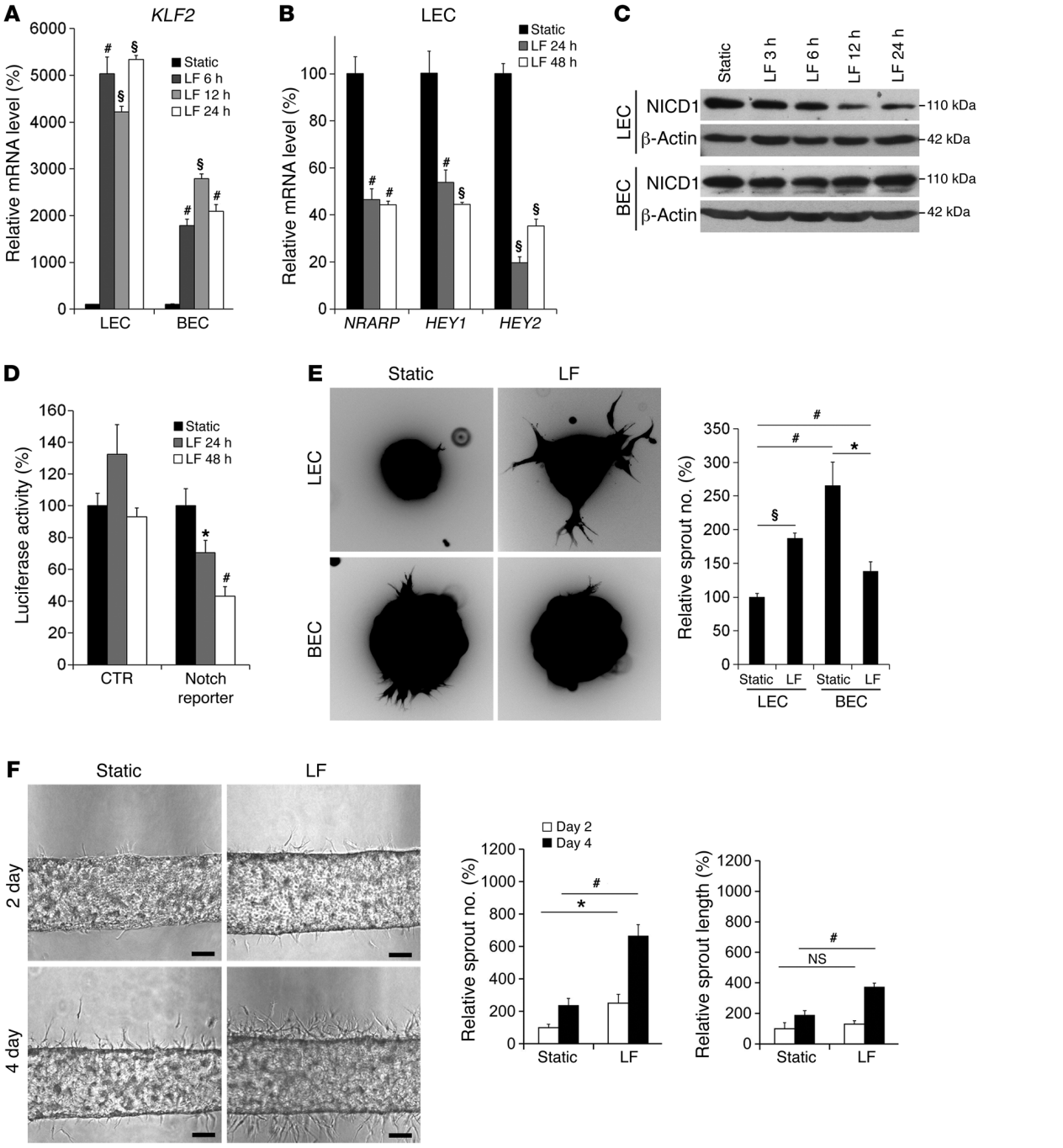

Figure 1. Laminar flow selectively suppresses NOTCH1 activity in LECs. (**A** and **B**) Real-time quantitative reverse transcription PCR (qRT-PCR) data showing the mRNA levels of *KLF2* in LECs and BECs (**A**) and those of Notch target genes in LECs (**B**) in response to steady laminar flow (2 dyn/cm^2). Expression of the Notch target genes in BECs by laminar flow is shown in Supplemental Figure 1C. (**C**) Protein levels of NICD1 in LECs and BECs in response to laminar flow (2 dyn/cm^2). The intensity of the Western blotting bands is quantitated in Supplemental Figure 1E. A monoclonal anti-NOTCH1 antibody that specifically detects the cleaved form of NOTCH1 at Val1744 was used. Blots presented are derived from replicate samples run on parallel gels. (**D**) Luciferase assay showing the flow-mediated suppression of Notch activity in LECs. LECs were transfected with a Notch activity reporter (pGa981-6) (60) and exposed to laminar flow (2 dyn/cm^2) for 24 or 48 hours before measurement of luciferase activity. (**E**) Spheroid-based sprouting assays. Cells were exposed or not exposed to laminar flow (2 dyn/cm^2) for 24 hours, stained with a CellTracker dye, aggregated in methylcellulose polymers, and then embedded in Matrigel. After 24 hours, images of more than 20 spheroids were taken for analyses, and relative sprout numbers were quantified in the graph. (**F**) Biomimetic sprouting assay. Intraluminal laminar flow (5 dyn/cm^2) was applied onto a layer of LECs lining the inner wall of the vascular mimetic channels made in collagen gel. Scale bars: 100 μm. Relative sprout length and number were graphed. Each experiment was independently performed at least 3 times with consistent results. Data are expressed as SEM and SD from 1 representative data set. $^*P < 0.05$; $^\#P < 0.01$; $^\S P < 0.001$; *t* test.

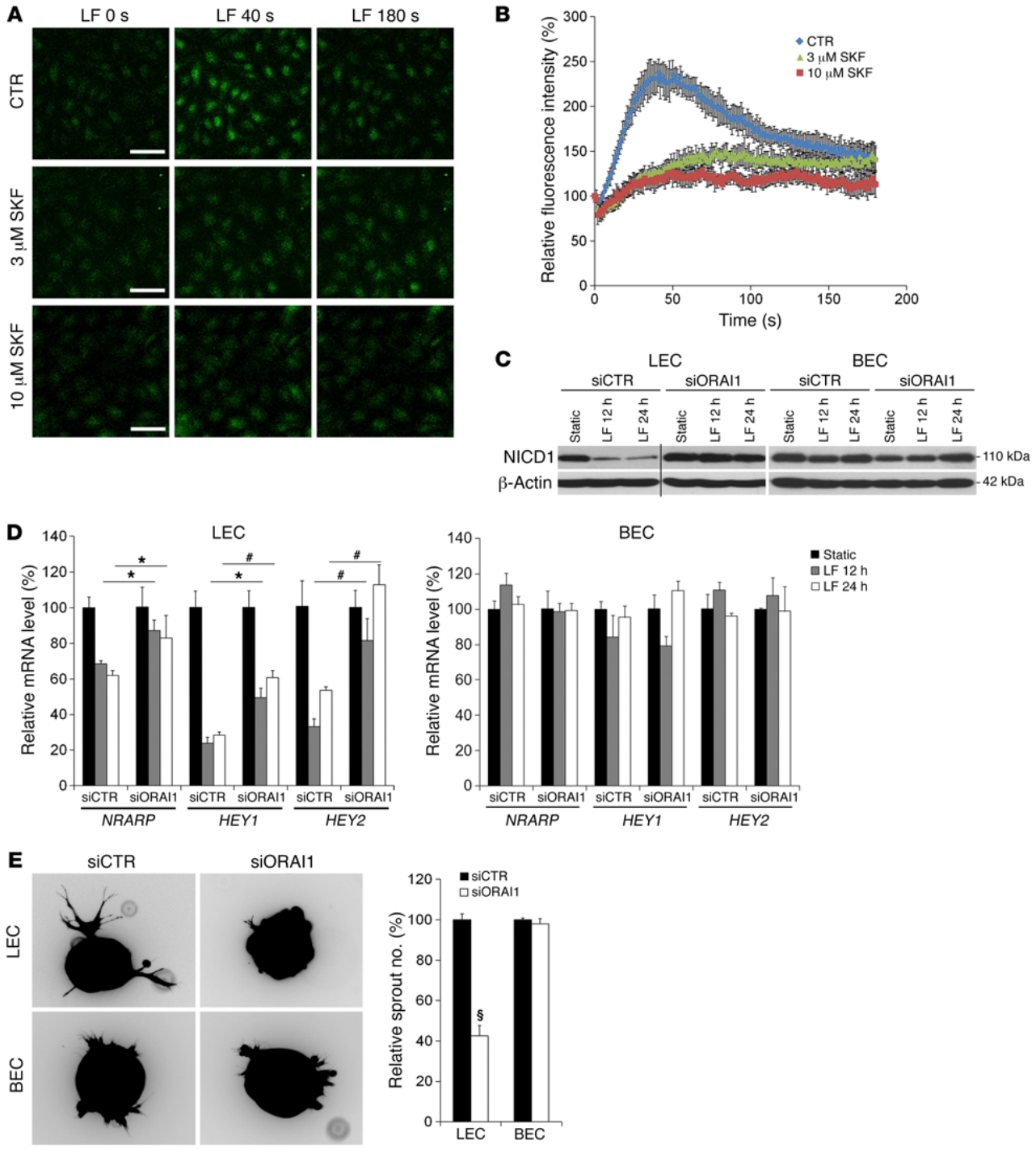

Figure 2. ORAI1 is essential for the laminar flow–induced NOTCH1 suppression in LECs. (**A** and **B**) Activation of Ca^{2+} mobilization in LECs by laminar flow: Fluo-4–loaded LECs were pretreated with PBS (CTR) or SKF-96365 (SKF), an inhibitor of store-operated Ca^{2+} entry (SOCE), for 10 minutes, and subjected to laminar flow (2 dyn/cm^2). Calcium signals were captured by a time-lapse microscope (**A**). Relative signal intensity was plotted in the graph (**B**). (**C**) NICD1 protein level in LECs and BECs that were transfected with control siRNA (siCTR) or ORAI1 siRNA (siORAI1) for 24 hours, then subjected to laminar flow (2 dyn/cm^2). The vertical line marks a boundary between 2 different areas in the same gel. Blots presented are derived from replicate samples run on parallel gels. (**D**) qRT-PCR data showing the mRNA level of *NRARP*, *HEY1*, and *HEY2* in ORAI1-inhibited LECs and BECs. Statistical comparison was made between control siRNA and ORAI1 siRNA samples at each time point to assess the reversal of the laminar flow–mediated suppression of the genes. (**E**) Effect of ORAI1 knockdown on the flow-induced sprouting of LECs and BECs. Cells were transfected with control or ORAI1 siRNA for 24 hours, exposed to laminar flow (2 dyn/cm^2) for 24 hours, stained with a CellTracker dye, aggregated in methylcellulose polymers, and embedded in Matrigel. After 24 hours, spheroid images (>20) were taken and relative sprout numbers were quantified by NIH ImageJ. Scale bars: 50 μm. Data are expressed as SEM and SD of a representative of 3 independent experiments. $^*P < 0.05$; $^\#P < 0.01$; $^\S P < 0.001$; *t* test.

(1.5- to 2-fold) between the branching points in the lymphatic networks. In contrast, blood vessels in *Orai1* KO embryos and adults exhibited slightly denser vascular networks with increased number of branching points and marginally reduced distance between the branching points. These vascular patterning phenotypes were also observed in endothelial-specific, inducible *Orai1* KO embryos (referred to hereafter as *Orai1*^{ECKO}). Mice with floxed *Orai1* alleles (*Orai1*$^{fl/fl}$) were crossed with *Prox1-EGFP* lymphatic reporter mice (32) and *Cdh5(PAC)-CreER*^{T2} (also known as VE-Cadherin-*CreER*^{T2}) mice (33) expressing the tamoxifen-responsive Cre in endothelial cells. *Orai1*^{ECKO} was induced by tamoxifen injection into pregnant female mice at E11.5 and E13.5. At E15.5, dermal lymphatics of *Orai1*^{ECKO} embryos revealed a reduced number of lymphatic sprouts, and round/dull lymphatic tips that appeared less invasive. WT embryos, by comparison, showed growing lymphatic tips with jagged and sharp ends (Figure 3, C and E). Dermal blood vessels in *Orai1*^{ECKO} embryos displayed a higher vascular density than that of WT embryos (Figure 3, D and E). Taking these results together, genetic ablation of *Orai1* results in decreased lymphatic sprouting in animal models, suggesting the essential role of *Orai1* in lymphatic development.

Calcium signal activates CaM to interact with PROX1. We next investigated how the flow-induced calcium influx through ORAI1 causes the LEC-specific shear stress phenotypes, in particular NICD1 downregulation. Seeking initial insights into this question, we asked what LEC-specific molecules could be affected in their functions by calcium signaling. Interestingly, our bioinformatics-based screening discovered that PROX1, the master regulator of lymphatic differentiation and development (34), contains a high-probability CaM-binding site in its N-terminal region (Supplemental Figure 4A) and suggested a possible physical interaction between PROX1 and CaM proteins. We therefore generated an array of recombinant GST-PROX1 fusion fragments (Supplemental Figure 4B), and performed the CaM overlay assays (35) to evaluate the protein/protein interaction between PROX1 fragments and CaM. Indeed, the PROX1 D1 fragment, spanning from the first to the 168th amino acid of PROX1, displayed a strong binding affinity to CaM in the presence of calcium, but this interaction was abolished by a calcium chelator, EGTA (Figure 4A). We generated a panel of PROX1 substitution mutants by replacing the nonpolar/hydrophobic amino acid residues in the predicted CaM-binding region (aa 14–35) with a polar/charged residue, aspartic acid (Figure 4B). We performed the CaM overlay assay using these substitution mutant fragments, and found that the V23D and V27D mutations abolished the PROX1/CaM interaction (Figure 4C), indicating the essential role of Val23 and Val27 in the interaction between PROX1 and CaM.

To identify the PROX1 binding region in CaM protein, we performed high-resolution NMR spectroscopy on the interaction between the Ca^{2+}/CaM protein and a PROX1 peptide (aa 15–35). Addition of the PROX1 peptide into ^{15}N-labeled CaM caused large chemical shift changes for signals from the N-terminal domain (e.g., I27, T29, A57, and D64; slow exchange) in the ^{1}H,^{15}N heteronuclear single quantum coherence NMR spectra (Figure 4D). In comparison, much smaller chemical shift perturbations were seen for the C-terminal domain (e.g., I100, I130, and N137; fast exchange), indicating that Ca^{2+}/CaM interacts with the PROX1 peptide mainly through its N-terminal region. To further confirm these biochemical data, we performed a series of co-immunoprecipitation (co-IP) assays for FLAG-tagged PROX1 and HA-tagged CaM proteins that were coexpressed in HEK293 cells with or without altering effective calcium concentration. These assays revealed that PROX1 could be coprecipitated with CaM, and also that the PROX1/CaM interaction could be inhibited by Bapta-AM (calcium chelator), but promoted by ionomycin (Ca^{2+} ionophore) and KCl (Ca^{2+} influx inducer) (Figure 4E and Supplemental Figure 5A). In addition, we also carried out co-IP assays for endogenous PROX1 and CaM proteins in LECs that were pre-exposed to laminar flow. This study found that the PROX1/CaM interaction was significantly increased (~7-fold) in LECs by steady laminar flow, and that the increased interaction could be significantly reversed by Bapta-AM (~3.5-fold) (Figure 4F and Supplemental Figure 5B).

We next investigated the impact of CaM overexpression on lymphatic sprouting using the GCaMP3 calcium reporter mouse. GCaMP3, a fusion protein of CaM and GFP, was originally developed as a calcium reporter. The GCaMP3 reporter mouse has been widely used as an animal model for live imaging of in vivo calcium dynamics (36). However, modifying its original purpose, we used the GCaMP3 reporter mouse as a transgenic model that conditionally overexpresses CaM in order to study the impact of overly expressed CaM protein on lymphangiogenesis. We first confirmed that PROX1 interacts with GCaMP3 through the CaM sequences (Supplemental Figure 6). Indeed, when GCaMP3 was conditionally overexpressed in *Tie2*- and *Prox1*-expressing cells during embryogenesis using *Tie2-Cre* and *Prox1-CreER*^{T2}, respectively, GCaMP3 overexpression unexpectedly caused extremely enlarged, abnormal lymphatic vessels with severely reduced branches (Figure 4G). We speculate that these surprising gain-of-function lymphatic phenotypes may be caused by disturbed calcium signaling due to an excessive expression of GCaMP3 in LECs. In summary, PROX1 physically interacts with CaM in a calcium-dependent manner, and the PROX1/CaM interaction is dramatically enhanced by the steady laminar flow. Furthermore, ectopic overexpression of CaM causes abnormally enlarged lymphatic vessels with defective branching morphogenesis.

CaM promotes a complex formation between PROX1 and KLF2 in a calcium-dependent manner. From our separate effort to find PROX1-interacting proteins, we fortuitously identified KLF2 as a PROX1 binding protein (Figure 5A). Because KLF2 is the master regulator for shear stress responses (37) and is dramatically upregulated by steady laminar flow in LECs (Figure 1A), we asked whether KLF2 may be involved in the flow-induced Notch downregulation. Supporting this notion, the PROX1/KLF2 interaction was decreased by calcium chelation, but enhanced by ionomycin, in HEK293T cells (Figure 5B and Supplemental Figure 5C), indicating the dependence of the PROX1/KLF2 interaction on the presence of calcium. Moreover, the PROX1/KLF2 interaction was enhanced by ectopic expression of HA-tagged CaM (Figure 5C and Supplemental Figure 5D). Although endogenous CaM proteins may be abundantly present in the cells, an additional expression of CaM could further enhance the PROX1/KLF2 interaction.

These data raised a possibility that CaM may facilitate the interaction between PROX1 and KLF2 and form a triple protein complex in the presence of increased intracellular calcium. In

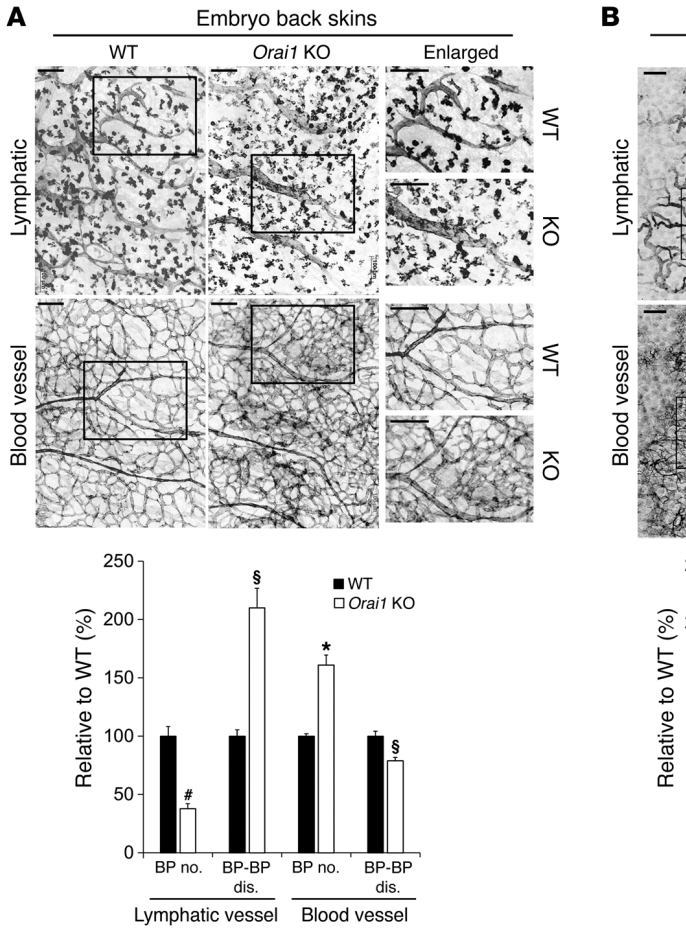

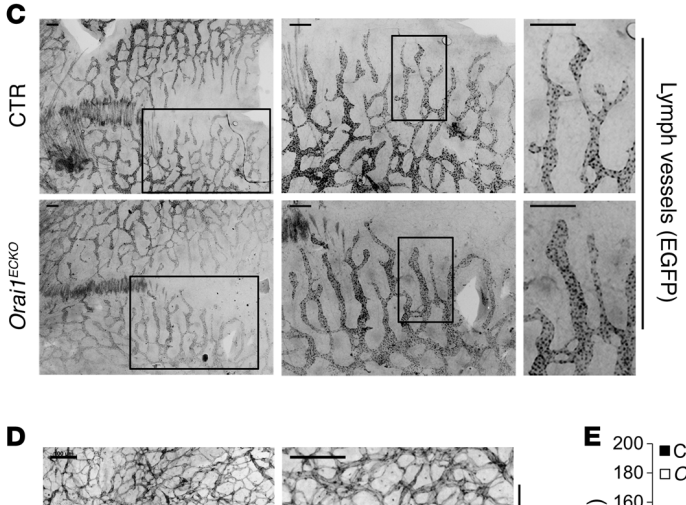

Figure 3. ORAI1 is required for normal lymphatic sprouting during development. (**A**) Immunofluorescence images of lymphatic and blood vessels in the back skins of WT and *Orai1* KO embryos (E15.5). Lymphatics were stained for LYVE-1, and blood vessels were visualized by anti-CD31 staining. The graph shows the relative number of branching points (BP no.) and average distance between the branching points (BP-BP dis.). Scale bars: 100 μm. (**B**) The ear vasculature of 3-week-old WT and *Orai1* KO mice was similarly visualized and analyzed. Scale bars: 250 μm. (**C**–**E**) Endothelial-specific deletion of *Orai1* (*Orai1*^{ECKO}) was induced in pregnant females by peritoneal injection of tamoxifen (1.5 mg) at E11.5 and 13.5. At E15.5, the embryos were harvested and genotyped. Lymphatics and blood vessels of the back skins of the control (CTR) embryos [*Orai1*$^{+/+}$ *Cdh5(Pac)-CreER*^{T2} *Prox1-EGFP*] and *Orai1*^{ECKO} embryos [*Orai1*$^{fl/fl}$ *Cdh5(Pac)-CreER*^{T2} *Prox1-EGFP*] were visualized by lymphatic-specific EGFP signals (**C**) and anti-CD31 staining (**D**), respectively. Scale bars: 250 μm (**C**), 100 μm (**D**). (**E**) Vascular analyses were performed as described above. For all studies, a total of more than 6 embryos or postnatal mice per genotype collected from at least 3 independent litters were analyzed. The dorsal midline areas of the embryos were chosen as the sites for vascular analyses. Data are expressed as SEM and SD. $^{*}P < 0.05$; $^{\#}P < 0.01$; $^{\S}P < 0.001$.

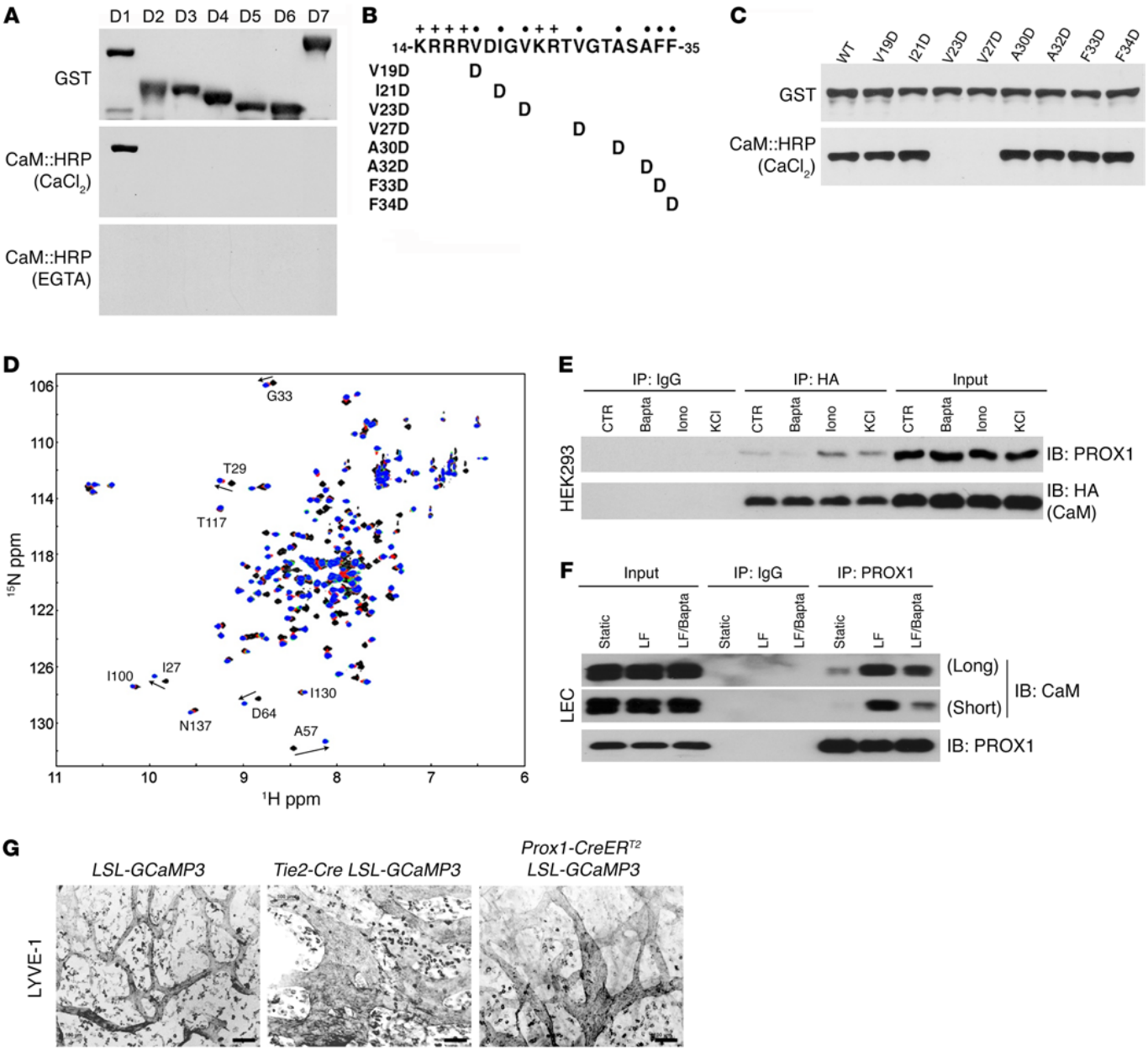

Figure 4. CaM physically interacts with PROX1 and regulates lymphatic sprouting. (**A**) CaM overlay assays. Top: Western analysis showing the quantity and quality of recombinant GST-PROX1 fragments (D1–D7; Supplemental Figure 4B). Middle and bottom: CaM overlay assays were performed on duplicate blots using the CaM::HRP conjugate protein in the presence of $CaCl_2$ (1 mM, middle) or EGTA (5 mM, bottom). (**B**) Substitution mutations in the predicted CaM-binding site of PROX1: uncharged residues (V19, I21, V23, V27, A30, A32, F33, and F34) were replaced with aspartic acid, D. (**C**) CaM overlay assays performed against the PROX1 mutant fragments identified 2 residues (V23, V27) as essential for the CaM/PROX1 binding. (**D**) Superposed ^{1}H,^{15}N heteronuclear single quantum coherence spectra of Ca^{2+}-saturated CaM recorded with 0 (black), 0.5 (red), 1.0 (green), and 1.5 (blue) molar equivalents of PROX1 peptide (aa 15–35). The assignments for separated signals are shown. Signals from the N-domain of CaM were perturbed in slow exchange on the NMR timescale, whereas the perturbations of the signals from the C-domain were relatively small and in fast exchange. (**E**) Co-IP assay demonstrating calcium-dependent interaction of PROX1 and CaM. HEK293 cells were transfected with vectors expressing FLAG-tagged PROX1 and/or HA-tagged CaM, treated with Bapta-AM (Bapta, 3 μM), ionomycin (Iono, 1 μM), and KCl (40 mM), and co-IP was performed. Band intensity is quantitated in Supplemental Figure 5A. (**F**) Co-IP assay demonstrating that laminar flow (LF, 2 dyne/cm^2) enhanced the interaction between PROX1 and CaM in LECs. LECs were treated with Bapta-AM (3 μM, Bapta) for 10 minutes, followed by laminar flow for 4 hours. Two CaM blots from a short or long exposure are shown. Band intensity is quantitated in Supplemental Figure 5B. (**G**) Whole-mount LYVE-1 staining of the back skin of embryos (E15.5) having *LSL-GCaMP3*, *Tie2-Cre LSL-GCaMP3*, or *Prox1-CreER^{T2} LSL-GCaMP3* transgenes. Pregnant mice were injected i.p. with tamoxifen (1.5 mg) at E11.5 and E13.5, and the embryos of each genotype were harvested at E15.5 for lymphatic analyses. More than 5 embryos total per genotype collected from at least 3 independent litters were analyzed. Scale bars: 100 μm. For in vitro experiments, data are expressed as SEM and SD from a representative of 3 independent experiments.

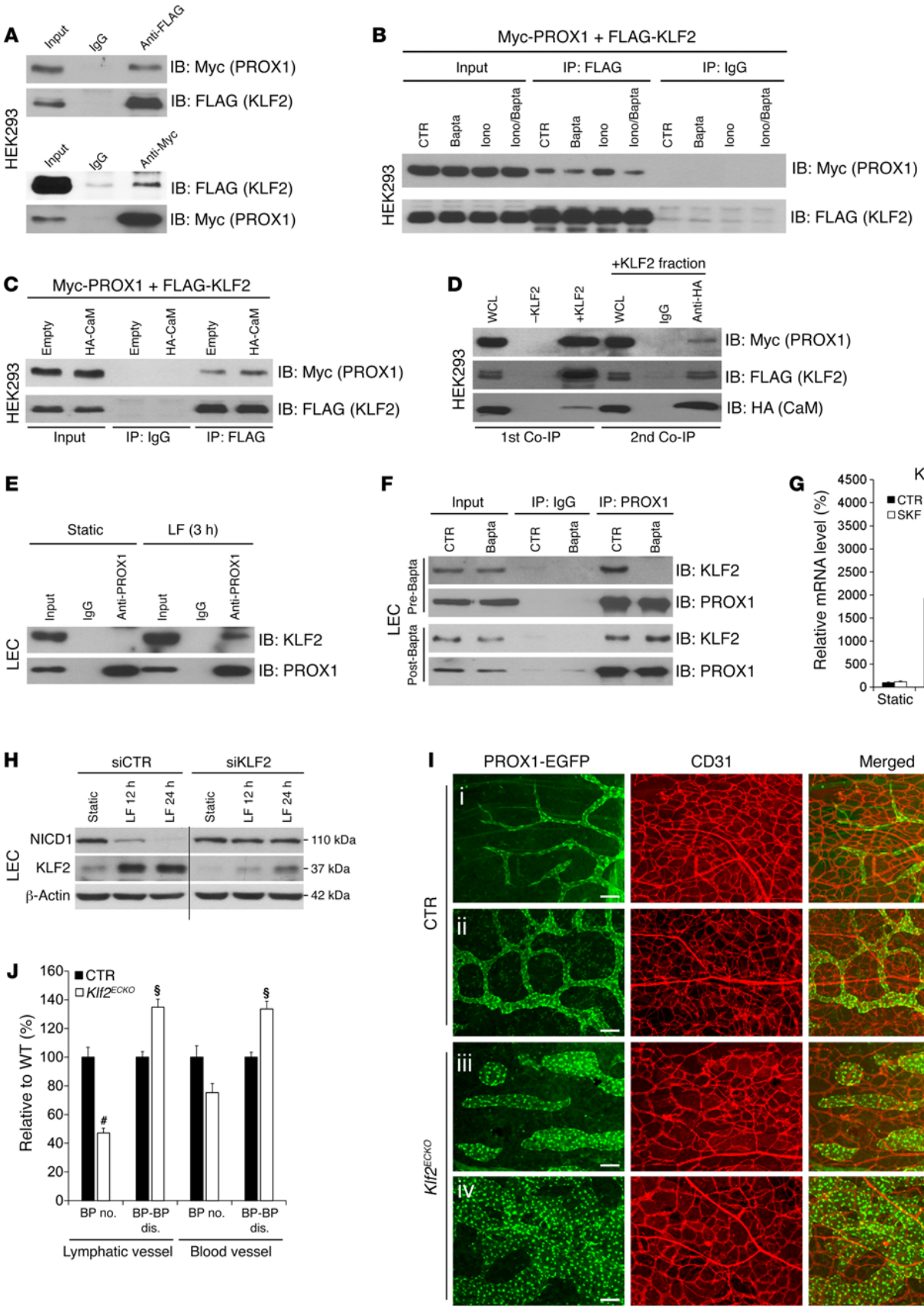
A
Input
IgG
Anti-FLAG
IB: Myc (PROX1)
IB: FLAG (KLF2)
HEK293
Input
IgG
Anti-Myc
IB: FLAG (KLF2)
IB: Myc (PROX1)
B
Myc-PROX1 + FLAG-KLF2
Input
IP: FLAG
IP: IgG
CTR
Bapta
Iono
Iono/Bapta
HEK293
IB: Myc (PROX1)
IB: FLAG (KLF2)
C
Myc-PROX1 + FLAG-KLF2
Empty
HA-CaM
HEK293
IB: Myc (PROX1)
IB: FLAG (KLF2)
Input
IP: IgG
IP: FLAG
D
+KLF2 fraction
WCL
−KLF2
+KLF2
IgG
Anti-HA
HEK293
IB: Myc (PROX1)
IB: FLAG (KLF2)
IB: HA (CaM)
1st Co-IP
2nd Co-IP
E
Static
LF (3 h)
Input
IgG
Anti-PROX1
LEC
IB: KLF2
IB: PROX1
F
Input
IP: IgG
IP: PROX1
CTR
Bapta
Pre-Bapta
Post-Bapta
LEC
IB: KLF2
IB: PROX1
G
KLF2
CTR
SKF
Relative mRNA level (%)
4500
4000
3500
3000
2500
2000
1500
1000
500
0
Static
12 h
24 h
LF
H
siCTR
siKLF2
Static
LF 12 h
LF 24 h
NICD1
KLF2
β-Actin
LEC
110 kDa
37 kDa
42 kDa
I
PROX1-EGFP
CD31
Merged
CTR
Klf2ECKO
i
ii
iii
iv
J
CTR
Klf2ECKO
Relative to WT (%)
160
140
120
100
80
60
40
20
0
BP no.
BP-BP dis.
BP no.
BP-BP dis.
Lymphatic vessel
Blood vessel

Figure 5. KLF2 forms a complex with PROX1 and CaM, and is required for lymphatic sprouting. (**A**) FLAG-KLF2 and/or Myc-PROX1 were expressed in HEK293 cells, and co-IP assays were performed using anti-FLAG (top panel) or anti-Myc antibody (bottom panel). (**B**) Co-IP assays were performed against FLAG-KLF2 and Myc-PROX1 in HEK293 cells in the presence of DMSO (CTR), Bapta-AM (Bapta, 10 μM), ionomycin (Iono, 1 μM), or Bapta-AM (10 μM)/ionomycin (1 μM). (**C**) CaM promotes PROX1/KLF2 interaction. FLAG-KLF2 and Myc-PROX1 were expressed in HEK293 cells with CaM (HA-CaM) or not (Empty). Co-IP was performed using IgG or anti-FLAG antibody. (**D**) Serial Co-IP assays showing a protein complex formation among KLF2, PROX1, and CaM. These 3 proteins were expressed in HEK293 cells and first immunoprecipitated using FLAG-antibody beads (1st Co-IP) and then using anti-HA antibody (2nd Co-IP) for final immunodetection of Myc-PROX1. See details in Supplemental Information. (**E**) LECs were cultured under static or laminar flow (2 dyn/cm^2), and co-IP assays were performed using IgG or anti-PROX1 antibody, followed by immunoblotting against KLF2 or PROX1. (**F**) Effect of calcium chelation on PROX1/KLF2 complex formation. (Pre-Bapta) LECs were pretreated with Bapta-AM (10 μM) for 10 minutes and exposed to laminar flow (2 dyn/cm^2) for 24 hours before co-IP assay. (Post-Bapta) LECs were exposed to laminar flow for 0.5 hours, treated with Bapta-AM (10 μM), and subjected to laminar flow (2 dyn/cm^2) for an additional 0.5 hours before co-IP assay. (**G**) qRT-PCR analyses showing that ORAI1 inhibition by SKF-96365 (SKF, 3 μM) reduced the flow-induced *KLF2* upregulation in LECs. (**H**) Western blot assays showing protein levels of KLF2, NICD1, and β-actin in LECs, which were transfected with scrambled siRNA (siCTR) or KLF2 siRNA (siKLF2) and exposed to laminar flow (2 dyne/cm^2). A vertical line marks spliced lanes. (**I** and **J**) Lymphatic and blood vessels of the back skins of control (CTR) embryos [*Cdh5(PAC)-CreER^{T2} Klf2$^{+/+}$ Prox1-EGFP*] and *Klf2^{ECKO}* embryos [*Cdh5(PAC)-CreER^{T2} Klf2$^{fl/fl}$ Prox1-EGFP*] were visualized by lymphatic-specific EGFP signal and CD31 immunostaining, respectively, at E15.5. Equivalent anatomic locations were chosen for i and iii, and for ii and iv. Scale bars: 100 μm. (**J**) Vascular analyses were performed and graphed. Data are expressed as SEM and SD of a representative of 3 independent experiments. $^*P < 0.05$; $^{\#}P < 0.01$; $^{\S}P < 0.001$.

order to address this hypothesis, we asked whether these 3 proteins can be found in a complex at the same time, and thus performed a serial co-IP assay. Myc-PROX1, FLAG-KLF2, and HA-CaM were expressed in HEK293 cells. A negative control was also prepared without FLAG-KLF2. We first set up an immunoprecipitation of the KLF2-containing complexes from both cell lysates. From the KLF2 precipitates obtained from the KLF2-expressing cells, we next performed an immunoprecipitation of CaM protein. In this serially precipitated CaM-containing protein complex, we checked the presence or absence of PROX1 protein by Western blotting for PROX1 (Figure 5D). Indeed, PROX1 protein was found in the protein complex that was immunoprecipitated sequentially by KLF2 and CaM, suggesting that the 3 proteins form a stable multiprotein complex. Notably, the PROX1/KLF2 interaction was undetectable in the statically cultured LECs, but was strongly enhanced in LECs that were pre-exposed to laminar flow for 3 hours (Figure 5E). Importantly, calcium was required for the initial formation, but not for the maintenance, of the PROX1/KLF2 complex by laminar flow, because pretreatment of LECs with Bapta-AM prior to the onset of fluid flow efficiently blocked the flow-induced formation of the complex, whereas treatment of LECs after laminar flow exposure did not disrupt the already formed complex (Figure 5F). In sum, these studies suggest that laminar flow activates KLF2, PROX1, and CaM proteins to form a multiprotein complex in LECs in a calcium-dependent manner.

KLF2 is essential for flow-induced NICD1 downregulation and lymphatic sprouting. Moreover, chemical inhibition of ORAI1 significantly suppressed the laminar flow–induced KLF2 upregulation in LECs (Figure 5G). In turn, when the flow-induced KLF2 expression was inhibited by siRNA-mediated knockdown in LECs, the laminar flow could no longer decrease the NICD1 protein level, indicating the essential role of KLF2 in the flow-mediated downregulation of NOTCH1 (Figure 5H). We next studied the in vivo effect of KLF2 inhibition on lymphatic development by inducing endothelial-specific knockout of *Klf2* (*Klf2^{ECKO}*). For this, we intercrossed *Cdh5(PAC)-CreER^{T2}* mice (33), *Klf2$^{fl/fl}$* mice (38), and *Prox1-EGFP* mice (32), and then compared the developing vascular phenotypes between the control embryos [*Cdh5(PAC)-CreER^{T2} Klf2$^{+/+}$ Prox1-EGFP*] and *Klf2^{ECKO}* embryos [*Cdh5(PAC)-CreER^{T2} Klf2$^{fl/fl}$ Prox1-EGFP*]. Indeed, the majority of *Klf2^{ECKO}* embryos (E15.5, $n > 6$) developed severe nuchal edema, often displaying blood-filled lymphatics (Supplemental Figure 7). *Klf2^{ECKO}* embryos displayed profoundly enlarged lymphatic vessels and impaired lymphatic sprouting, determined by a reduced number of branching points and an increased distance between the branching points, compared with WT controls (Figure 5, I and J, and Supplemental Figure 8). Together, our data show that *Klf2* is required for the laminar flow to downregulate NICD1, and also that KLF2 ablation causes abnormally enlarged lymphatic vessels with defective lymphatic sprouting.

PROX1/KLF2 selectively suppresses Notch by upregulation of DTX1 and DTX3L in LECs. The finding of LEC-specific suppression of Notch activity directed us to hypothesize that there may be Notch activity modifiers acting selectively in LECs. We thus searched for putative modifiers that were differentially expressed in LECs and BECs under the laminar flow conditions. DTX1 and DTX3L were identified from our transcriptional profiling analyses as the candidates based on their previous association with Notch signaling as a heterodimeric E3 ligase (39–42). While *DTX3L* mRNA was upregulated specifically in LECs in response to laminar flow, *DTX1* mRNA was commonly upregulated in LECs and BECs (Figure 6, A and B). This finding was also confirmed by the protein levels (Supplemental Figure 9). ChIP assays revealed that PROX1 and KLF2 proteins were physically associated with the promoters of the *DTX1* and *DTX3L* genes, and that their promoter occupancies were significantly increased by laminar flow. Notably, these flow-increased promoter occupancies were reversed by an inhibitor of SOCE (SKF-96365) (Figure 6, C and D), indicating that the flow-induced bindings of PROX1 and KLF2 to the promoters of *DTX1* and *DTX3L* are dependent on ORAI1 function. Functionally, DTX1 and DTX3L proteins were found to synergistically reduce the endogenous NICD1 level in HEK293 cells and LECs (Figure 6, E and F, and Supplemental Figure 10, A and B). Simultaneous knockdown of DTX1 and DTX3L showed a synergy in reversing the flow-mediated decrease of NICD1 level in LECs (Figure 6G and Supplemental Figure 10C). Moreover, the flow-induced increase in sprouting capacity was significantly reduced by knockdown of DTX1 or DTX3L in LECs (Figure 6H), indicating the critical role of DTX1 and DTX3L in the flow-mediated promotion of lymphatic sprouting.

Since DTX3L was uniquely upregulated in LECs after exposure to laminar flow, we generated *Dtx3l* KO mice using Cas9 tech-

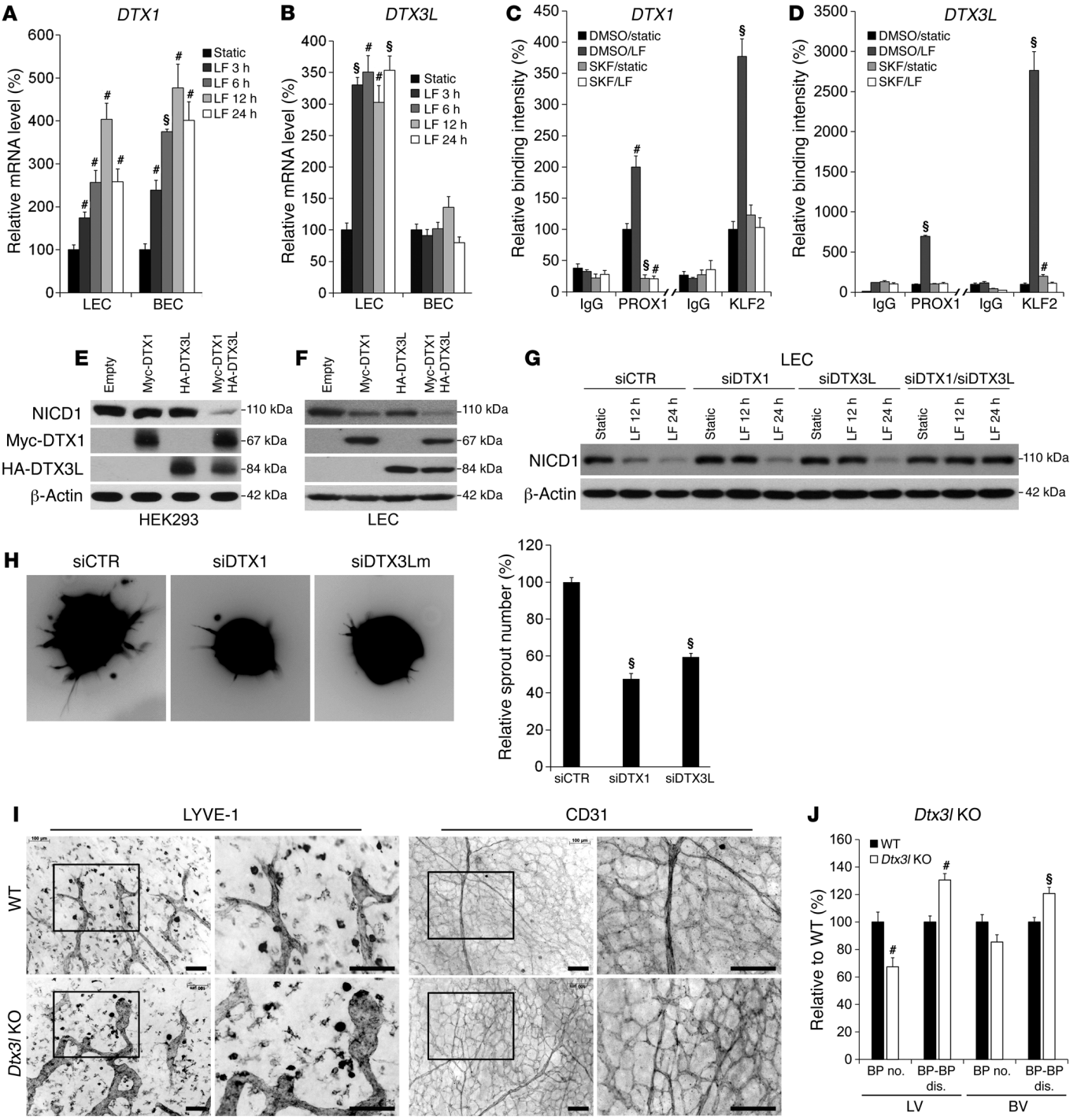

Figure 6. PROX1/KLF2 complex promotes lymphatic sprouting by upregulating DTX1 and DTX3L. (**A** and **B**) qRT-PCR analyses showing the expression of *DTX1* (**A**) and *DTX3L* (**B**) in LECs and BECs exposed to laminar flow (2 dyne/cm^2) for 0 (static), 3, 6, 12, and 24 hours. Protein expression is shown in Supplemental Figure 9. (**C** and **D**) ChIP assays demonstrating the binding of PROX1 and KLF2 to the promoters of the *DTX1* (**C**) and *DTX3L* (**D**) genes in LECs, which were exposed to laminar flow for 0 (static) or 3 hours in the presence of vehicle (DMSO) or SKF-96365 (SKF, 3 μM). (**E** and **F**) Western blot assays showing a synergistic degradation of NICD1 by DTX1 and/or DTX3L in HEK293 cells (**E**) and LECs (**F**). Band intensities are graphed in Supplemental Figure 10, A and B. (**G**) Western blot assays showing the knockdown effect of DTX1 and/or DTX3L on the flow-induced downregulation of NICD1. LECs were transfected with siRNA for DTX1 and/or DTX3L for 24 hours, followed by laminar flow for 0 (static), 12, or 24 hours, and subjected to immunoblotting for NICD1 and β-actin. Band intensities were measured and are graphed in Supplemental Figure 10C. (**H**) Spheroid-based sprouting assay showing that sprouting capability was significantly reduced by knockdown of DTX1 or DTX3L. LECs were transfected with control siRNA (siCTR), siRNA for DTX1 (siDTX1), or siRNA for DTX3L (siDTX3L) for 12 hours, exposed to laminar flow (2 dyn/cm^2) for 24 hours, and subjected to sprouting assays as described in Figure 1E ($n > 20$ spheroids). (**I**) Lymphatics and blood vessels were visualized by LYVE-1 and CD31 staining, respectively, in the back skins of WT and *Dtx3l* KO embryos (E15.5). Boxed areas are enlarged at right. Scale bars: 100 μm. (**J**) The number of branching points (BP no.) and distance between the branching points (BP-BP dis.) of lymphatic vessels (LV) and blood vessels (BV) were quantified and graphed. More than 4 embryos per genotype harvested from at least 3 independent litters were analyzed. Data are expressed as SEM and SD. $^{\#}P < 0.01$; $^{\S}P < 0.001$.

nology (43) and studied the impact of genetic ablation of *Dtx3l* on embryonic lymphatic development. *Dtx3l* KO mice apparently are fertile and grossly normal until 4–6 months of age, after which they tend to become unhealthy and die much earlier than their WT littermates. In developing embryos, DTX3L-deficient lymphatic vessels displayed defective lymphatic sprouting with a reduced number of branching points and an increased distance between the branching points, compared with those in WT embryos (Figure 6, I and J, and Supplemental Figure 11). In addition, whereas WT lymphatic vessels showed characteristic jagged and invasive-appearing tips, DTX3L-deficient lymphatic vessels had atypical dull and round vessel tips. Together, these results suggest that laminar flow upregulates a NOTCH1 E3 ligase, composed of DTX1 and DTX3L, which reduces NICD1 level in LECs and increases lymphatic sprouting.

ORAI1 and DTX3L are required for the suppression of Notch signal in developing lymphatic vessels. We next aimed to corroborate the epistatic relationships among ORAI1, KLF2, DTX3L, and Notch pathway, which were established based on the above in vitro experiments, using ORAI1 and DTX3L mutant embryos. For this purpose, we determined the mRNA levels of *Klf2*, *Dtx3l*, *Nrarp*, *Hey1*, and/or *Hey2* in primary dermal LECs freshly isolated from the WT and mutant embryos. In LECs from *Orai1* KO embryos, *Klf2* and *Dtx3l* were found to be downregulated, while *Nrarp*, *Hey1*, and *Hey2* were upregulated, compared with those in LECs from the WT litter embryos (Figure 7A). Moreover, the Notch pathway genes were upregulated in LECs freshly isolated from *Dtx3l* KO embryos, compared with those in the WT LECs (Figure 7B). Consistent with these mRNA expression patterns, the protein levels of NICD1 were increased in the back skins and intestines of *Orai1* KO (Figure 7C) and *Dtx3l* KO (Figure 7D) embryos. These data imply that ORAI1 and DTX3L are required for the suppression of Notch signal in embryonic LECs, presumably by functional fluid drainage during embryonic development.

DTX3L overexpression rescues lymphatic sprouting defects of Orai1 KO mouse. We next asked whether ectopic expression of DTX3L could rescue the defective lymphatic sprouting caused by genetic deletion of *Orai1*. For this, we generated an inducible *Dtx3l* transgenic mouse line, which harbors a transgene cassette consisting of transcription termination (poly-A) signals flanked by *LoxP* sites (LSL) that are followed by the *Dtx3l*-coding sequences (*LSL-Dtx3l*). These *LSL-Dtx3l* transgenic mice were mated with *Prox1-EGFP* and *Cdh5(PAC)-CreER^{T2}* mice, and resulting pregnant females were injected with tamoxifen at E11.5 and E13.5 for vascular analyses at E15.5 [*LSL-Dtx3l Cdh5(PAC)-CreER^{T2} Prox1-EGFP* mice, hereafter known as *Dtx3l^{TG}* mice]. Indeed, endothelial-specific expression of *Dtx3l* in the transgenic *Dtx3l^{TG}* embryos caused a hypersprouting of the lymphatics, in comparison with the WT embryo (Figure 8, A and B). Interestingly, ectopic expression of *Dtx3l* also appeared to slightly increase blood vessel sprouting. We next intercrossed the *LSL-Dtx3l Cdh5(PAC)-CreER^{T2}* mice (*Dtx3l^{TG}* mice without the *Prox1-EGFP* reporter) and/or *Orai1$^{fl/fl}$* mice. The resulting pregnant females were injected with tamoxifen at E11.5 and 13.5, followed by embryo harvest at E15.5 for vascular analyses. As expected, *Orai1^{ECKO}* embryos [*Orai1$^{fl/fl}$ Cdh5(PAC)-CreER^{T2}*] showed severely defective lymphatic sprouting (Figure 8, C and D). However, this defective lymphatic sprouting could be largely rescued by simultaneous expression of exogenous *Dtx3l* in the *Orai1$^{fl/fl}$ Cdh5(PAC)-CreER^{T2} LSL-Dtx3l* (*Orai1^{ECKO} LSL-Dtx3l*) mice, where the lymphatic sprouting and branching morphogenesis, determined by the number of branching points and the distance between the branching points, appeared to be comparable to those in the control embryos (*Ora1$^{fl/fl}$* and *Orai$^{+/fl}$ LSL-Dtx3l*). Together, these data suggest that ORAI1 is essential for normal lymphatic sprouting by suppressing Notch activity via upregulation of DTX1 and DTX3L. Additionally, the defective lymphatic sprouting caused by *Orai1* deletion could be rescued by ectopic expression of *Dtx3l*.

Discussion

Considering interstitial fluid drainage as the major function of the lymphatics, the basal-to-apical interstitial flow and the subsequent intraluminal flow caused by an overwhelming volume of tissue fluid could serve as an important expansion signal that triggers embryonic and postnatal lymphangiogenesis. This kind of fluid flow–driven lymphangiogenesis may be conceptually similar to hypoxia-activated angiogenesis in purpose to execute their physiological function. Fluid flow resulting from the functional drainage of embryonic fluid imposes shear stress on LECs in the lumen of developing lymphatic vessels. In this study, we investigated how laminar fluid flow activates lymphatic expansion during embryonic lymphatic development. Our in vitro and animal-based findings of this study allow us to build a working model for the molecular mechanism by which steady laminar flow induces lymphatic sprouting (Figure 8E). In our proposed model, steady laminar flow activates calcium influx in LECs through the ORAI1-containing calcium channel and thus increases the concentration of calcium-loaded CaM. Increased Ca^{2+}/CaM, in turn, facilitates a complex formation between PROX1, CaM, and KLF2 proteins, which binds to the promoters of the *DTX1* and *DTX3L* genes and activates their gene expression. Subsequently, upregulated DTX1 and DTX3L proteins form a heterodimeric NOTCH1 E3 ligase that degrades NICD1 protein, leading to activation of lymphatic sprouting. We propose that this mechanism, uniquely operating in lymphatic vessels, presents a key mechanotransduction pathway, through which LECs translate the hemodynamic force to a biological response, specifically, sprouting. In addition, we found in a separate study that steady laminar flow also enhances cell proliferation of LECs by upregulating VEGF-A, VEGF-C, and FGFR3 through the ORAI1/KLF2 pathway (44).

A previous study has nicely demonstrated the presence of embryonic fluid drainage and flow as early as mouse E11.5 and established the interrelationship among embryonic tissue fluid accumulation, fluid pressure increase, elongation and stretching of LECs, VEGFR-3 activation, LEC proliferation, and fluid drainage (6). Despite the convincing presence of lymphatic fluid flow at this developmental stage, however, the precise shear force level in developing embryonic lymphatic networks remains unknown and is thought to be experimentally challenging to measure. On the other hand, shear force levels in other postnatal lymphatics have been previously estimated. Under a basal physiological condition, the shear force level was approximately 0.64 dyn/cm^2 in a collecting lymphatic vessel (45), 0.001 dyn/cm^2 in mouse tail capillaries (46), and 0.003 dyn/cm^2 in human skin capillaries (47). Compared with these very low shear force levels, however, conceptual predic-

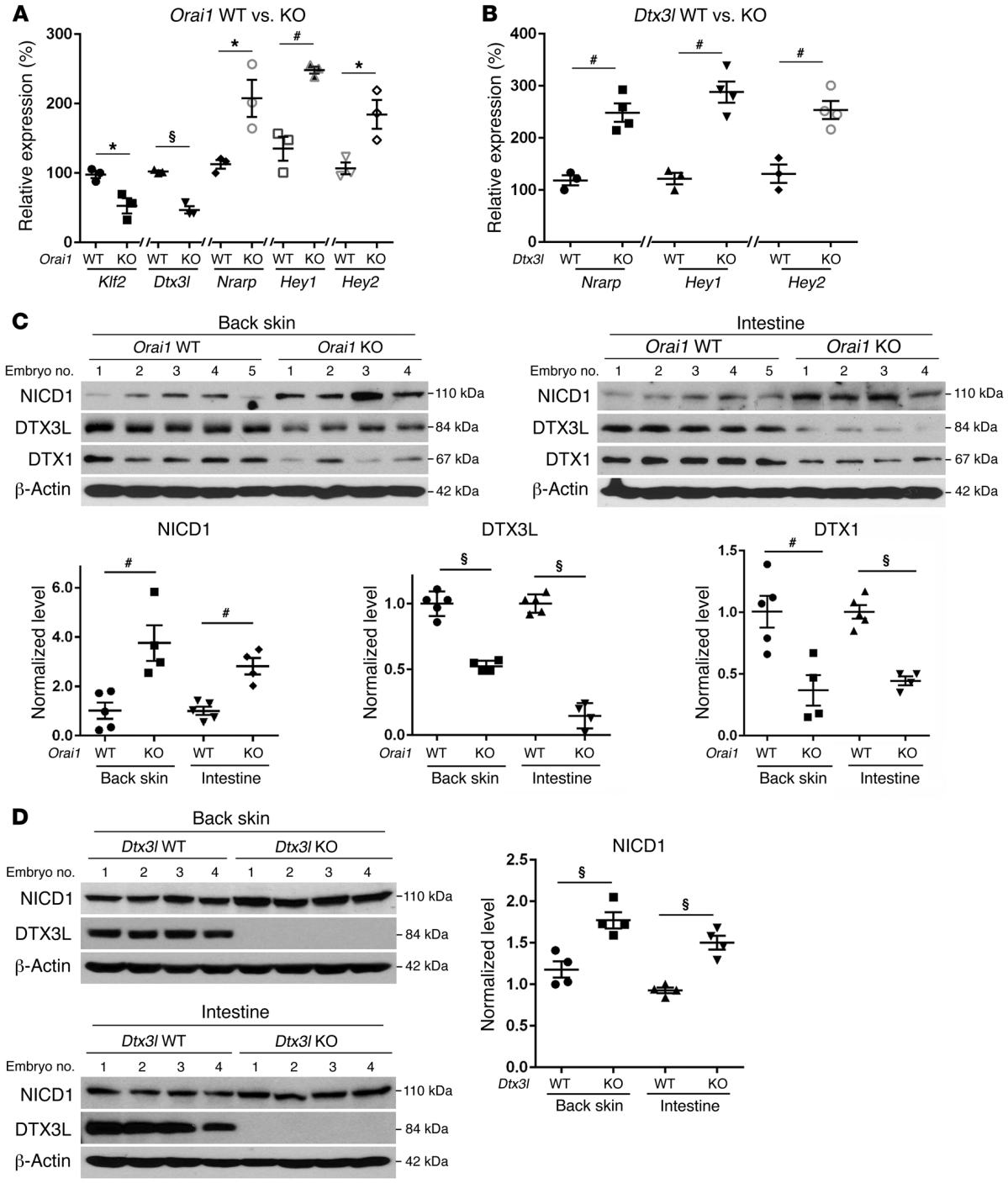

Figure 7. Regulation of Notch pathway genes by ORAI1 and DTX3L during lymphatic development. (**A** and **B**) qRT-PCR analyses showing the expression of *Klf2*, *Dtx3l*, *Nrarp*, *Hey1*, and/or *Hey2* in dermal LECs freshly isolated from WT or KO embryos of *Orai1* (**A**) or *Dtx3l* (**B**). (**C** and **D**) Western blot assays showing the protein expression of NICD1, DTX3L, and/or DTX1 in the back skins or intestines of WT versus mutant embryos of *Orai1* (**C**) or *Dtx3l* (**D**). A monoclonal anti-NOTCH1 antibody that specifically detects the cleaved form of NOTCH1 at Val1744 was used to detect the NICD1 protein. Ratios of band intensities of NICD1, DTX3L, and DTX1 normalized against β-actin are graphed ($n > 4$ per genotype). Data are expressed as mean ± SEM. Each data point represents an individual embryo ($n > 3$ per genotype). $^{*}P < 0.05$; $^{\#}P < 0.01$; $^{\S}P < 0.001$.

tions would suggest that much higher levels of mechanical force may be required as growth stimuli to activate mature and quiescent postnatal lymphatic vessels to form new sprouts. Furthermore, developing lymphatics in rapidly growing embryos will experience much higher levels of hemodynamic force by dealing with an overwhelming amount of embryonic tissue fluid. To identify an optimal shear force condition, we have evaluated various force doses (0.25–5 dyn/cm^2) on cultured human primary dermal LECs and found that a laminar shear force level higher than approximately 1 dyn/cm^2 was needed to clearly trigger the classic endothelial

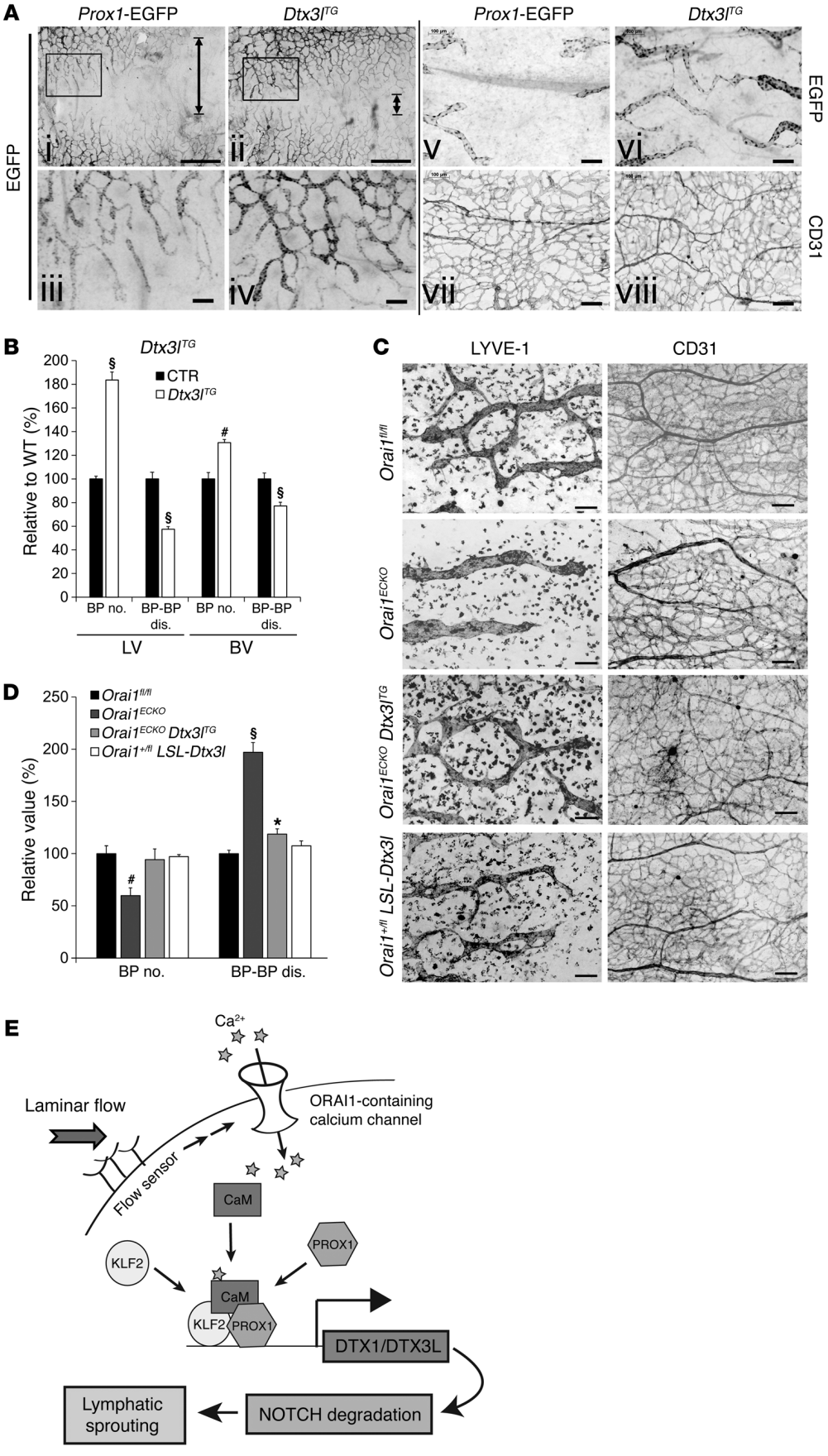

Figure 8. Overexpression of DTX3L rescues the defective lymphatic sprouting of Orai1 KO mice. (**A** and **B**) Lymphatic and blood vessels were visualized in control embryos (*Prox1-EGFP*) or *Dtx3l*^{TG} transgenic embryos [*Prox1-EGFP Cdh5(PAC)-CreER*^{T2} *LSL-Dtx3l*]. (**A**) Pregnant females were injected with tamoxifen at E11.5 and E13.5. At E15.5, dermal lymphatic and blood vessels were visualized by EGFP and CD31 staining, respectively. Panels i and ii display lymphatic vessels growing into the dorsal midline region. Boxed areas are enlarged in panels iii and iv, respectively. Arrows indicate distance between front lines of lymphatic vessels growing from the lateral areas into the midline. Panels v and vi highlight the dorsal midline area. Blood vessels in the corresponding area are shown in panels vii and viii, respectively. (**B**) Vascular analyses were performed and graphed to show branching point numbers (BP no.) and distance between the branching points (BP-BP dis.) of lymphatic vessels (LV) and blood vessels (BV). More than 5 embryos total per genotype obtained from 3 independent litters were analyzed. The dorsal midline regions were imaged for the vascular analyses. (**C** and **D**) Ectopic expression of DTX3L rescues the lymphatic sprouting defects in *Orai1* KO embryos. (**C**) Endothelial-specific *Orai1*^{ECKO} and/or *Dtx3l* ectopic expression were induced in pregnant females at E11.5 and E13.5 by i.p. tamoxifen injection. Lymphatic and blood vessels were detected by LYVE-1 and CD31 staining, respectively, in the back skins of embryos with indicated genotypes at E15.5. (**D**) Vascular analyses were performed to determine the number of branching points (BP no.) and distance between the branching points (BP-BP dis.) of lymphatic vessels. (**E**) Schematic illustration showing a current working model of laminar flow–induced lymphatic sprouting. More than 4 embryos total per genotype were harvested from at least 3 independent litters and analyzed. The dorsal midline areas of the embryos were imaged for the vascular analyses. Scale bars: 100 μm (**A**, iii–viii; **C**); 1 mm (**A**, i, ii). $^{*}P < 0.05$; $^{\#}P < 0.01$; $^{\S}P < 0.001$.

shear stress responses, such as cellular elongation, upregulation of KLF2 and endothelial NOS, and calcium influx (44), suggesting this range of fluid shear stress as a threshold shear force to trigger vascular remodeling phenotypes in vitro. In this study, we thus applied a shear force at approximately 2 dyn/cm^2 to cultured LECs for all our experiments, except for the 3D biomimetic model (Figure 1F and Supplemental Figure 1I), where approximately 5 dyn/cm^2 was applied to activate an efficient blood vessel growth. This minimum force level, similarly termed as a "set point" (48), for cultured LECs is consistent with an elegant study by Baeyens et al. (49), which demonstrated that the set point in LECs for the flow-induced cellular elongation and reorientation is much lower than that in HUVECs (10–20 dyn/cm^2) because of the presence of VEGFR-3 in LECs. Moreover, separate studies have shown that flow-activated calcium influx in LECs reaches its maximum level at approximately 3 dyn/cm^2 (28), whereas the half-maximal activation in HUVECs occurred at a shear stress of 30 dyn/cm^2 (50).

LECs in developing, immature lymphatic vessels during embryogenesis appear to experience steady laminar flow, especially when the interstitial fluid load rapidly increases (6). Given the dynamics of embryonic interstitial fluid, we hypothesize that our working model for the laminar flow–induced lymphatic sprouting may be best applicable to early lymphatic capillaries during development, rather than more matured and large-caliber collecting lymphatics, where PROX1 expression is downregulated and oscillatory flow is the dominant pattern (51). It is important to note that the 2 flow patterns, laminar versus oscillatory, induce somewhat different shear stress transcriptional signatures in LECs. While laminar flow (0.25–5 dyn/cm^2) profoundly induces KLF2 in LECs (Figure 1A), oscillatory flow (~4 dyn/cm^2) augments the valve-forming cell characteristics in LECs without upregulation of KLF2 (8). Moreover, steady laminar flow condition did not change the expression of FOXC2, GATA2, and GJA4 (also known as CX37), which have been shown to be upregulated by oscillatory flow and to play key roles in lymphatic valve formation (8, 52–54). On the other hand, laminar flow was found to promote maturation of collecting lymphatic vessels during development (7), and laminar flow at the blood flow rate downregulates PROX1 and reprograms collecting lymphatics to adopt blood vessel phenotypes (18). Thus, fluid flow at different strengths and patterns may induce different responses in endothelial cells apparently through distinct mechanisms.

Notch signal plays a critical role in controlling vascular expansion and remodeling (19–23). Importantly, a reduction or loss of Notch signaling activates both blood vascular and lymphatic sprouting during development. Deltex (DTX) proteins were originally isolated as a regulator of Notch signaling in *Drosophila*. Deltex and its mammalian homolog DTX1 can either promote or inhibit Notch signaling depending on the cellular context. While deltex and DTX1 can promote Notch-dependent transcriptional activity, they also function as an E3 ligase that targets Notch protein for ubiquitination and degradation (40, 41, 55, 56). Notably, DTX3L interacts with DTX1 to form a more active heterodimeric E3 ligase (39, 42). Our study shows that DTX3L knockdown phenocopied ORAI1 knockdown in cultured LECs, abrogating flow-induced Notch downregulation (Figure 2C and Figure 6G). These in vitro data were further confirmed in animal models: Both *Dtx3l* knockout and *Orai1* knockout increased NICD1 levels and upregulated the Notch target genes (Figure 7). An equally important finding is that both mRNA and protein levels of DTX3L were upregulated by laminar flow selectively in LECs but not in BECs (Figure 6B and Supplemental Figure 9). This implies that DTX3L is a critical player in the laminar flow–induced Notch downregulation in LECs. Supporting this notion, ectopic expression of DTX3L is sufficient to promote sprouting of both blood and lymphatic vessels (Figure 8, A and B). Together, a cooperative upregulation of DTX3L by PROX1, CaM, and KLF2 accounts for Notch downregulation in LECs and increased lymphatic sprouting in response to low-rate steady laminar flow.

Although both LECs and BECs display the classic responses to shear stress, only LECs downregulated Notch activity and enhanced sprouting, when exposed to low-rate steady laminar flow. In comparison, the same experimental condition did not trigger comparable phenotypes in BECs. It is necessary to exert caution in interpreting these data in BECs, because our shear force level was much lower than the physiological levels that BECs may experience in vivo. Nonetheless, Notch signal suppression through NICD1 downregulation may be a unique event that requires a lymphatic-specific mechanism. Indeed, NICD1 downregulation was found to be orchestrated by the lymphatic-specific protein PROX1 that interplays with the master regulator of the shear stress response, KLF2, and the Ca^{2+} signal mediator, CaM. Despite the clear presence of KLF2 upregulation and increased Ca^{2+} entry, laminar flow did not alter Notch activity in BECs, presumably because of the absence of PROX1. Therefore, we propose that the shear stress phenotype of BECs may be the "default" endothelial response, produced by KLF2 and CaM in the absence of the lymphatic-specific factor PROX1. In comparison, because BECs differentiate into LECs through the expression of PROX1, the unique shear stress phenotypes of LECs may be a "newly acquired" response choreographed by the lymphatic-specific PROX1 in collaboration with the 2 "old" players, KLF2 and CaM. Therefore, it would be very interesting to define how PROX1 can modify the collaborative function of KLF2 and CaM by comparing their functional interplays in LECs versus BECs. Moreover, it will be intriguing to define the molecular basis for the increased blood vessel network formation in *Orai1* KO embryos.

In summary, fluid flow has long been thought to be a key nonbiological growth stimulus for lymphatic expansion. This is in agreement with the major function of the lymphatics, that is, draining interstitial fluid. Here, our working model illustrates a molecular mechanism underlying the lymphatic-specific activation of sprouting by laminar flow, underscoring the differential responses of the 2 vascular systems. Our study not only offers a better understanding of flow-induced lymphatic expansion, but also provides significant insight into other mechanotransduction pathways in endothelial cells.

Methods

Cell culture–related reagents and assays. Human primary endothelial cells (LECs and BECs) were cultured in media based on Endothelial Basal Media (EBM, Lonza) as previously described (57, 58). Primary cells under seventh population doublings (passage) were used for this study. HEK293 cells were obtained from American Type Culture Collection and cultured in DMEM (Genesee Scientific) supplemented

with 10% calf serum and antibiotics (Invitrogen). Continuous laminar flow was generated based on the orbital rotation of culture medium over a monolayer of endothelial cells in a standard CO_2 incubator as previously reported (15). Steady laminar flow was applied at 2 dyn/cm^2 for all experiments in this study, except for Figure 1F and Supplemental Figure 1I (5 dyn/cm^2), as previously described (15). Spheroid-based sprouting assay was performed as described (25). Briefly, cells were exposed to laminar flow for 24 hours and then treated with a CellTracker (Molecular Probes; C7025, 1.5 μM) dye for 0.5 hours. If necessary, cells were transfected with siRNA for 24 hours before the onset of laminar flow. The cells were mixed with Methocel (20%; Dow Chemical Co.), aggregated in hanging drops for 24 hours, and then embedded in Matrigel for 24 hours before imaging. Sources of antibodies for Western blot analyses and immunostaining are listed in Supplemental Table 1. See complete unedited blots in the supplemental material. The sources of reagents used in this study are: SKF-96365 hydrochloride, Tocris Bioscience; Tamoxifen Free Base, MP Biomedicals; and Bapta-AM, Sigma-Aldrich.

Animal-related studies. All mice were maintained and used for experiments in mixed backgrounds, except for *Orai1* conventional KO mice, which were maintained in the C57BL/6 background. Sources of mice are: *PROX1-EGFP*, Jackson Laboratory [Tg(Prox1-EGFP)KY221Gsat] (32); *LSL-GCaMP3*, Jackson Laboratory [B6;129S-Gt(ROSA)26Sortm38(CAG-GCaMP3)Hze/J]; *Tie2-Cre*, Jackson Laboratory; *Cdh5(PAC)-CreER^{T2}*, Ralf Adams, University of Münster (33); floxed *Klf2* (*Klf2$^{fl/fl}$*), Jerry Lingrel, University of Cincinnati (Cincinnati, Ohio, USA) (38); *Prox1-CreER^{T2}*, Taija Mäkinen, Uppsala University (Uppsala, Sweden) (52); and *Orai1* KO (31, 59) and floxed *Orai1* (*Orai1$^{fl/fl}$*), Yousang Gwack, UCLA. *Dtx3l* transgenic and KO mice were newly developed for this study in the University of Southern California Norris Comprehensive Cancer Center Transgenic/Knockout Rodent Core as described below. *Orai1$^{fl/fl}$* mice were generated in Yousang Gwack's laboratory by flanking of exon 2 of mouse *Orai1* with LoxP sites by homologous recombination in AB2.2 (129SvEv) embryonic stem cells. Exon 2 encodes more than 50% of the protein, and its deletion results in loss of expression of *Orai1*. G418-resistant clones were screened by PCR for homologous recombination at both homology arms. Chimeric mice with floxed *Orai1* alleles were generated by blastocyst injection of heterozygous *Orai1$^{fl/+}$* embryonic stem cell clones. Founder *Orai1$^{fl/+}$* chimeric mice were bred with Flp-deleter mice (Jackson Laboratory) to remove the neomycin resistance gene cassette. Deletion of ORAI1 protein was validated by immunoblotting and measurement of SOCE. The *Dtx3l* conditional transgenic mouse line was generated by microinjection of the gel-purified SaII/PacI fragment from the *Dtx3l* transgenic vector (YH3004; see below for detailed information). *Dtx3l* KO mice were generated by pronuclear injection of recombinant Cas9 protein and 2 guide RNAs (AACUACUAAAAAGCCAGUAGAGG and UUGUGAUGACAUACAUCCCCAGG) for *Dtx3l* (PNA Bio) in the University of Southern California Norris Comprehensive Cancer Center Transgenic/Knockout Rodent Core.

Cellular, molecular, and biochemical assays. Detailed information on isolation of mouse embryonic dermal LECs, gene and protein expression, plasmids and vectors, mutagenesis, Notch activity reporter assay, confocal laser-scanning fluorescence microscopy for calcium imaging, CaM overlay assay, NMR study, co-IP, and 3D microfluidic sprouting assay is available in Supplemental Methods. Sequences of all the primers and siRNAs are listed in Supplemental Table 2.

Statistics. Student's *t* test (2-tailed) was used to determine whether the differences between the experimental and control groups were statistically significant. A *P* value less than 0.05 was considered to be statistically significant. The analyses were performed using Microsoft Excel (Microsoft Office) and GraphPad Prism 6 (GraphPad Software Inc.).

Study approval. Human primary BECs and LECs were isolated and cultured from deidentified human neonatal foreskins with approval by the Institutional Review Board of the University of Southern California (principal investigator, YK Hong). Animal-related studies were approved by the University of Southern California Institutional Animal Care and Use Committee (principal investigator, YK Hong).

Author contributions

DC, EP, EJ, YJS, JY, EL, MH, SL, HI, and JB performed experiments and collected data. JPP, SS, YG, CSC, HV, AKW, and YKH designed and supervised the research. RHA and CJK provided the resources.

Acknowledgments

We thank Jerry Lingrel and Taija Mäkinen for sharing floxed *Klf2* and *Prox1-CreER^{T2}* mice, respectively. This study was supported by NIH grants (EY026260 to YKH, HL121036 to YKH, HL119583 to YKH, EB00262 to CSC, and EB017103 to CSC), an American Heart Association Grant-in-Aid (13GRNT17060131 to YKH), and the L.K. Whittier Foundation (to YKH and AKW).

Address correspondence to: Young-Kwon Hong, Department of Surgery, University of Southern California, Norris Comprehensive Cancer Center, 1450 Biggy Street NRT6501, Los Angeles, California 90033, USA. E-mail: young.hong@usc.edu.

1. Escobedo N, Oliver G. Lymphangiogenesis: origin, specification, and cell fate determination. *Annu Rev Cell Dev Biol*. 2016;32:677–691.
2. Swartz MA, Boardman KC. The role of interstitial stress in lymphatic function and lymphangiogenesis. *Ann N Y Acad Sci*. 2002;979:197–210.
3. Ng CP, Helm CL, Swartz MA. Interstitial flow differentially stimulates blood and lymphatic endothelial cell morphogenesis in vitro. *Microvasc Res*. 2004;68(3):258–264.
4. Boardman KC, Swartz MA. Interstitial flow as a guide for lymphangiogenesis. *Circ Res*. 2003;92(7):801–808.
5. Breslin JW, Kurtz KM. Lymphatic endothelial cells adapt their barrier function in response to changes in shear stress. *Lymphat Res Biol*. 2009;7(4):229–237.
6. Planas-Paz L, Strilić B, Goedecke A, Breier G, Fässler R, Lammert E. Mechanoinduction of lymph vessel expansion. *EMBO J*. 2012;31(4):788–804.
7. Sweet DT, et al. Lymph flow regulates collecting lymphatic vessel maturation in vivo. *J Clin Invest*. 2015;125(8):2995–3007.
8. Sabine A, et al. Mechanotransduction, PROX1, and FOXC2 cooperate to control connexin37 and calcineurin during lymphatic-valve formation. *Dev Cell*. 2012;22(2):430–445.
9. Kim S, Chung M, Jeon NL. Three-dimensional biomimetic model to reconstitute sprouting lymphangiogenesis in vitro. *Biomaterials*. 2016;78:115–128.
10. Schwartz MA, Simons M. Lymphatics thrive on stress: mechanical force in lymphatic development. *EMBO J*. 2012;31(4):781–782.
11. Masumura T, Yamamoto K, Shimizu N, Obi S, Ando J. Shear stress increases expression of the arterial endothelial marker ephrinB2 in murine ES cells via the VEGF-Notch signaling pathways. *Arterioscler Thromb Vasc Biol*. 2009;29(12):2125–2131.
12. Levesque MJ, Nerem RM, Sprague EA. Vascular endothelial cell proliferation in culture and the

influence of flow. *Biomaterials*. 1990;11(9):702–707.
13. Akimoto S, Mitsumata M, Sasaguri T, Yoshida Y. Laminar shear stress inhibits vascular endothelial cell proliferation by inducing cyclin-dependent kinase inhibitor p21(Sdi1/Cip1/Waf1). *Circ Res*. 2000;86(2):185–190.
14. Lin K, et al. Molecular mechanism of endothelial growth arrest by laminar shear stress. *Proc Natl Acad Sci U S A*. 2000;97(17):9385–9389.
15. dela Paz NG, Walshe TE, Leach LL, Saint-Geniez M, D'Amore PA. Role of shear-stress-induced VEGF expression in endothelial cell survival. *J Cell Sci*. 2012;125(pt 4):831–843.
16. Ando J, Yamamoto K. Vascular mechanobiology: endothelial cell responses to fluid shear stress. *Circ J*. 2009;73(11):1983–1992.
17. Jahnsen ED, Trindade A, Zaun HC, Lehoux S, Duarte A, Jones EA. Notch1 is pan-endothelial at the onset of flow and regulated by flow. *PLoS One*. 2015;10(4):e0122622.
18. Chen CY, et al. Blood flow reprograms lymphatic vessels to blood vessels. *J Clin Invest*. 2012;122(6):2006–2017.
19. Zheng W, et al. Notch restricts lymphatic vessel sprouting induced by vascular endothelial growth factor. *Blood*. 2011;118(4):1154–1162.
20. Fatima A, et al. Murine Notch1 is required for lymphatic vascular morphogenesis during development. *Dev Dyn*. 2014;243(7):957–964.
21. Niessen K, et al. The Notch1-Dll4 signaling pathway regulates mouse postnatal lymphatic development. *Blood*. 2011;118(7):1989–1997.
22. Domigan CK, Iruela-Arispe ML. Recent advances in vascular development. *Curr Opin Hematol*. 2012;19(3):176–183.
23. Roca C, Adams RH. Regulation of vascular morphogenesis by Notch signaling. *Genes Dev*. 2007;21(20):2511–2524.
24. Korff T, Krauss T, Augustin HG. Three-dimensional spheroidal culture of cytotrophoblast cells mimics the phenotype and differentiation of cytotrophoblasts from normal and preeclamptic pregnancies. *Exp Cell Res*. 2004;297(2):415–423.
25. Alajati A, et al. Spheroid-based engineering of a human vasculature in mice. *Nat Methods*. 2008;5(5):439–445.
26. Wong KH, Chan JM, Kamm RD, Tien J. Microfluidic models of vascular functions. *Annu Rev Biomed Eng*. 2012;14:205–230.
27. Galie PA, Nguyen DH, Choi CK, Cohen DM, Janmey PA, Chen CS. Fluid shear stress threshold regulates angiogenic sprouting. *Proc Natl Acad Sci U S A*. 2014;111(22):7968–7973.
28. Jafarnejad M, Cromer WE, Kaunas RR, Zhang SL, Zawieja DC, Moore JE. Measurement of shear stress-mediated intracellular calcium dynamics in human dermal lymphatic endothelial cells. *Am J Physiol Heart Circ Physiol*. 2015;308(7):H697–H706.
29. Singh A, Hildebrand ME, Garcia E, Snutch TP. The transient receptor potential channel antagonist SKF96365 is a potent blocker of low-voltage-activated T-type calcium channels. *Br J Pharmacol*. 2010;160(6):1464–1475.
30. Srikanth S, Gwack Y. Molecular regulation of the pore component of CRAC channels, Orai1. *Curr Top Membr*. 2013;71:181–207.
31. Gwack Y, et al. Hair loss and defective T- and B-cell function in mice lacking ORAI1. *Mol Cell Biol*. 2008;28(17):5209–5222.
32. Choi I, et al. Visualization of lymphatic vessels by Prox1-promoter directed GFP reporter in a bacterial artificial chromosome-based transgenic mouse. *Blood*. 2011;117(1):362–365.
33. Wang Y, et al. Ephrin-B2 controls VEGF-induced angiogenesis and lymphangiogenesis. *Nature*. 2010;465(7297):483–486.
34. Wigle JT, Oliver G. Prox1 function is required for the development of the murine lymphatic system. *Cell*. 1999;98(6):769–778.
35. Yoo JH, et al. Regulation of the dual specificity protein phosphatase, DsPTP1, through interactions with calmodulin. *J Biol Chem*. 2004;279(2):848–858.
36. Zariwala HA, et al. A Cre-dependent GCaMP3 reporter mouse for neuronal imaging in vivo. *J Neurosci*. 2012;32(9):3131–3141.
37. Lee JS, et al. Klf2 is an essential regulator of vascular hemodynamic forces in vivo. *Dev Cell*. 2006;11(6):845–857.
38. Wani MA, Means RT, Lingrel JB. Loss of LKLF function results in embryonic lethality in mice. *Transgenic Res*. 1998;7(4):229–238.
39. Yan Q, et al. BBAP monoubiquitylates histone H4 at lysine 91 and selectively modulates the DNA damage response. *Mol Cell*. 2009;36(1):110–120.
40. Zhang P, Yang Y, Nolo R, Zweidler-McKay PA, Hughes DP. Regulation of NOTCH signaling by reciprocal inhibition of HES1 and Deltex 1 and its role in osteosarcoma invasiveness. *Oncogene*. 2010;29(20):2916–2926.
41. Mukherjee A, Veraksa A, Bauer A, Rosse C, Camonis J, Artavanis-Tsakonas S. Regulation of Notch signalling by non-visual beta-arrestin. *Nat Cell Biol*. 2005;7(12):1191–1201.
42. Takeyama K, et al. The BAL-binding protein BBAP and related Deltex family members exhibit ubiquitin-protein isopeptide ligase activity. *J Biol Chem*. 2003;278(24):21930–21937.
43. Shui B, Hernandez Matias L, Guo Y, Peng Y. The rise of CRISPR/Cas for genome editing in stem cells. *Stem Cells Int*. 2016;2016:8140168.
44. Choi D, et al. ORAI1 activates proliferation of lymphatic endothelial cells in response to laminar flow through Krüppel-like factors 2 and 4 [published online ahead of print February 6, 2017]. *Circ Res*. https://doi.org/10.1161/CIRCRESAHA.116.309548.
45. Dixon JB, Greiner ST, Gashev AA, Cote GL, Moore JE, Zawieja DC. Lymph flow, shear stress, and lymphocyte velocity in rat mesenteric prenodal lymphatics. *Microcirculation*. 2006;13(7):597–610.
46. Berk DA, Swartz MA, Leu AJ, Jain RK. Transport in lymphatic capillaries. *Am J Physiol*. 1996;270(1 pt 2):H330–H337.
47. Fischer M, et al. Flow velocity of single lymphatic capillaries in human skin. *Am J Physiol*. 1996;270(1 pt 2):H358–H363.
48. Rodbard S. Vascular caliber. *Cardiology*. 1975;60(1):4–49.
49. Baeyens N, et al. Vascular remodeling is governed by a VEGFR3-dependent fluid shear stress set point. *Elife*. 2015;4:04645.
50. Schwarz G, Callewaert G, Droogmans G, Nilius B. Shear stress-induced calcium transients in endothelial cells from human umbilical cord veins. *J Physiol (Lond)*. 1992;458(1):527–538.
51. Norrmén C, et al. FOXC2 controls formation and maturation of lymphatic collecting vessels through cooperation with NFATc1. *J Cell Biol*. 2009;185(3):439–457.
52. Bazigou E, et al. Genes regulating lymphangiogenesis control venous valve formation and maintenance in mice. *J Clin Invest*. 2011;121(8):2984–2992.
53. Kazenwadel J, et al. GATA2 is required for lymphatic vessel valve development and maintenance. *J Clin Invest*. 2015;125(8):2979–2994.
54. Kanady JD, Dellinger MT, Munger SJ, Witte MH, Simon AM. Connexin37 and Connexin43 deficiencies in mice disrupt lymphatic valve development and result in lymphatic disorders including lymphedema and chylothorax. *Dev Biol*. 2011;354(2):253–266.
55. Yamamoto N, et al. Role of Deltex-1 as a transcriptional regulator downstream of the Notch receptor. *J Biol Chem*. 2001;276(48):45031–45040.
56. Matsuno K, et al. Involvement of a proline-rich motif and RING-H2 finger of Deltex in the regulation of Notch signaling. *Development*. 2002;129(4):1049–1059.
57. Shin JW, et al. Prox1 promotes lineage-specific expression of fibroblast growth factor (FGF) receptor-3 in lymphatic endothelium: a role for FGF signaling in lymphangiogenesis. *Mol Biol Cell*. 2006;17(2):576–584.
58. Lee S, et al. Prox1 physically and functionally interacts with COUP-TFII to specify lymphatic endothelial cell fate. *Blood*. 2009;113(8):1856–1859.
59. Kim KD, Srikanth S, Yee MK, Mock DC, Lawson GW, Gwack Y. ORAI1 deficiency impairs activated T cell death and enhances T cell survival. *J Immunol*. 2011;187(7):3620–3630.
60. Minoguchi S, et al. RBP-L, a transcription factor related to RBP-Jκ. *Mol Cell Biol*. 1997;17(5):2679–2687.

SUPPLEMENTAL INFORMATION

SUPPLEMENTAL METHODS

Isolation of Mouse Embryonic Dermal LECs

Embryo back skins with proper genotypes were harvested, chopped into small pieces, and then treated with dispase and collagenase (1mg/mL, Hoffmann-La Roche, Ltd), collagenase II (50 U/mL, Worthington Biochemical, Lakewood, NJ) and DNase I (1,000 U/mL, New England Biolabs, Ipswich, MA) in phosphate buffered saline (PBS) at 37 °C for 1 hr. Dermal cell mixtures were isolated by triturating enzymatically treated back skins through a needle (18.5G) and filtering through a cell strainer. Cells were then centrifuged, resuspended in EBM-based media, seeded on a culture dish, and incubated 37 °C for 4 hr. The cultures were washed with PBS twice, trypsinized, and then incubated with LYVE1 antibody (Angiobio, 11-034) at 4 °C for 1 hr. Concurrently, biotinylated goat anti-rabbit IgG antibody (Vector Laboratories, BA-1000) and Dynabeads Biotin Binder (Invitrogen, 11047) were separately incubated at 4 °C for 1 hr. and then finally mixed with the cells incubated with the LYVE1 antibody at 4 °C for 1 hr., followed by RNA isolation processes using Trizol solution (Thermo Fisher Scientific).

Gene and Protein Expression, Plasmids and Vectors, Mutagenesis

Standard protocols were employed for quantitative real-time RT-PCR and western blotting. Plasmids and siRNAs were transfected into target cells using HMEC-L Nucleofector Kit (Lonza, VPB1003) or PBS (1), respectively. Immunofluorescent staining for whole-mount/tissue sections was performed as previously described (2). Sources of expression vectors are as follows: Myc-tag PROX1 (Dr. Paul A. Overbeek, Baylor College of Medicine, Houston, TX) (3), FLAG-tag KLF2 (Dr. Hiroaki Taniguchi, University of Tokyo, Tokyo, Japan) (4), Myc-tag DTX1 and HA-tag DTX3L (Dr. Margaret A. Shipp, Harvard Medical School, Boston, MA) (5), and pGa981-6/TP1-luc (Dr. Hua Han, Fourth Military Medical University, Xi'an, China) (6). The following are the vectors that were generated for this study: For pcDNA3-HA-CaM (YH2307), human CaM fragment was constructed by PCR using a EcoRV site-containing forward primer and a XhoI site-harboring reverse primer, and cloned into EcoRV/XhoI sites of pcDNA3 (Life Technologies). The primer sequences are listed in Supplemental Table2. We constructed recombinant GST-PROX1 fusion

vectors as follows. Human PROX1 fragment (1-546 a.a.) was PCR-amplified from a human cDNA library using a primer set (Supplemental Table2) and cloned in EcoRI/SalI sites of pGEX-5X-1. The resulting vector (YH2012) was digested with EcoRI/SmaI and the insert was transferred to EcoRI/SmaI sites of pGEX-5X-1 to generate PROX1-D1 (YH2722). For PROX1-D2 to PROX1-D7, PROX1 fragments were PCR-amplified against human PROX1 cDNA with forward and reverse primers harboring a EcoRI site and a SalI site, respectively, and cloned into EcoRI/SalI sites of pGEX-5X-1 (GE Healthcare Life Sciences). Their sequences are listed in Supplemental Table2. These GST-PROX1 fusion vectors were transformed into BL21 bacterial strain and recombinant GST-PROX1 fusion fragments were produced and purified as described previously (7). For Dtx3L-transgenic vector (YH3004), mouse Dtx3L was PCR-amplified from pCR4-TOPO-mDtx3L (Source Bioscience, Santa Fe Springs, CA) and cloned into NotI/EcoRI site of pcDNA3. The resulting construct was then PCR-amplified, digested with BamHI and PacI and cloned into BglII/PacI sites of a *LoxP*-Stop-*LoxP*-containing conditional expression vector, pCAG-sGFP-4X L2 Pac (kindly provided by Dr. Jeong K. Yoon, Maine Medical Center Research Institute, Scarborough, ME) (8). Substitution mutagenesis to aspartic acid (D) in human PROX1 protein was performed using corresponding mutagenesis primers as previously described (9). Sequences of all the primers are listed in Supplemental Table2.

Notch Activity Reporter Assay

Human primary LECs were transfected with a RBP-JK reporter luciferase vector, pGa981-6/TP1-luc (6), or the parental vector (pGL3-Basic, Promega Corporation, Madison, WI) for 24 hr. The cells were then subjected to steady laminar flow at 2 dyne/cm^2 for 24 or 48 hr., followed by a standard luciferase assay using Bright-Glo™ Luciferase Assay System (Promega). Total cell lysate was quantified by the Bradford assay (Sigma-Aldrich) and equal amount of the lysates was used for the luciferase assay.

Confocal Laser-Scanning Fluorescence Microscopy for Calcium Imaging

Primary LECs were seeded and preloaded with Fluo-4 on μ-Slides and unidirectional laminar flow (2 dyne/cm^2) was applied using a pump that was connected to the slide. Calcium releasing signals were

captured with a Leica TCS SP5 AOTF MP confocal microscope system (Leica Microsystems, Heidelberg, Germany). A Leica DMI6000 inverted microscope with 20X 0.7NA objective (Leica Microsystems) was powered by an Argon 488-nm for these studies. Images were collected in time series (*xyt*, 1 s per frame) with the Leica LAS AF imaging software, and excitation at 488 nm, emission at 520 ± 50 nm was used. All experiments were performed with the same instrument settings (laser power, offset, gain of both detector channels). Fluorescence intensity (8 bit) was measured with the Leica LAS lite imaging software's Quantification Tools.

CaM Overlay Assay

CaM overlay assays were performed to determine *in vitro* protein-protein interaction between PROX1 protein fragments and HRP-conjugated CaM protein on western membranes. Western blotting assay was first performed to detect the quantity and quality of GST-PROX1 fusion fragments that were produced in bacteria (top panel, Fig.4A). CaM overlay assays were then performed as previously described (7). Briefly, duplicate GST-PROX1 fragment blots were probed with GmCaM1::HRP and GmCaM4::HRP conjugates in the presence of $CaCl_2$ (1 mM) or EGTA (5 mM) (middle and bottom panels, respectively, Fig.4A). The bound HRP-conjugated CaM protein was visualized using ECL detection system (GE Healthcare Life Sciences).

NMR Study

The NMR sample contained 0.5 mM ^{15}N-labeled CaM, 100 mM KCl, 20 mM Bis-Tris (pH 6.8), 5 mM $CaCl_2$, 0.5 mM 2,2-dimethyl-2-silapentane-5-sulfonate (DSS) in 10%D_2O/90%H_2O. A stock solution of 5 mM PROX1 peptide in the same buffer was titrated into the NMR sample. The titration was monitored through HSQC experiments acquired on a Bruker Avance 700 MHz NMR spectrometer at 30 °C. DSS was used as a reference to obtain the ^{1}H and ^{15}N chemical shifts. The spectra were processed with NMRPipe (10) and analyzed using NMRView (11). The chemical shift assignment for Ca^{2+}-CaM was obtained from Gifford *et al* (11).

Co-Immunoprecipitation

The standard co-immunoprecipitation protocol was used to show a direct protein-protein interaction as previously described (12). For the serial co-IP, plasmid vectors expressing Myc-PROX1 and HA-CaM were co-transfected in HEK293 cells with or without a FLAG-KLF2-expressing vector for 48 hr. Cell were lysed in PBS containing NP-40 (0.5%) to harvest whole cell lysates (WCL), which were then incubated with FLAG-antibody beads to precipitate KLF2 by centrifugation at 4 °C. The KLF2-containing precipitants were eluted into the same lysis buffer (PBS with NP-40, 0.5%) from the FLAG-beads using FLAG peptide (0.5 mg/mL, LifeTein, LLC). Elutes from the KLF2-expressing cell lysates (+KLF2) were again precipitated using normal IgG or anti-HA antibody, followed by incubation with Protein-A/G beads (Pierce) to precipitate HA-CaM. The resulting isolates from both rounds of co-IPs were blotted with anti-FLAG, anti-HA, and anti-Myc antibodies.

3-D Microfluidic Sprouting Assay

A microfluidic device was used to assemble vessel-like structures that are lined with BECs or LECs as described previously (13). Briefly, collagen 1 (2.5 mg/mL) was polymerized in the device around two 400-μm-diameter needles. After removing the needles, BECs or LECs were seeded (4 million/mL) into one channel, and we allowed them to form a confluent monolayer overnight. Devices were placed on a platform rocker to generate gravity-driven flow (5 dyne/cm^2) or placed on a static incubator. Growth factors were added to the opposite channel to induce sprouting as described previously (13).

Supplemental References

1. Kang, J., Ramu, S., Lee, S., Aguilar, B., Ganesan, S.K., Yoo, J., Kalra, V.K., Koh, C.J., and Hong, Y.K. 2009. Phosphate-buffered saline-based nucleofection of primary endothelial cells. *Anal Biochem* 386:251-255.

2. Choi, I., Chung, H.K., Ramu, S., Lee, H.N., Kim, K.E., Lee, S., Yoo, J., Choi, D., Lee, Y.S., Aguilar, B., et al. 2011. Visualization of lymphatic vessels by Prox1-promoter directed GFP reporter in a bacterial artificial chromosome-based transgenic mouse. *Blood* 117:362-365.

3. Chen, Q., Dowhan, D.H., Liang, D., Moore, D.D., and Overbeek, P.A. 2002. CREB-binding protein/p300 co-activation of crystallin gene expression. *J Biol Chem* 277:24081-24089.

4. Taniguchi, H., Jacinto, F.V., Villanueva, A., Fernandez, A.F., Yamamoto, H., Carmona, F.J., Puertas, S., Marquez, V.E., Shinomura, Y., Imai, K., et al. 2012. Silencing of Kruppel-like factor 2 by the histone methyltransferase EZH2 in human cancer. *Oncogene* 31:1988-1994.

5. Takeyama, K., Aguiar, R.C., Gu, L., He, C., Freeman, G.J., Kutok, J.L., Aster, J.C., and Shipp, M.A. 2003. The BAL-binding protein BBAP and related Deltex family members exhibit ubiquitin-protein isopeptide ligase activity. *J Biol Chem* 278:21930-21937.

6. Minoguchi, S., Taniguchi, Y., Kato, H., Okazaki, T., Strobl, L.J., Zimber-Strobl, U., Bornkamm, G.W., and Honjo, T. 1997. RBP-L, a transcription factor related to RBP-Jkappa. *Mol Cell Biol* 17:2679-2687.

7. Yoo, J.H., Cheong, M.S., Park, C.Y., Moon, B.C., Kim, M.C., Kang, Y.H., Park, H.C., Choi, M.S., Lee, J.H., Jung, W.Y., et al. 2004. Regulation of the dual specificity protein phosphatase, DsPTP1, through interactions with calmodulin. *J Biol Chem* 279:848-858.

8. Venkatesh, D.A., Park, K.S., Harrington, A., Miceli-Libby, L., Yoon, J.K., and Liaw, L. 2008. Cardiovascular and hematopoietic defects associated with Notch1 activation in embryonic Tie2-expressing populations. *Circ Res* 103:423-431.

9. Kunkel, T.A. 1985. Rapid and efficient site-specific mutagenesis without phenotypic selection. *Proc Natl Acad Sci U S A* 82:488-492.

10. Delaglio, F., Grzesiek, S., Vuister, G.W., Zhu, G., Pfeifer, J., and Bax, A. 1995. NMRPipe: a multidimensional spectral processing system based on UNIX pipes. *J Biomol NMR* 6:277-293.

11. Johnson, B.A. 2004. Using NMRView to visualize and analyze the NMR spectra of macromolecules. *Methods Mol Biol* 278:313-352.

12. Choi, I., Lee, S., Kyoung Chung, H., Suk Lee, Y., Eui Kim, K., Choi, D., Park, E.K., Yang, D., Ecoiffier, T., Monahan, J., et al. 2012. 9-cis retinoic Acid promotes lymphangiogenesis and enhances lymphatic vessel regeneration: therapeutic implications of 9-cis retinoic Acid for secondary lymphedema. *Circulation* 125:872-882.

13. Nguyen, D.H., Stapleton, S.C., Yang, M.T., Cha, S.S., Choi, C.K., Galie, P.A., and Chen, C.S. 2013. Biomimetic model to reconstitute angiogenic sprouting morphogenesis in vitro. *Proc Natl Acad Sci U S A* 110:6712-6717.

SUPPLEMENTAL FIGURE LEGENDS

Supplemental Figure 1. Laminar flow selectively suppresses NOTCH1 activity in LECs

(**A**) Cell morphology of LECs and BECs in response to low-rate steady laminar flow (LF) at 2 dyne/cm^2 for 0 (static), 12, 24, and 48 hr. Scale bars: 50 μm.

(**B-D**) Real-time RT-PCR (qRT-PCR) data showing the mRNA levels of eNOS in LECs and BECs (**B**), Notch target genes in BECs (**C**), and NOTCH1 in LECs (**D**) in response to steady laminar flow at 2 dyne/cm^2 for the indicated time.

(**E**) Western blot bands of NICD-1 in Fig.1C in the main text were quantitated and charted.

(**F,G**) Protein levels (**F**) and their band intensity (**G**) of NICD-4 in LECs and BECs in response to laminar flow at 2 dyne/cm^2 for the indicated time.

(**H**) Prox1 protein level was not altered in LECs that were exposed to laminar flow (2 dyne/cm^2).

(**I**) The biomimetic sprouting assay shown in Fig.1F was performed on BECs. Intraluminal laminar flow (5 dyne/cm^2) was applied onto a layer of BECs lining the inner wall of the vascular-mimetic channels made in collagen gel. Scale bars: 100 μm. Relative sprout number and length were graphed.

Error bars represent standard deviation (SD). Statistical values: n.s., not significant; *, $p < 0.05$; **, $p < 0.01$; ***, $p < 0.001$.

Supplemental Figure 2. Quantitation of the effect of siRNA-mediated knockdown of ORAI1.

Intensity of NICD-1 bands in LECs (**A**) and BECs (**B**) after siRNA-mediated knockdown of ORAI1 shown in Fig.2C was quantified and charted. (**C**) Laminar flow-induced calcium influx was measured in LECs transfected with either scrambled siRNA (siCTR) or ORAI1 siRNA (siOrai1) for 24 hr., followed by laminar flow (2 dyne/cm^2). Calcium signals were captured by a time-lapse microscope and the relative signal intensity was plotted. Error bars represent standard deviation (SD). Statistical values: **, $p < 0.01$; ***, $p < 0.001$.

Supplemental Figure 3. Defective lymphatic development in Orai1 KO embryo. (A-H) Low magnification images of the Cd31/Lyve1-stained back skins of Orai1 wild type (+/+) and KO (-/-) embryos

(E15.5). Two sets (#1 and #2) of wild type (**A-D**) and KO (**E-H**) embryos from two different litters are shown. Scale bars: 200 μm. **(I)** Relative calibers of lymphatic vessels in Orai1 wild type vs. KO embryos. Error bars represent standard deviation (SD). Statistical values: *, $p < 0.05$; **, $p < 0.01$; ***, $p < 0.001$

Supplemental Figure 4. Sequence-based prediction of a putative CaM-binding site in the N-terminus of PROX1 (**A**) A potential CaM binding site was identified in the N-terminal area of PROX1 by the Camodulin Target Database Binding Site Search algorithm, established by the Mitsu Ikura Lab (Ontario Cancer Institute, Canada). Probability scores (from 0 to 9) were shown below each amino acid residue. The putative CaM binding site mapped between 5^{th} and 37^{th} amino acid in PROX1 is underlined. (**B**) Diagram of GST-PROX1 fragments. The N-terminus of each PROX1 fragment was fused to GST protein (empty circle) for bacterial expression and purification. The location of each end is shown. NR, nuclear receptor binding motif; Homeo, homeodomain.

Supplemental Figure 5. Quantitation of western blot bands. Intensity of western blot bands in Figs.4 and 5 was measured, normalized and graphed. (**A**) Band intensity of Prox1 proteins that were immunoprecipitated by anti-HA antibody in Fig.4E was quantitated. (**B**) Band intensity of CaM proteins that were co-precipitated with Prox1 in Fig.4F was quantitated using the short exposure. (**C**) Band intensity of Myc-Prox1 proteins that were co-precipitated with FLAG-KLF2 in Fig.5B was quantitated. (**D**) Band intensity of Myc-Prox1 proteins that were co-precipitated with FLAG-KLF2 in the absence (Empty) or presence (HA-CaM) of CaM protein in Fig.5C was quantitated.

Supplemental Figure 6. PROX1 binds with GCamP3, but with GFP. An expression vector encoding GCaMP3 or GFP was co-transfected with a vector expressing Myc-PROX1 into HEK293 cells. After 48 hours, GFP or GCaMP3 was immunoprecipitated from the cell lysates using anti-GFP antibody or normal rabbit IgG as a negative control, which were then blotted with anti-Myc or anti-GFP antibody. Note that only GCaMP3, not GFP, was immunoprecipitated with PROX1.

Supplemental Figure 7. Nuchal edema in endothelial-specific Klf2 KO embryos. Wild type and endothelial-specific Klf2 KO embryos (Klf2 ^{ECKO}) resulted from crossing the Cdh5(PAC)-CreER^{T2} mice and Klf2 $^{fl/fl}$ mice are shown at E15.5. Two different litters are shown (#1 and #2). Klf2 ^{ECKO} was induced in pregnant females by intraperitoneal injection of tamoxifen (1.5 mg) at E11.5 and E13.5. Arrowheads mark nuchal edema. Dermal lymphatics were often filled with blood as shown in the white box.

Supplemental Figure 8. Low-power images of the back skins of wild type and Klf2 ^{ECKO} embryos of Fig.5l. Overview low-magnification images of lymphatic vessels (shown by EGFP) and blood vessels (stained with Cd31) demonstrate the vascular defects caused by genetic ablation of Klf2 in endothelial cells.

Supplemental Figure 9. Regulation of DTX1 and DTX3L protein expression in LECs *vs.* BECs by laminar flow. Western blot assays showing the regulation of protein expression of DTX1 (**A**) and DTX3L (**B**) in LECs and BECs after exposure to laminar flow (2 dyne/cm^2) for 0 (Static), 12 or 24 hr.. These protein expression data are consistent with their mRNA expression patterns shown in Fig.6 A and B, respectively.

Supplemental Figure 10. Synergistic downregulation of NICD-1 by DTX1 and DTX3L. Western blot bands for NICD-1 shown in Fig.6 E, F, and G were quantified and charted in panels **A**, **B**, and **C**, respectively. Statistical values: *, $p < 0.05$; **, $p < 0.01$; ***, $p < 0.001$.

Supplemental Figure 11. Low-power images of the back skins of wild type *vs.* Dtx3L knockout embryos. Overview low-magnification images for Lyve1 show defective lymphatic sprouting in Dtx3L KO embryos at E15.5. Total > 4 embryos per genotype harvested from at least 3 independent litters were analyzed for the study.

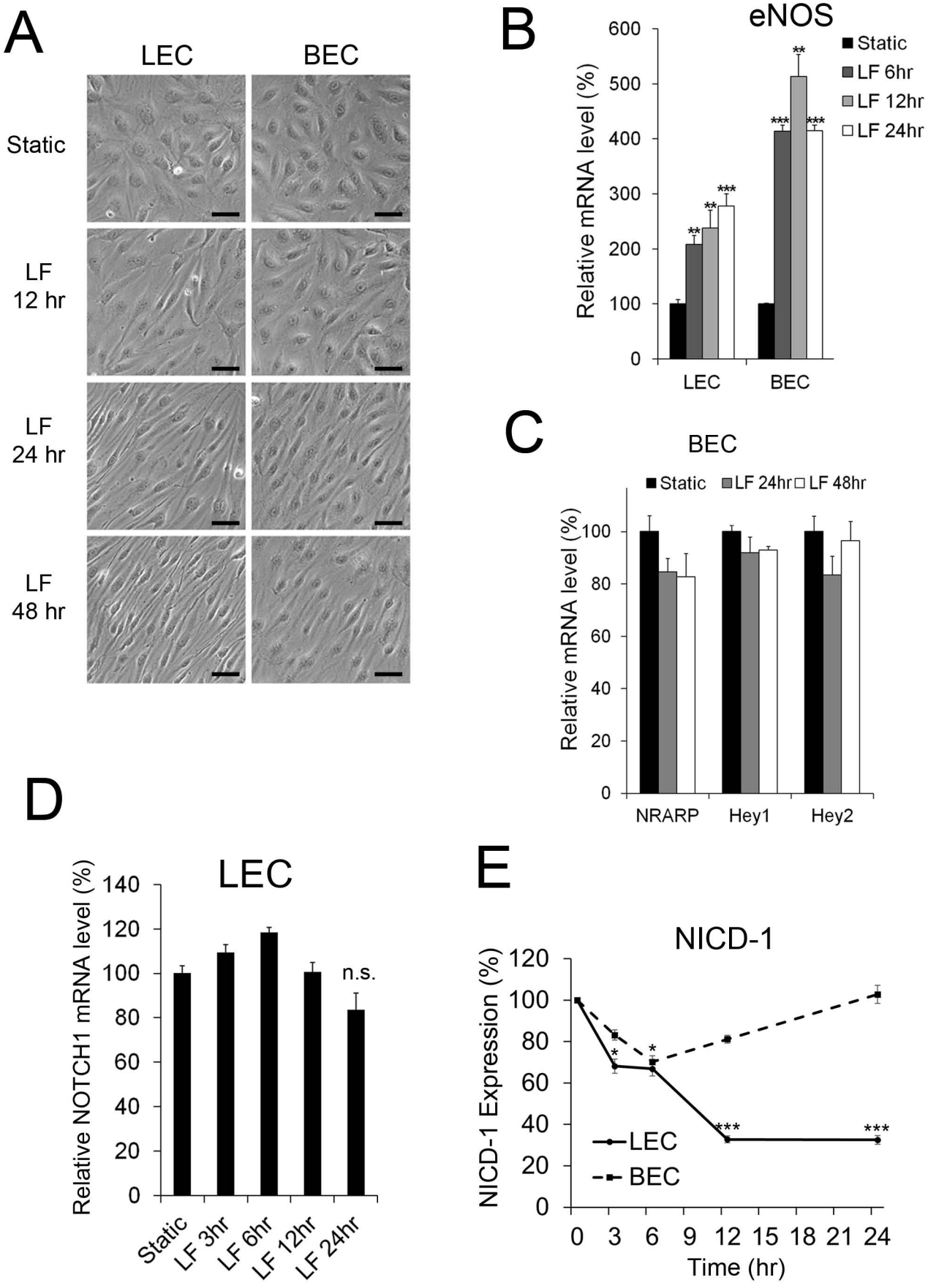

Supplemental Figure1 (Part1)

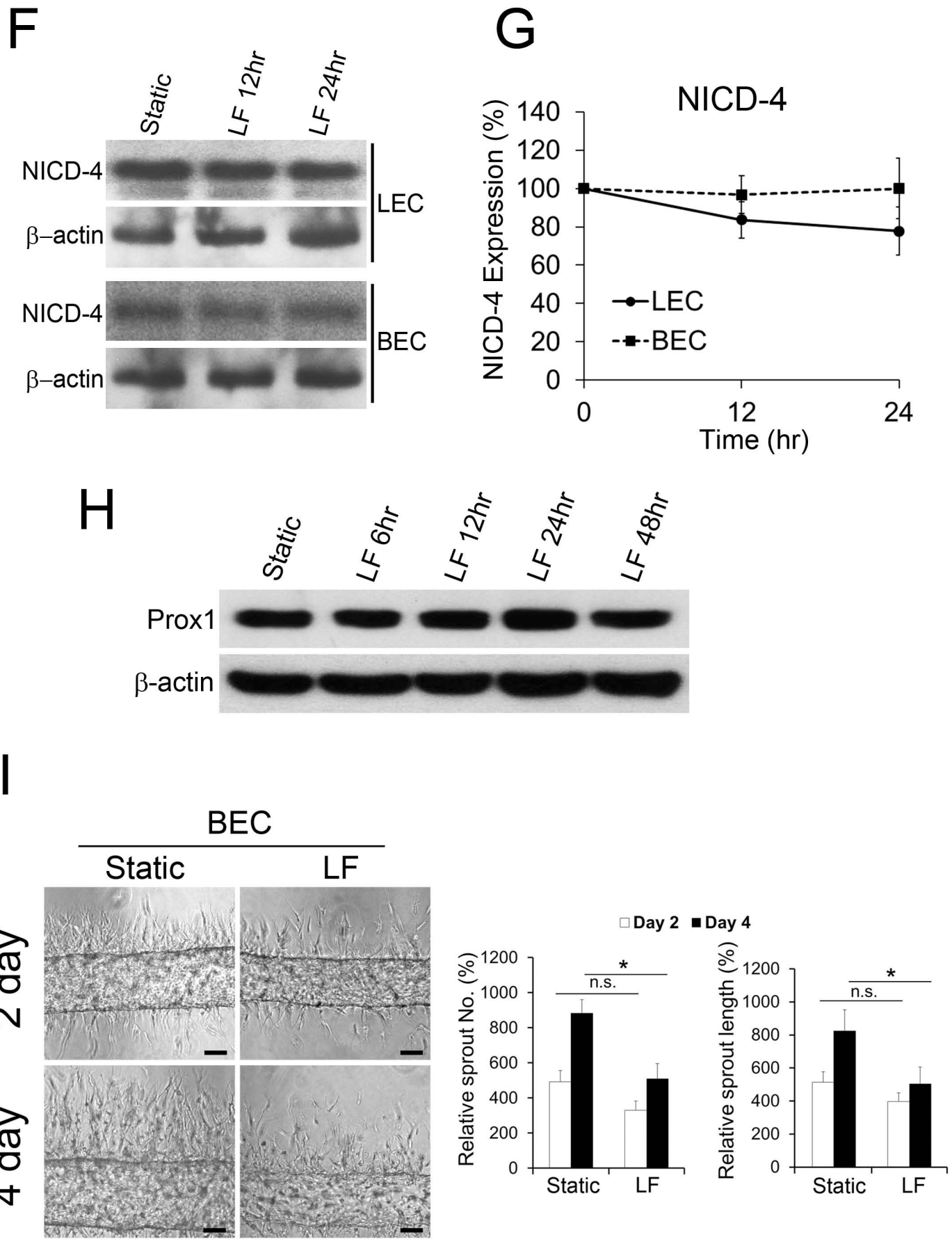

Supplemental Figure 1 (Part2)

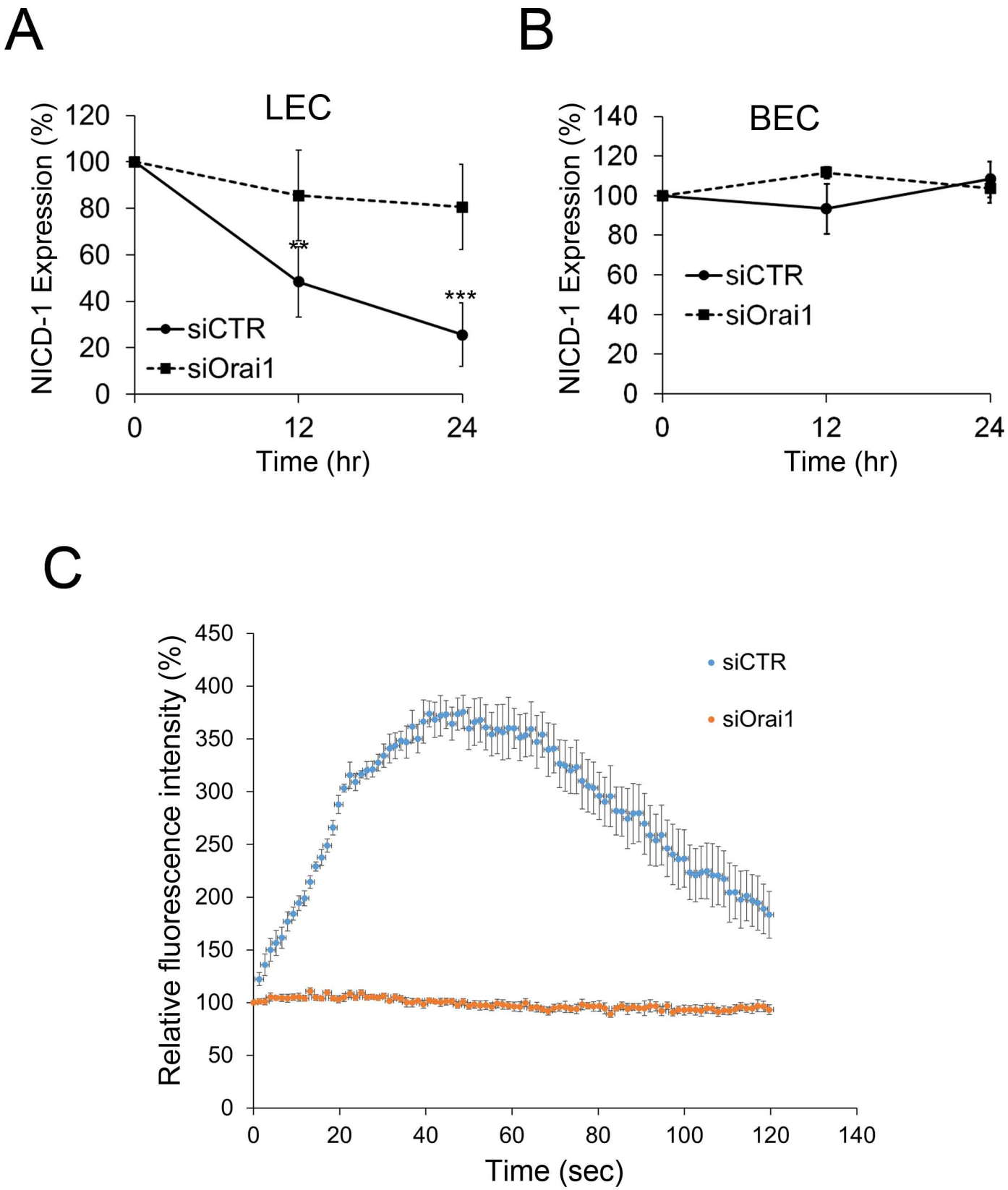

Supplemental Figure 2

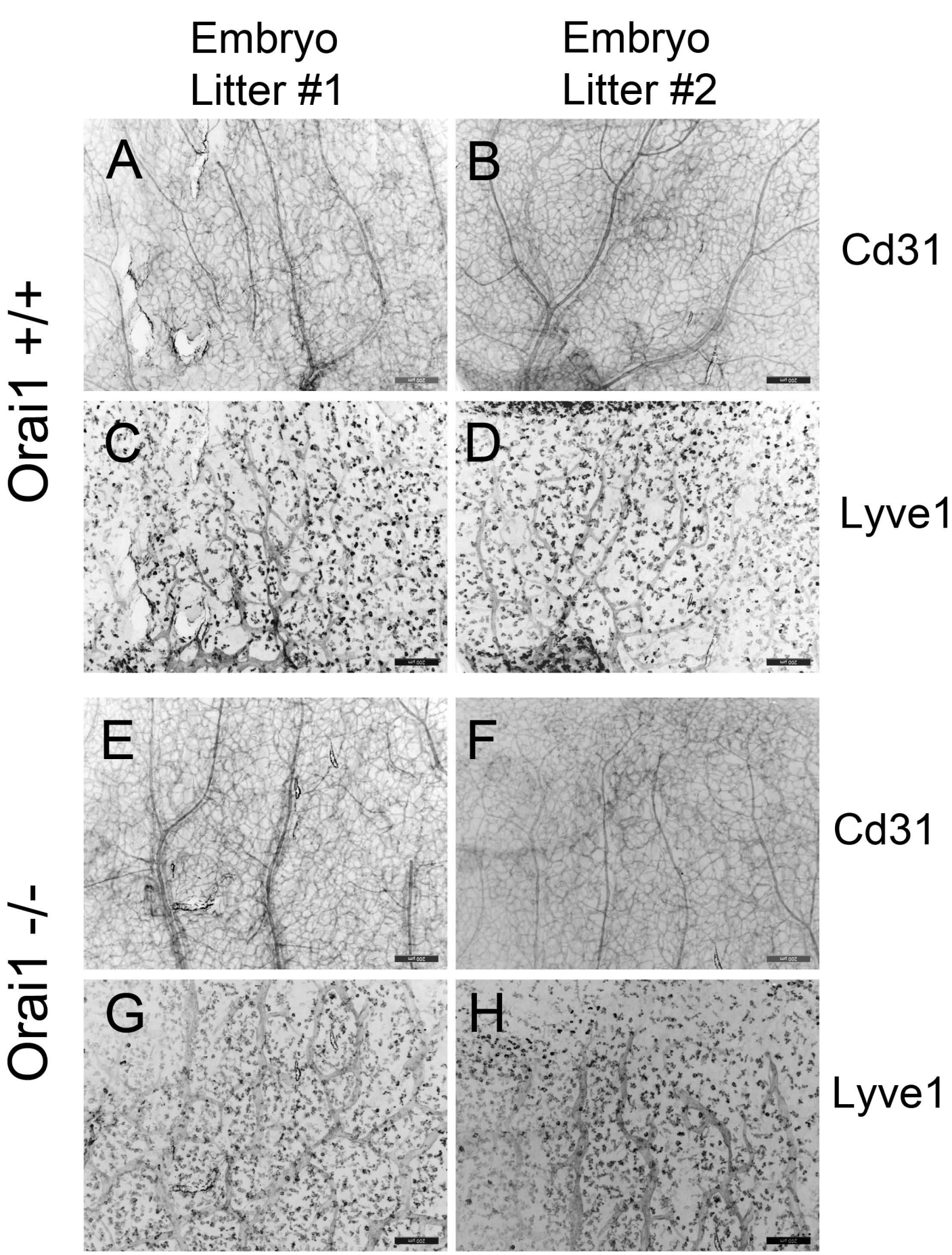

Supplemental Figure 3 (Part1)

I

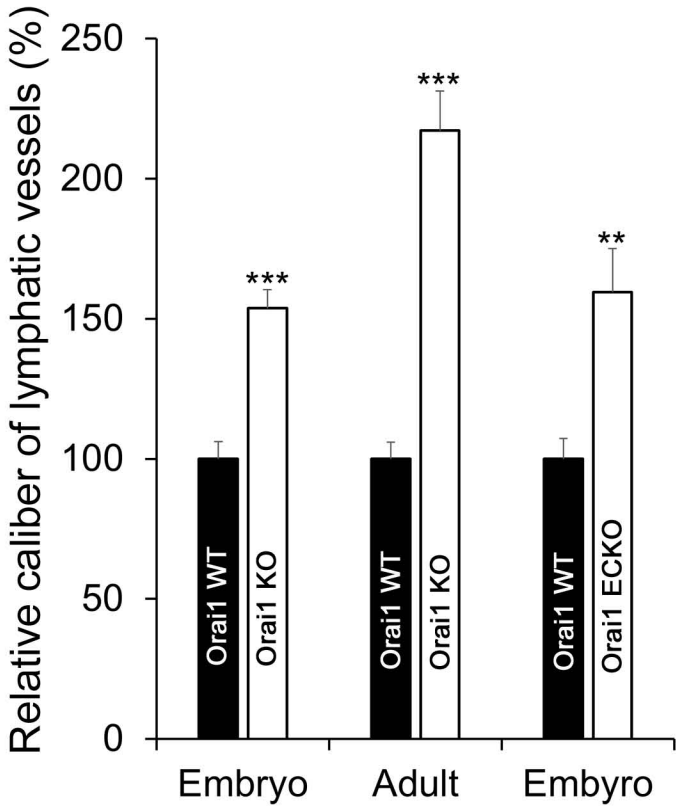

Supplemental Figure 3 (Part2)

A

```
....1 MPDHDSTALL SRQTKRRRVD IGVKRTVGTA SAFFAKARAT FFSAMNPQGS
..... 0000111233 4566789999 9999988766 5433211000 0000000000

...51 EQDVEYSVVQ HADGEKSNVL RKLLKRANSY EDAMMPFPGA TIISQLLKNN
..... 0000000000 0000000000 0000000000 0000000000 0000000000

..101 MNKNGGTEPS FQASGLSSTG SEVHQEDICS NSSRDSPPEC LSPFGRPTMS
..... 0000000000 0000000000 0000000000 0000000000 0000000000

..151 QFDMDRLCDE HLRAKRARVE NIIRGMSHSP SVALRGNENE REMAPQSVSP
..... 0000000000 0000000000 0000000000 0000000000 0000000000

..201 RESYRENKRK QKLPQQQQQS FQQLVSARKE QKREERRQLK QQLEDMQKQL
..... 0000000000 0000000000 0000000000 0000000000 0000000000

..251 RQLQEKFYQI YDSTDSENDE DGNLSEDSMR SEILDARAQD SVGRSDNEMC
..... 0000000000 0000000000 0000000000 0000000000 0000000000

..301 ELDPGQFIDR ARALIREQEM AENKPKREGN NKERDHGPNS LQPEGKHLAE
..... 0000000000 0000000000 0000000000 0000000000 0000000000

..351 TLKQELNTAM SQVVDTVVKV FSAKPSRQVP QVFPPLQIPQ ARFAVNGENH
..... 0000000000 0000000000 0000000000 0000000000 0000000000

..401 NFHTANQRLQ CFGDVIIPNP LDTFGNVQMA SSTDQTEALP LVVRKNSSDQ
..... 0000000000 0000000000 0000000000 0000000000 0000000000

..451 SASGPAAGGH HQPLHQSPLS ATTGFTTSTF RHPFPLPLMA YPFQSPLGAP
..... 0000000000 0000000000 0000000000 0000000000 0000000000

..501 SGSFSGKDRA SPESLDLTRD TTSLRTKMSS HHLSHHPCSP AHPPSTAEGL
..... 0000000000 0000000000 0000000000 0000000000 0000000000

..551 SLSLIKSECG DLQDMSEISP YSGSAMQEGL SPNHLKKAKL MFFYTRYPSS
..... 0000000000 0000000000 0000000011 1111111111 1111111100

..601 NMLKTYFSDV KFNRCITSQL IKWFSNFREF YYIQMEKYAR QAINDGVTST
..... 0000000000 0000000001 1123333333 3333333332 1110000000

..651 EELSITRDCE LYRALNMHYN KANDFEVPER FLEVAQITLR EFFNAIIAGK
..... 0000000000 0000000000 0000000000 0000000000 0000000000

..701 DVDPSWKKAI YKVICKLDSE VPEIFKSPNC LQELLHE
..... 0000000000 0000000000 0000000000 0000000
```

B

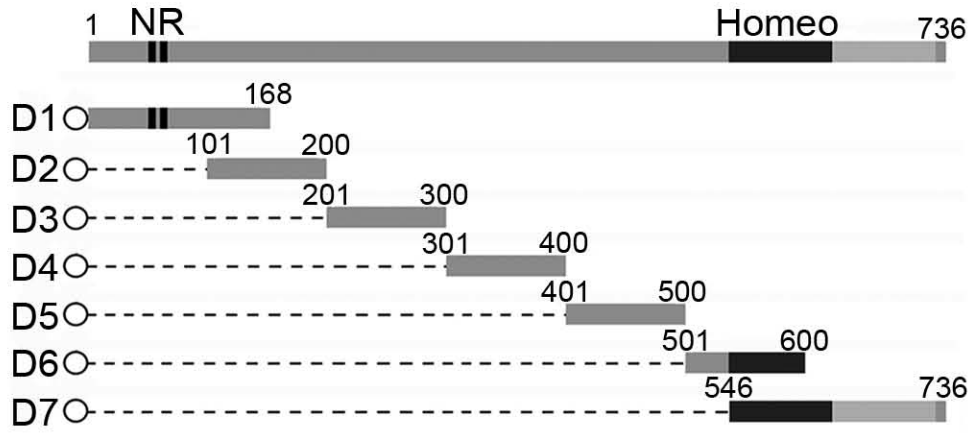

Supplemental Figure 4

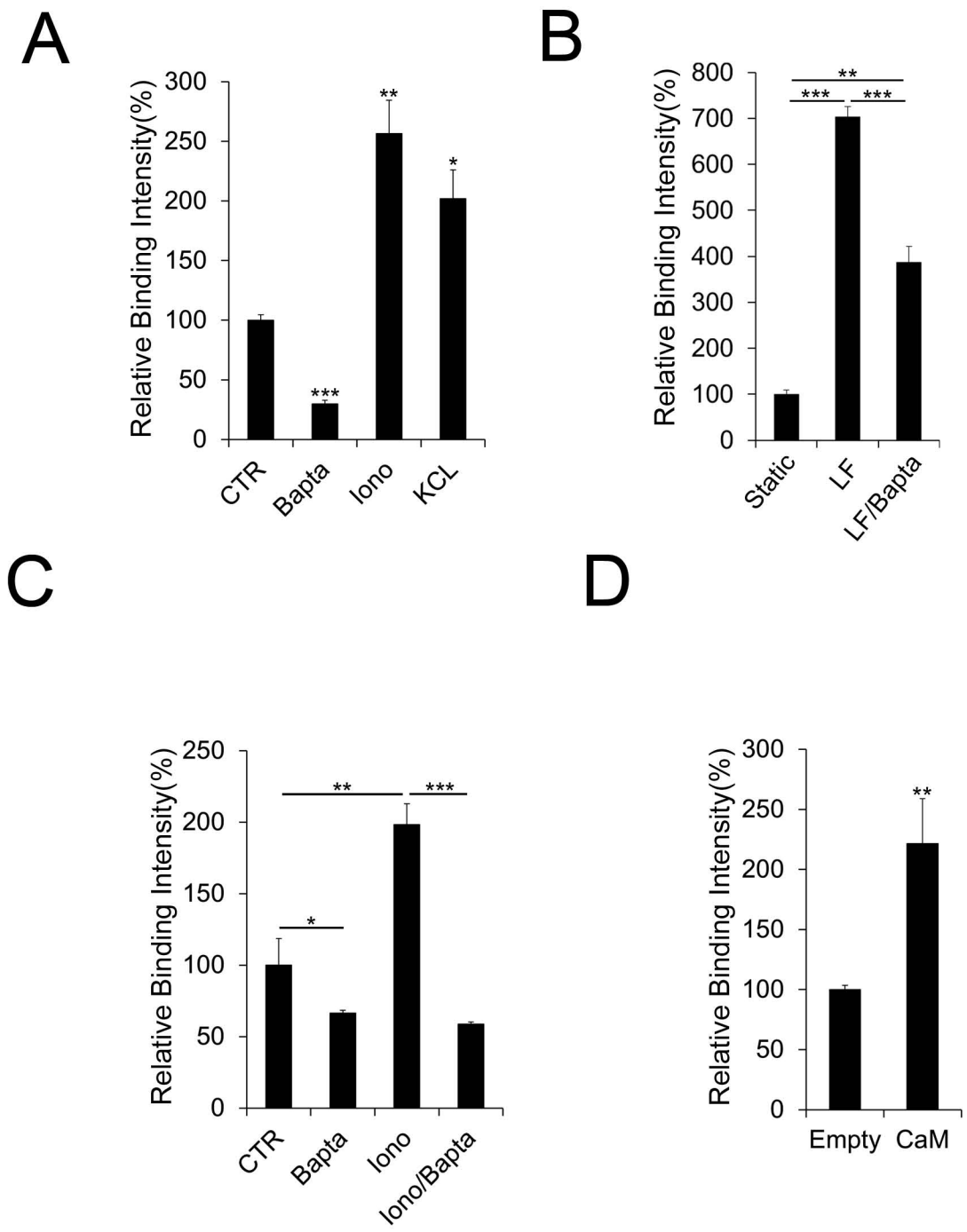

Supplemental Figure 5

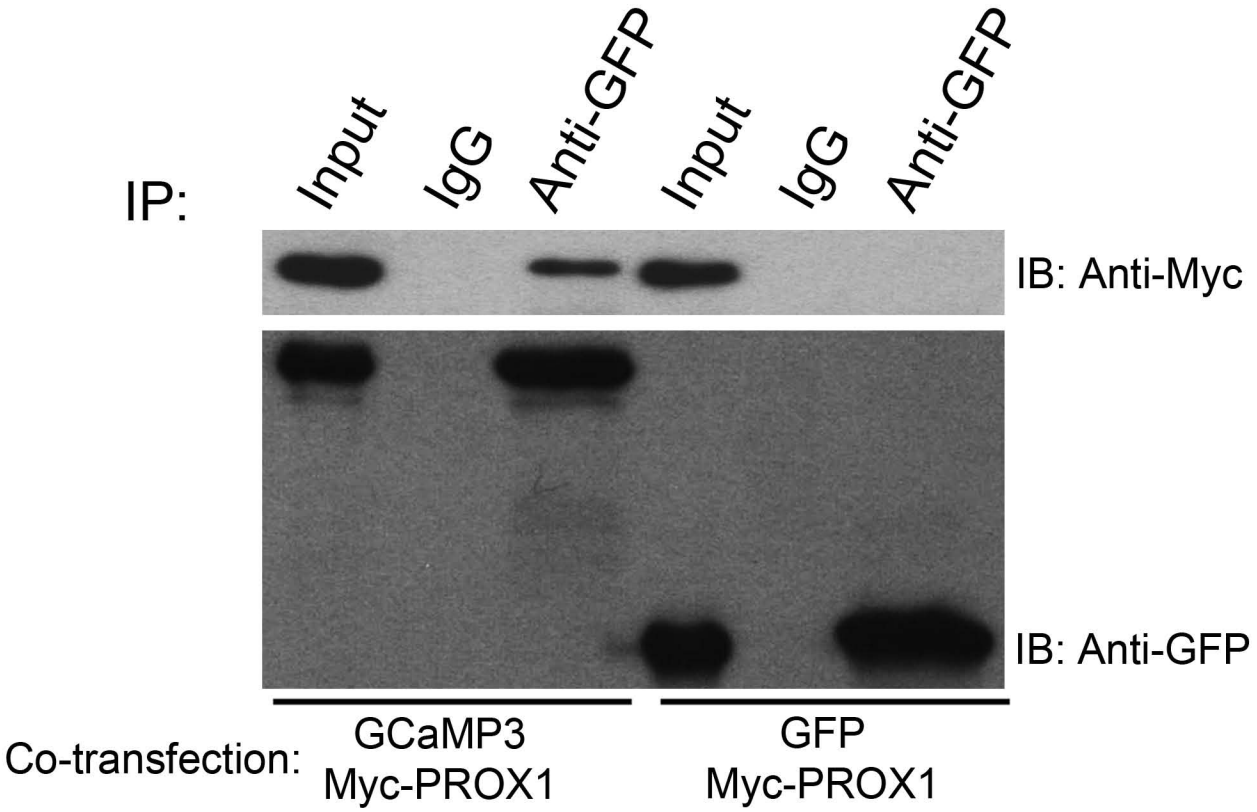

Supplemental Figure 6

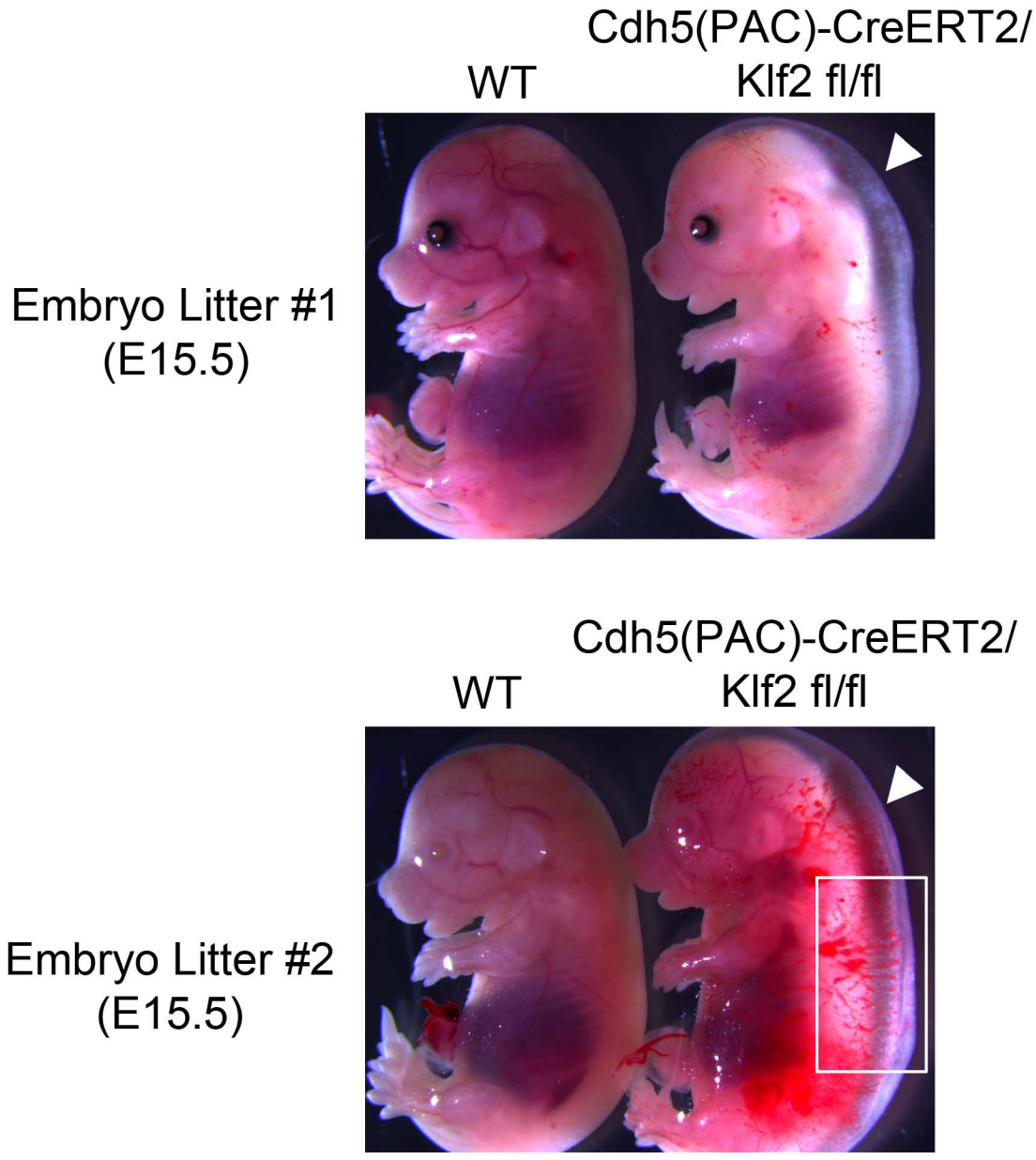

Supplemental Figure 7

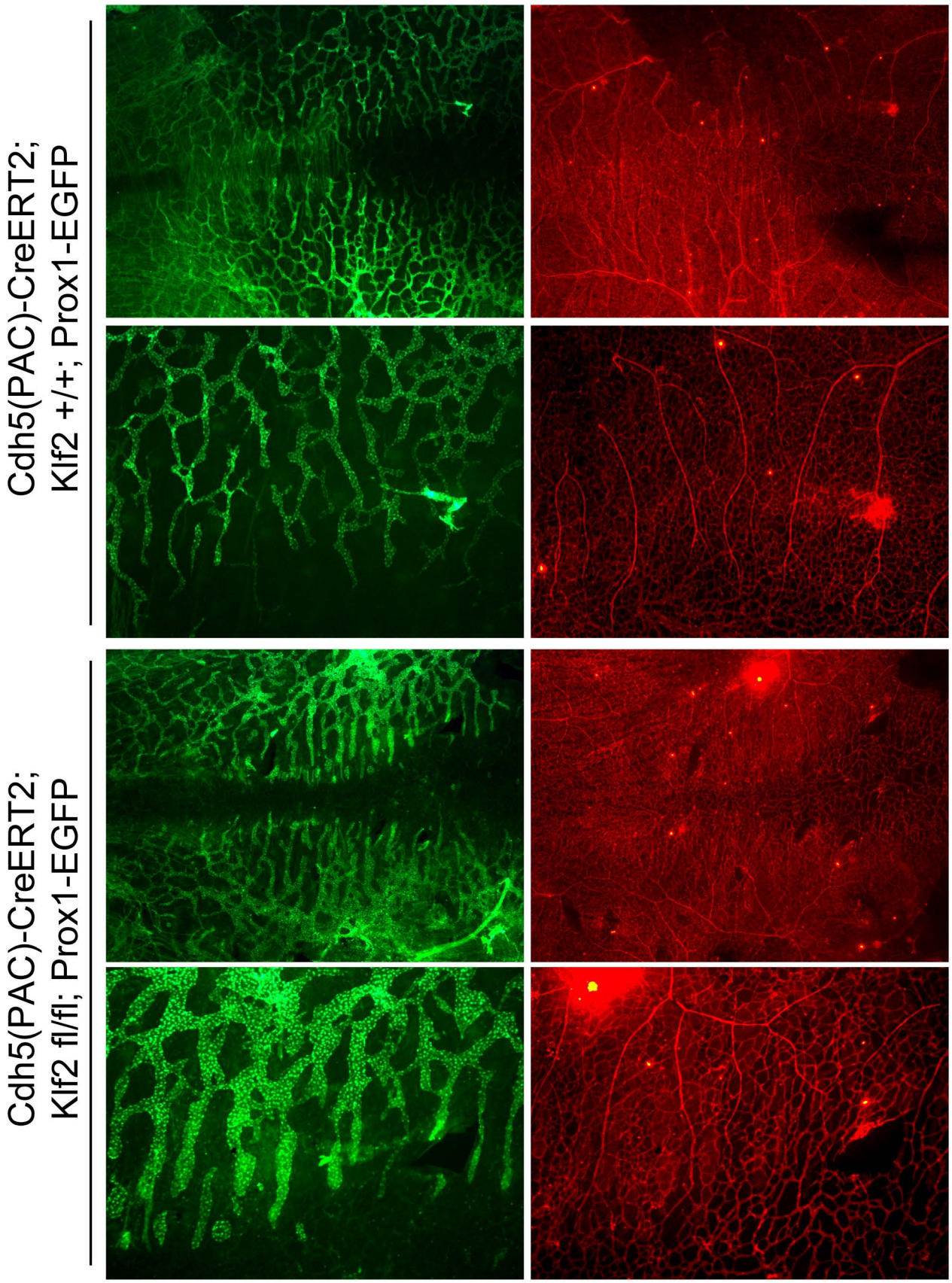

Supplemental Figure 8

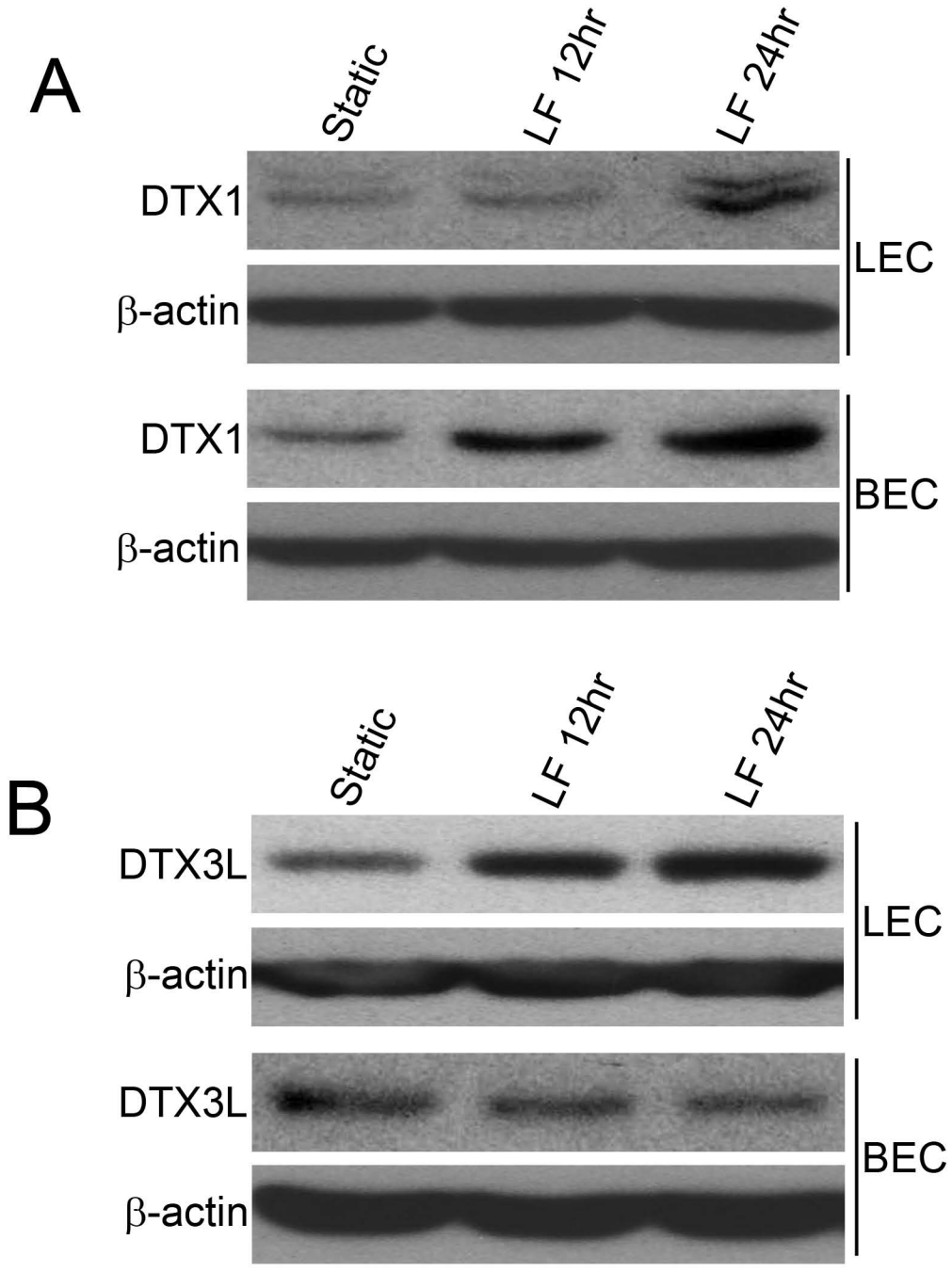

Supplemental Figure 9

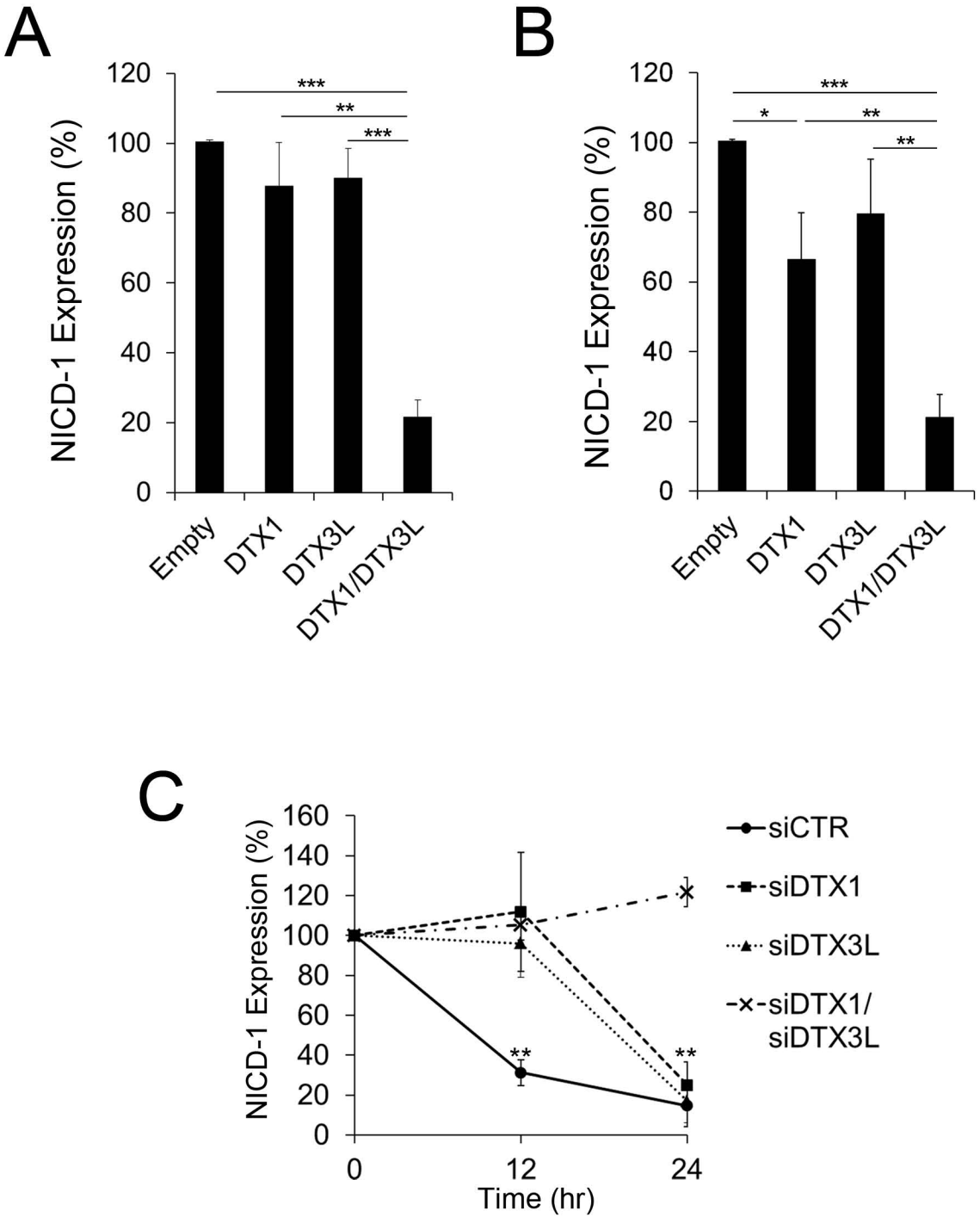

Supplemental Figure 10

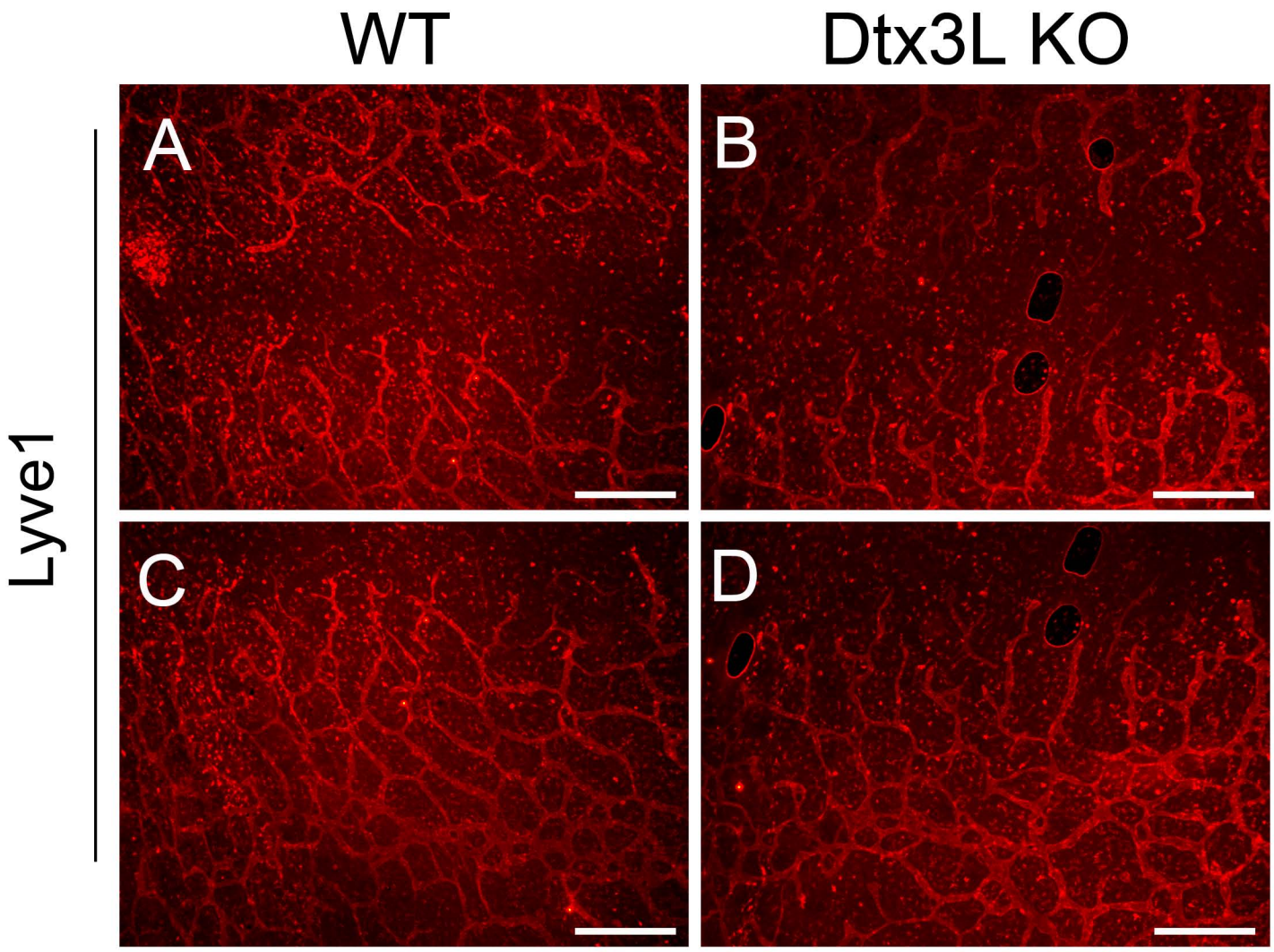

Supplemental Figure 11

Supplemental Table1. Sources of Antibodies

anti-PROX1	Rabbit polyclonal antibody was generated by the authors using a peptide (AGKDVDPSWKKAIYKV), followed by affinity purification.
anti-β-actin	Sigma-Aldrich, AC-15
anti-CD31	BD Bioscience, MEC13.3
anti-LYVE-1	Abcam, ab14917
	Angiobio, 11-034 (For mouse LEC isolation)
anti-Notch1	Santa Cruz Biotechnology, SC-6014
anti-Notch1 (cleaved at Val1744)	Cell Signaling, Cat. No. 2421
anti-Notch4	Santa Cruz Biotechnology, SC-5594
anti-Myc tag	Cell Signaling, Cat. No. 2272
	Santa Cruz Biotechnology, SC-40
anti-FLAG tag	Sigma-Aldrich, F7425, F1804
anti-HA tag	Santa Cruz Biotechnology, SC-805
	GenScript, A01244
Biotinylated goat anti-rabbit IgG	Vector Laboratories, BA-1000

Supplemental Table 2. Sequences of primers and siRNA used for this study

Human CaM fragment

Forward Primer AAA GAT ATC ATG TAC CCA TAC GAT GTT CCA GAT TAC GCT ATG GCT GAT CAG CTG ACC GAA GAA

Reverse Primer AAA CTC GAG TCA TTT TGC AGT CAT CAT CTG TAC

PROX1-D1 (YH2722)

Forward Primer AA GAA TTC ATG CCT GAC CAT GAC AGC ACA

Reverse Primer AA GTC GAC GGT GCT GGG CGG GTG TGC TGG

PROX1-D2 (YH2075)

Forward Primer AA GAA TTC ATG AAC AAA AAT GGT GGC ACG

Reverse Primer AA GTC GAC GGG ACT CAC AGA CTG CGG GGC

PROX1-D3 (YH2076)

Forward Primer AA GAA TTC CGA GAA AGT TAC AGA GAA AAC

Reverse Primer AA GTC GAC GCA CAT CTC ATT ATC TGA CCT

PROX1-D4 (YH2077)

Forward Primer AA GAA TTC GAG CTA GAC CCA GGA CAG TTT

Reverse Primer AA GTC GAC GTG GTT TTC CCC ATT GAC TGC

PROX1-D5 (YH2078)

Forward Primer AA GAA TTC AAT TTC CAC ACC GCC AAC CAG

Reverse Primer AA GTC GAC GGG AGC ACC TAA TGG GCT CTG

PROX1-D6 (YH2079)

Forward Primer AA GAA TTC TCC GGC TCC TTC TCT GGA AAA

Reverse Primer AA GTC GAC GGA GCT GGG ATA ACG GGT ATA

PROX1-D7 (YH2080)

Forward Primer AA GAA TTC AAT ATG CTG AAG ACC TAC TTC

Reverse Primer AA GTC GAC CTA CTC ATG AAG CAG CTC TTG

Mouse Dtx3L

Forward Primer TTC ACC ATG GAC TAC AAA GAC GAT GAC GAC AAG GCT TCC AGT CCC GAC CCG CCG

Reverse Primer TAT GCG GCC GCT TAC TCA ATG CCT TTT GCT TTCA

Dtx3L-transgenic vector (YH3004)
Forward Primer GGC GTG TAC GGT GGG AGG
Reverse Primer GCT TTA ATT AAG GTT CTT TCC GCC TCA GAAG

PROX1 V19D Mutagenesis
Forward Primer CAA ACC AAG AGG AGA AGA GAT GAC ATT GGA GTG
Reverse Primer CCC TAC CGT CCT TTT CAC TCC AAT GTC ATC TCT

PROX1 I21D Mutagenesis
Forward Primer AAG AGG AGA AGA GTT GAC GAT GGA GTG AAA AGG
Reverse Primer TGC TGT CCC TAC CGT CCT TTT CAC TCC ATC GTC

PROX1 V23D Mutagenesis
Forward Primer AGA AGA GTT GAC ATT GGA GAT AAA AGG ACG GTA
Reverse Primer TGC AGA TGC TGT CCC TAC CGT CCT TTT ATC TCC

PROX1 V27D Mutagenesis
Forward Primer ATT GGA GTG AAA AGG ACG GAT GGG ACA GCA TCT
Reverse Primer CTT AGC AAA AAA TGC AGA TGC TGT CCC ATC CGT

PROX1 A30D Mutagenesis
Forward Primer AAA AGG ACG GTA GGG ACA GAT TCT GCA TTT TTT
Reverse Primer TGC TCT TGC CTT AGC AAA AAA TGC AGA ATC TGT

PROX1 A32D Mutagenesis
Forward Primer ACG GTA GGG ACA GCA TCT GAT TTT TTT GCT AAG
Reverse Primer AAA CGT TGC TCT TGC CTT AGC AAA AAA ATC AGA

PROX1 A33D Mutagenesis
Forward Primer GTA GGG ACA GCA TCT GCA GAT TTT GCT AAG GCA
Reverse Primer AAA AAA CGT TGC TCT TGC CTT AGC AAA ATC TGC

PROX1 A34D Mutagenesis
Forward Primer GGG ACA GCA TCT GCA TTT GAT GCT AAG GCA AGA
Reverse Primer ACT AAA AAA CGT TGC TCT TGC CTT AGC GAT AAA

siRNA for human ORAI1
UCACUGGUUAGCCAUAAGA

siRNA for human KLF2

CCAAGAGUUCGCAUCUGAAdTdT

siRNA for human DTX1

CCAAGAAGAAGCACCUUAAdTdT

siRNA for human DTX3L

GCCAAGACAUUGGAGAAGUdTdT

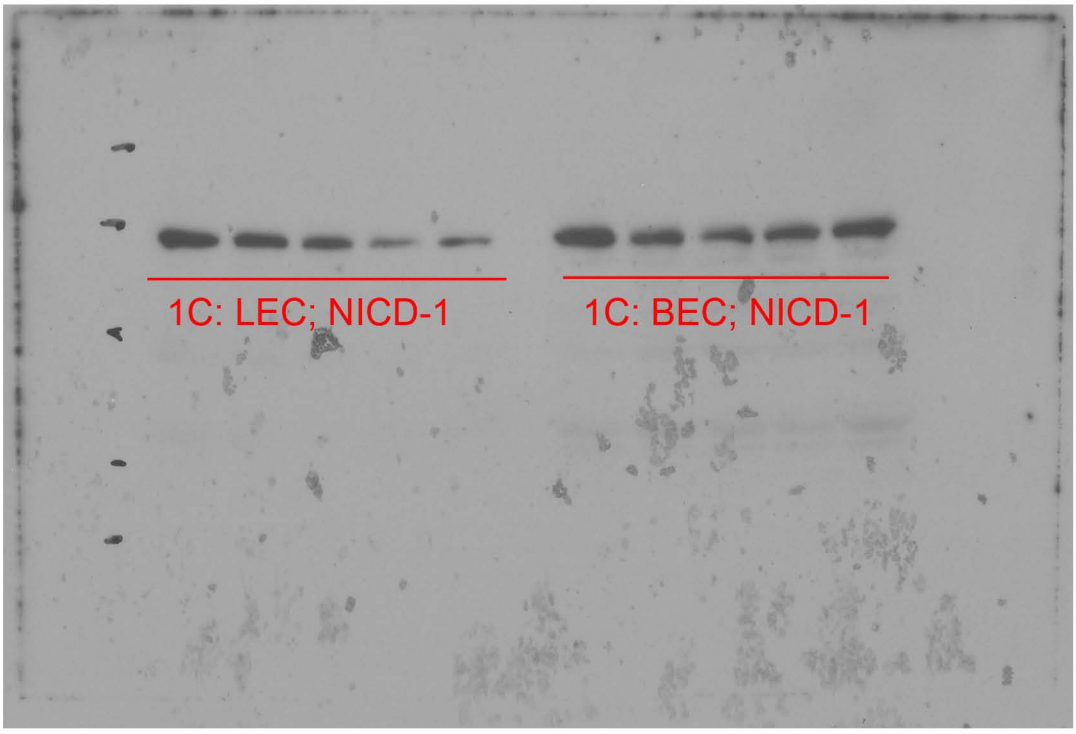

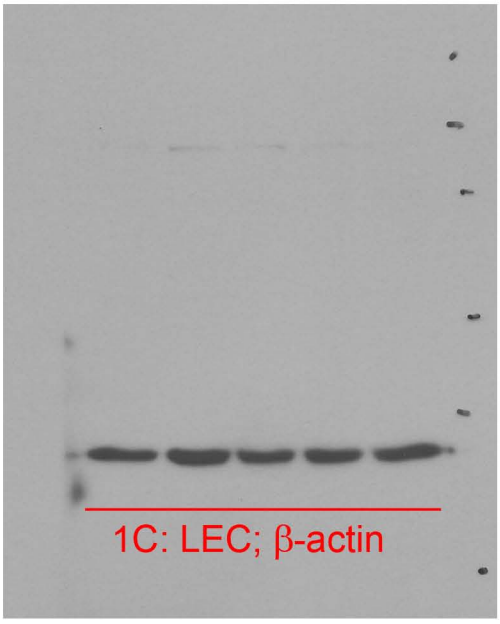

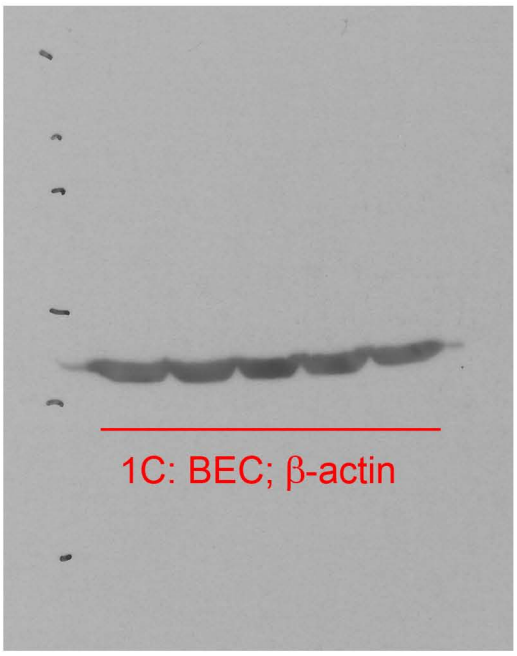

Full unedited gel for Figure 1C

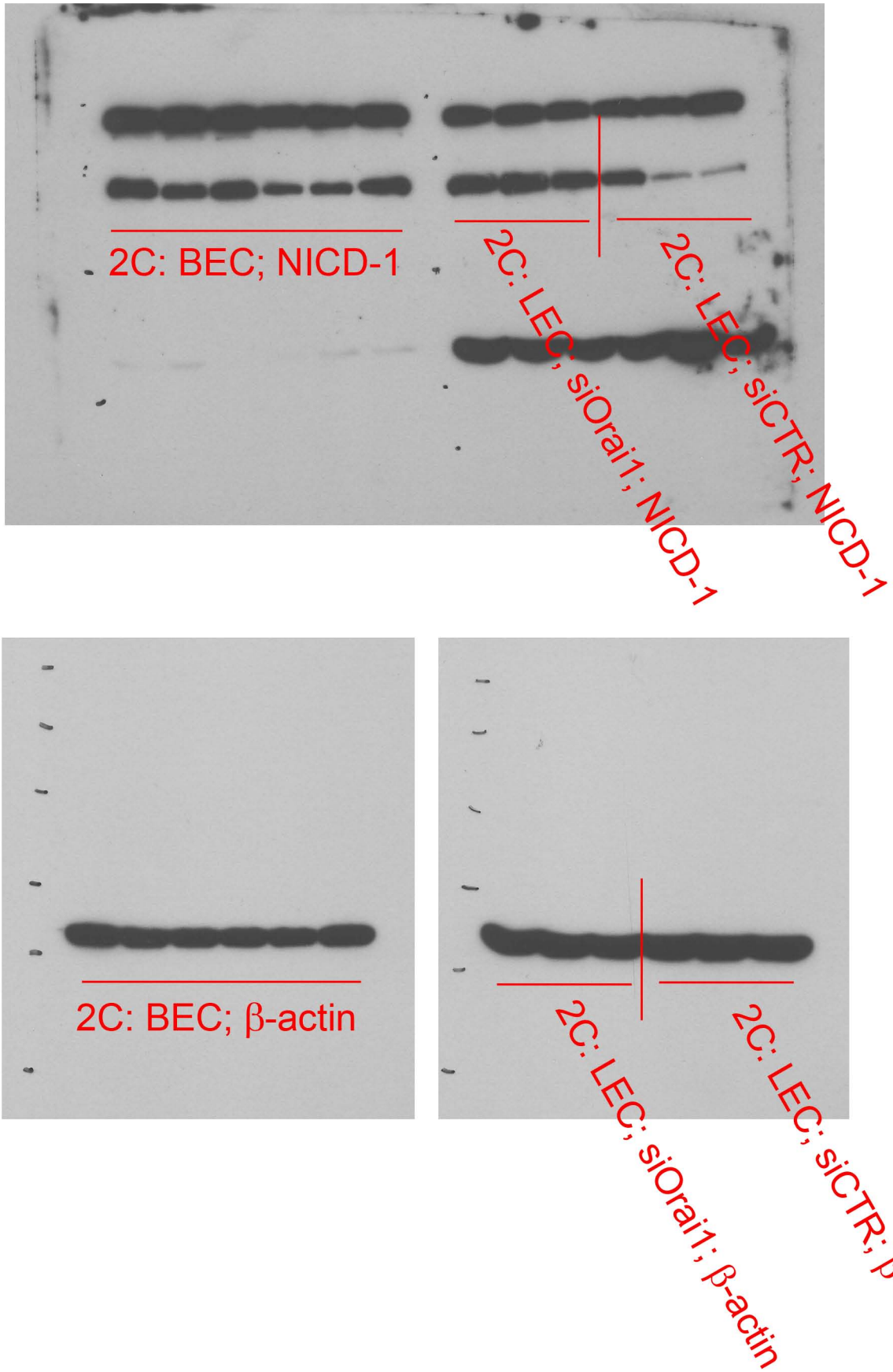

Full unedited gel for Figure 2C

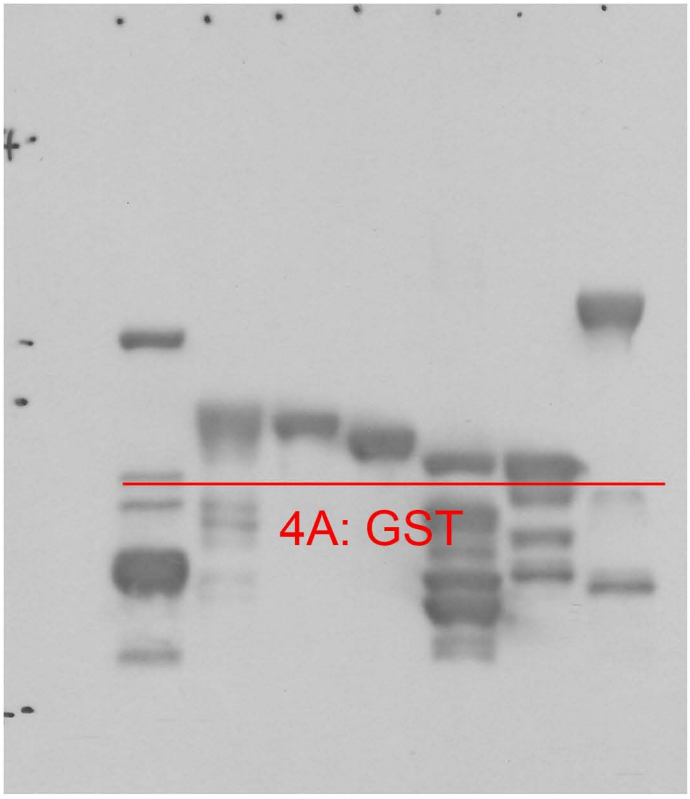

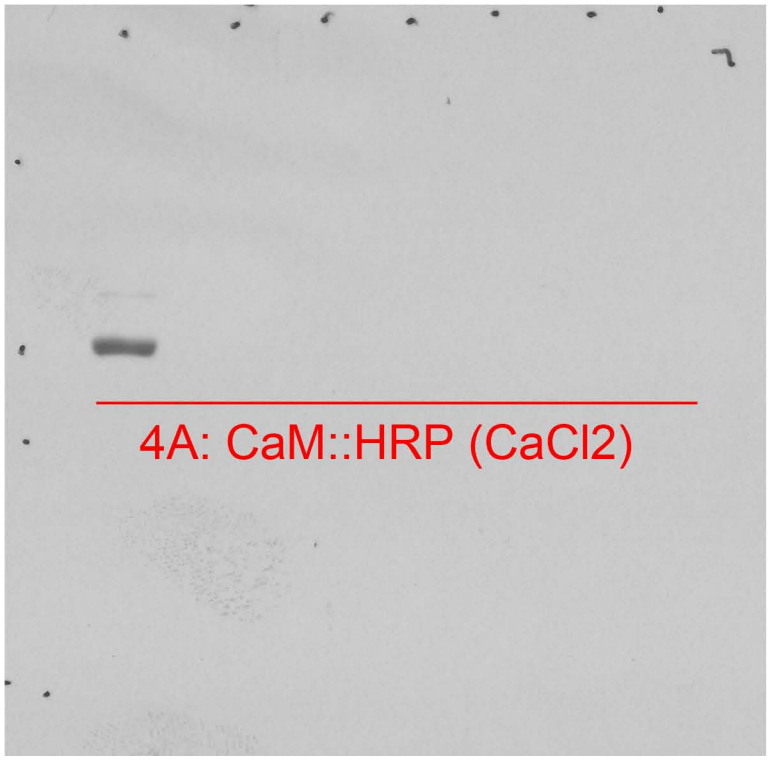

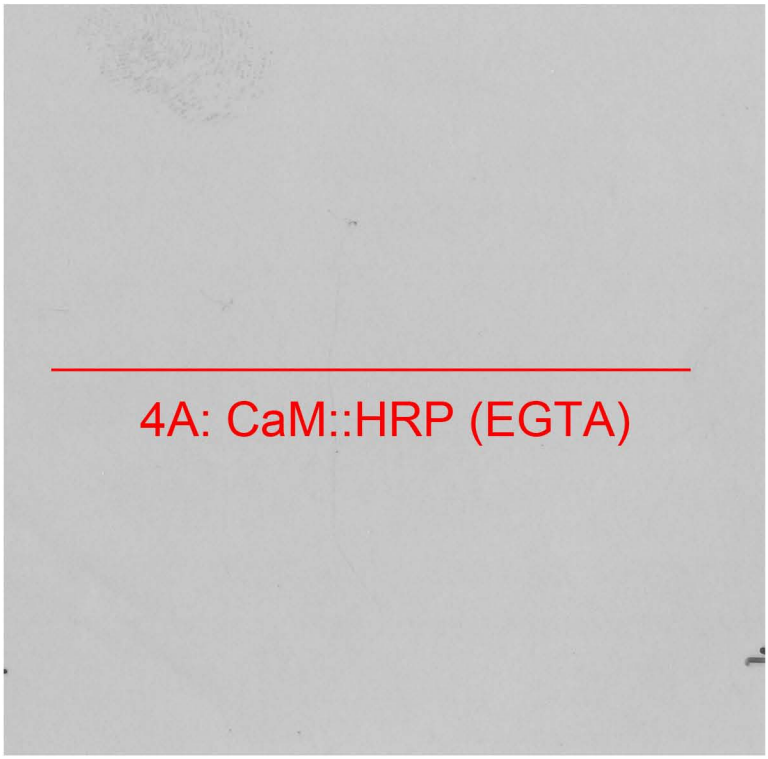

Full unedited gel for Figure 4A

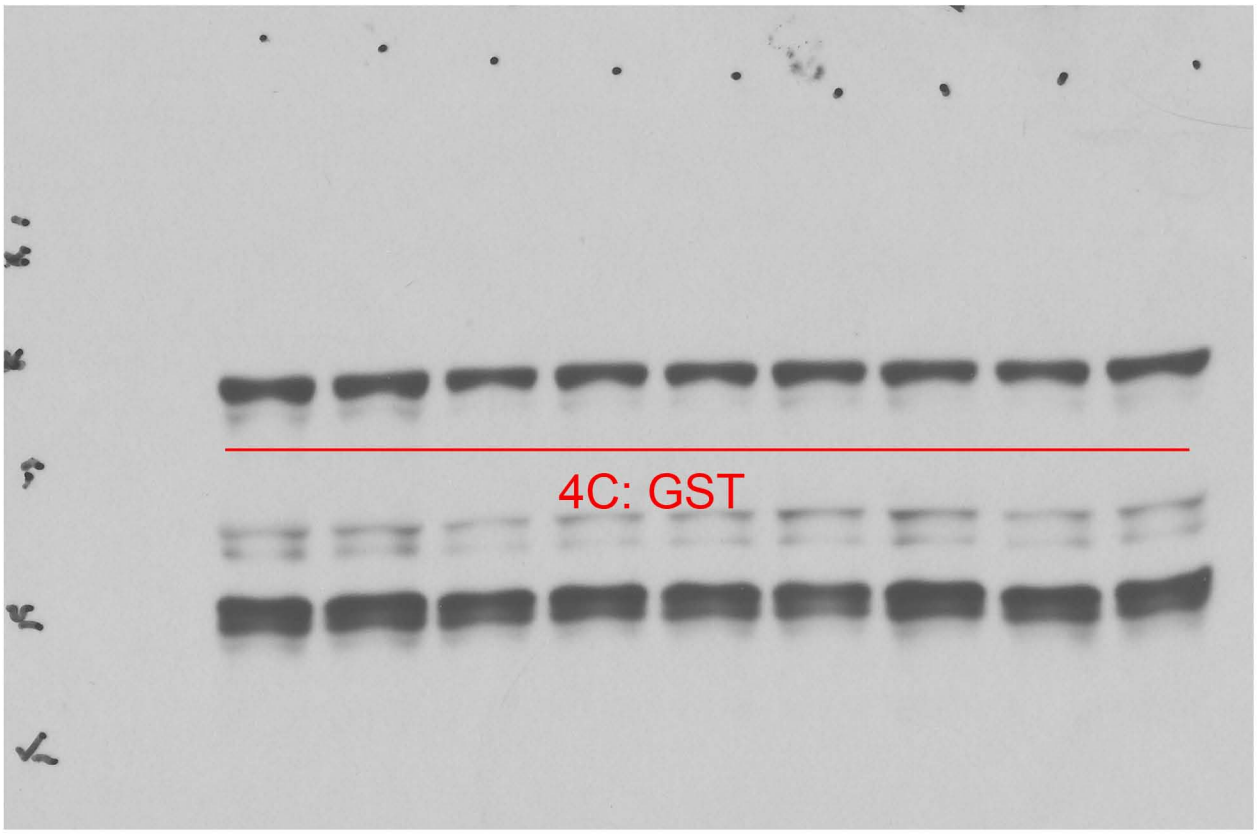

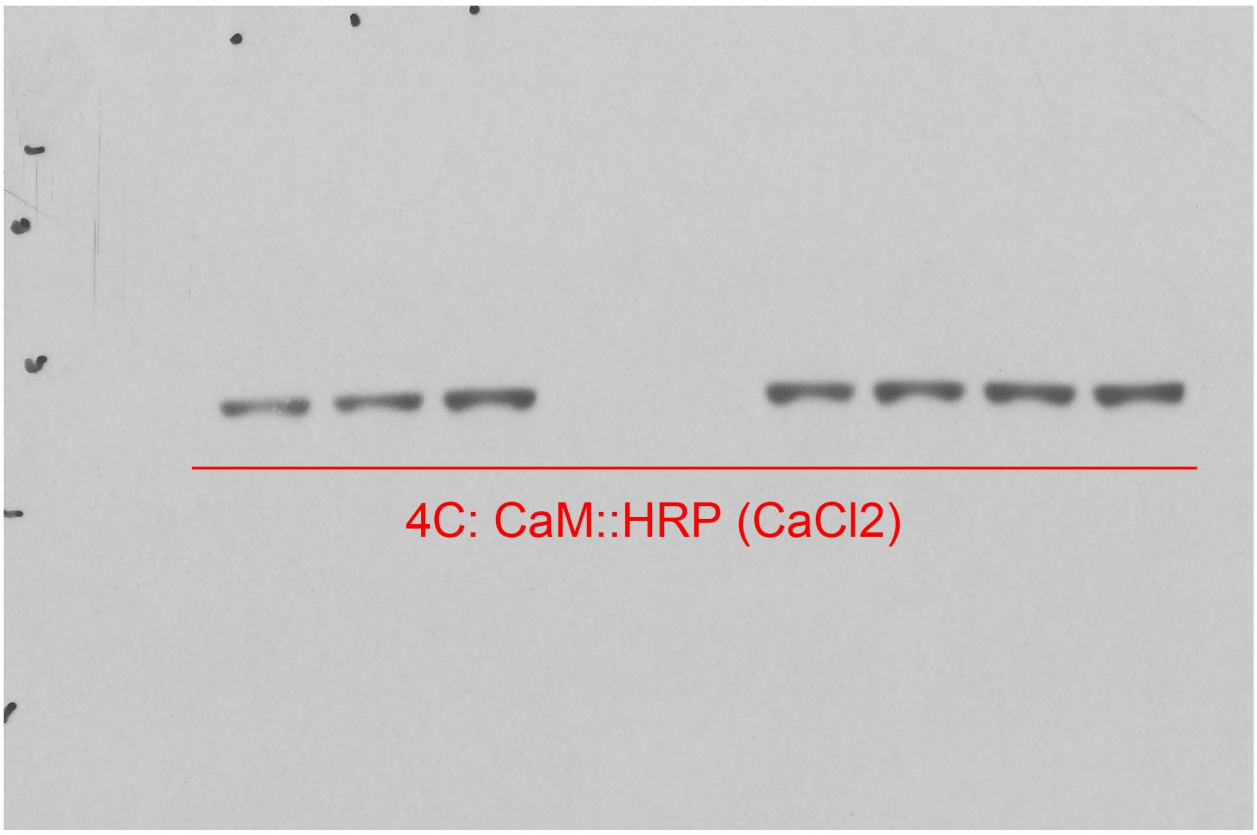

Full unedited gel for Figure 4C

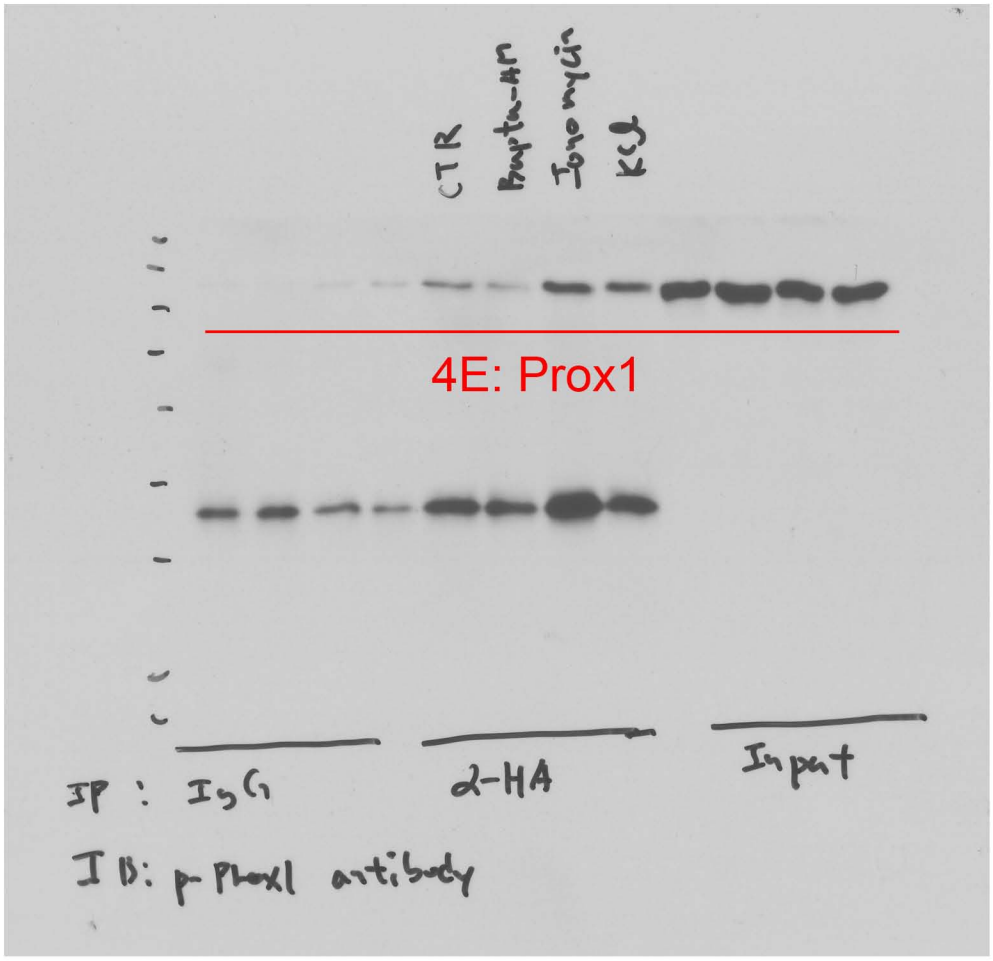

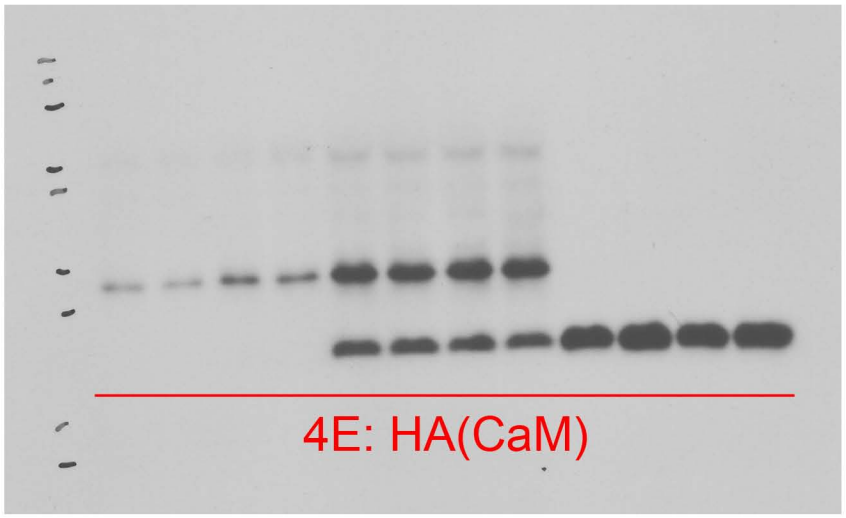

Full unedited gel for Figure 4E

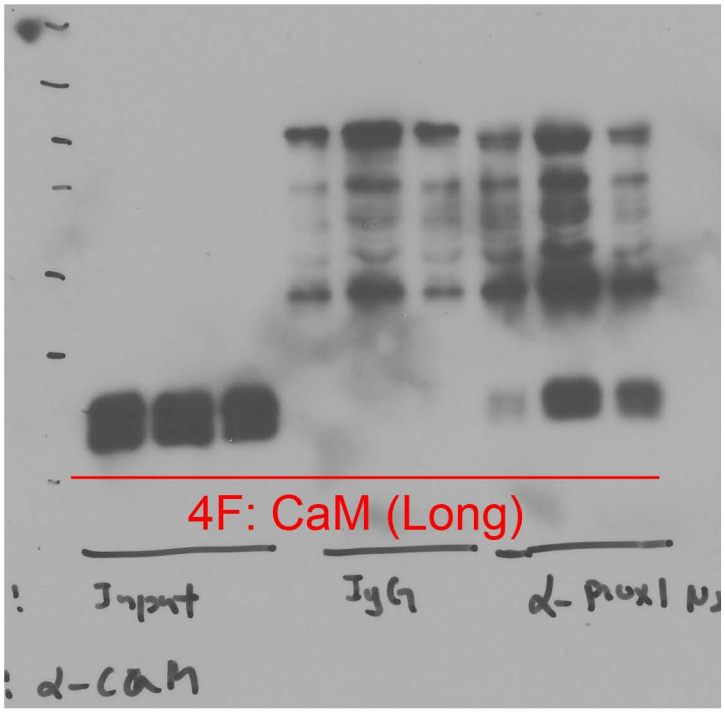

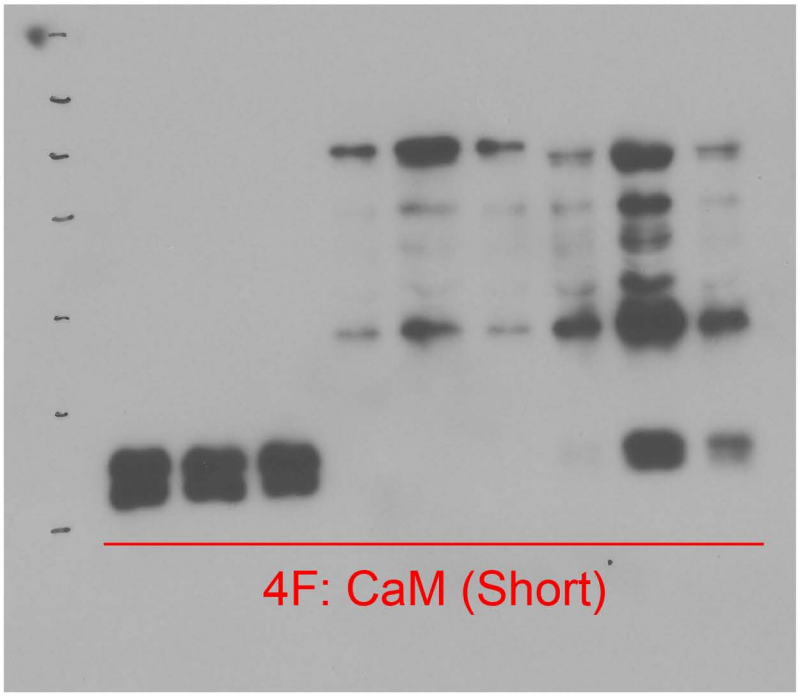

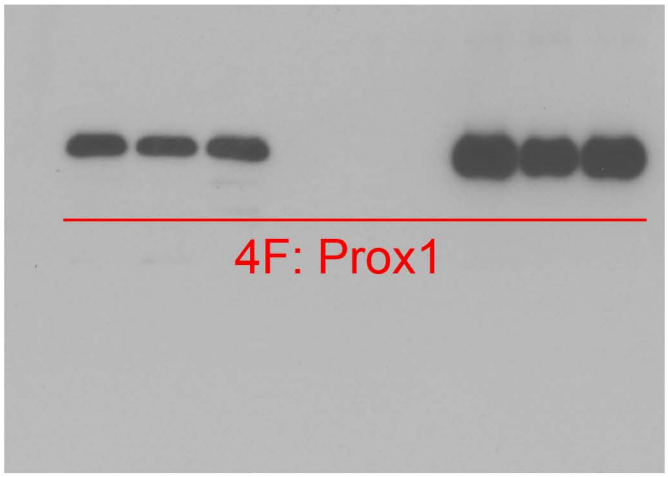

Full unedited gel for Figure 4F

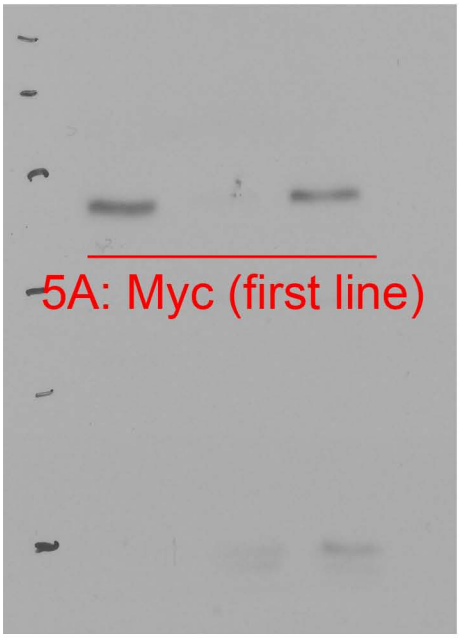

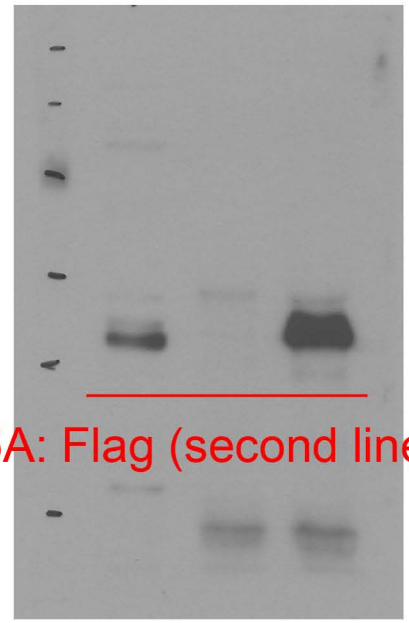

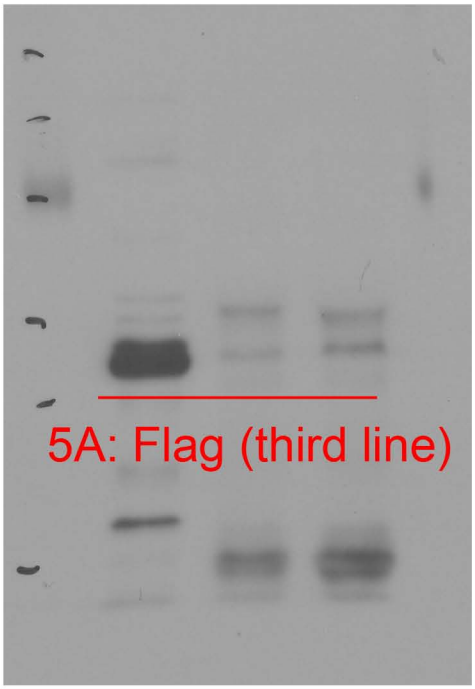

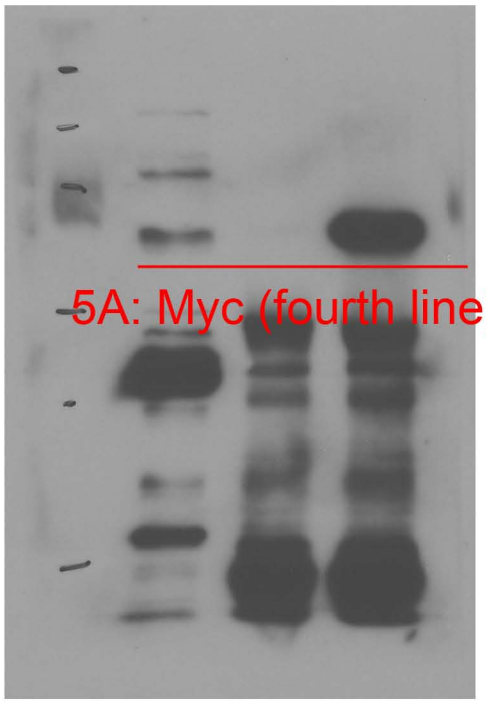

Full unedited gel for Figure 5A

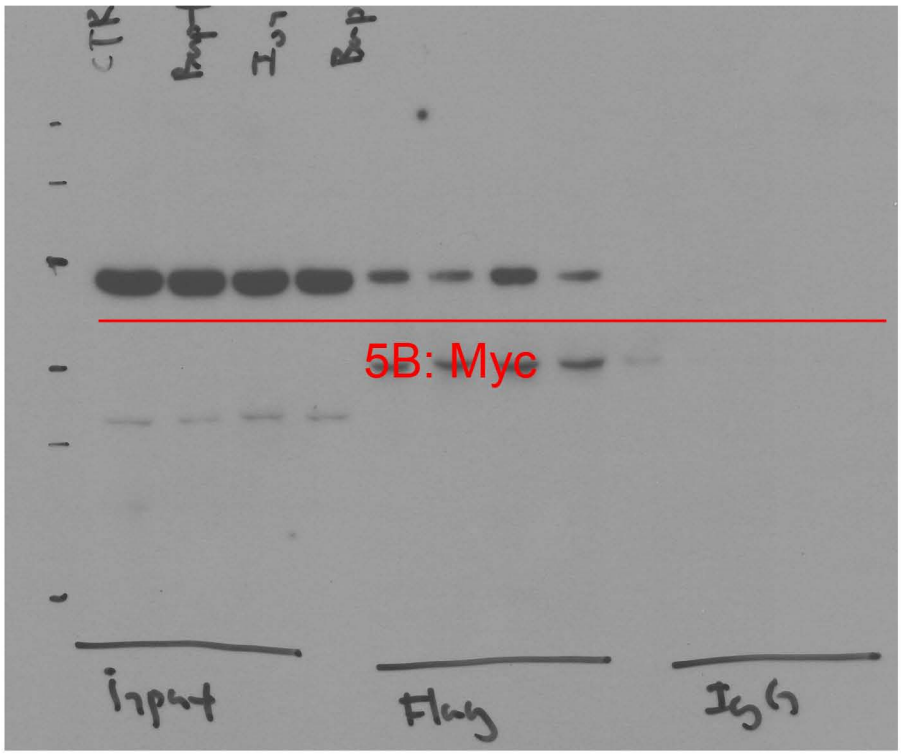

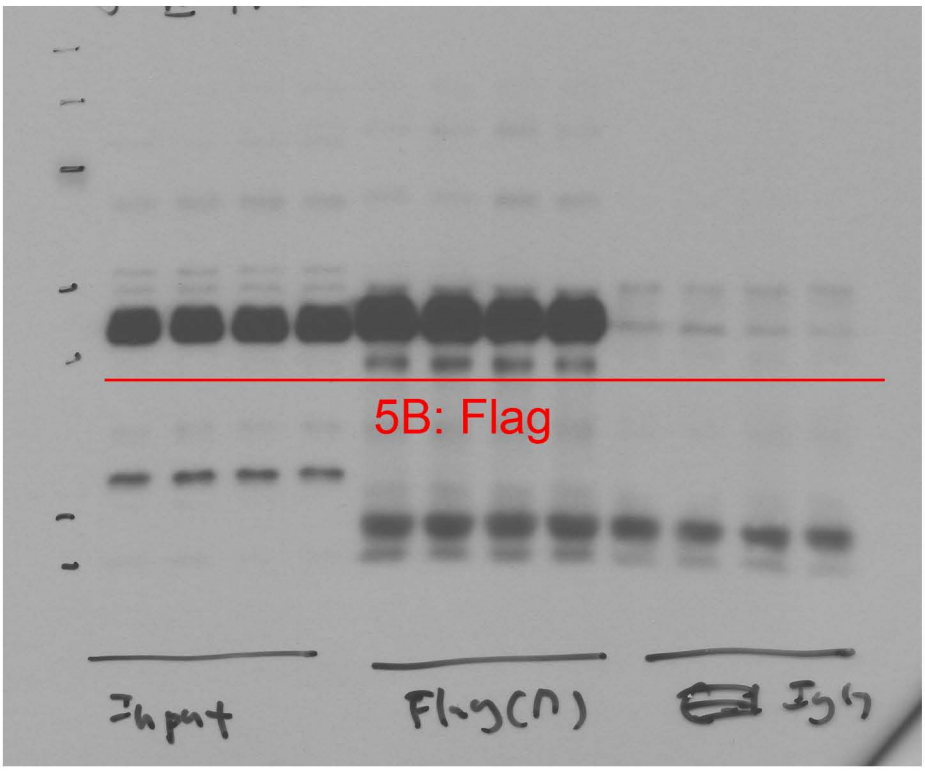

Full unedited gel for Figure 5B

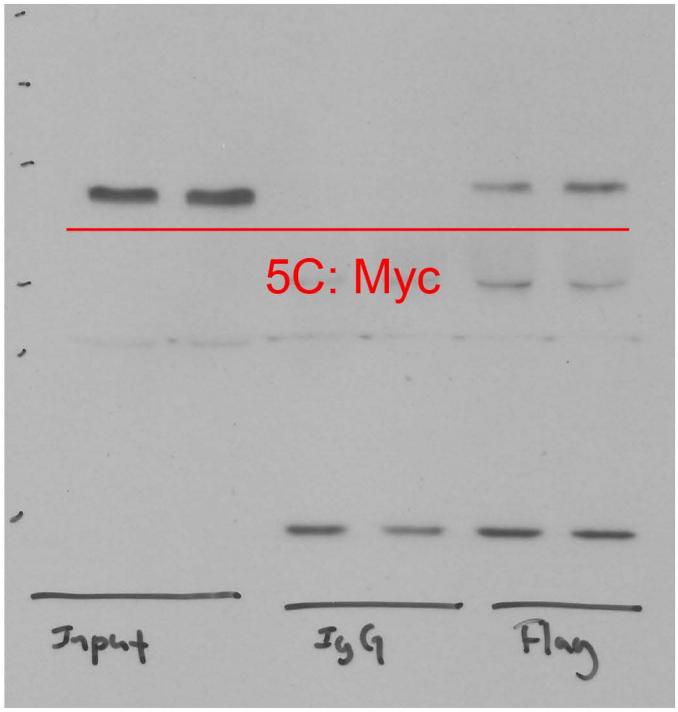

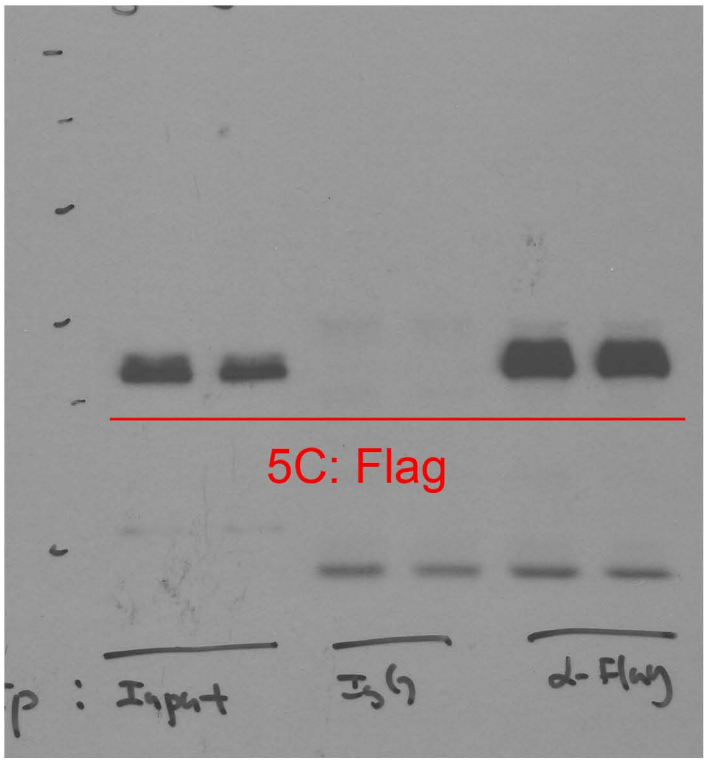

Full unedited gel for Figure 5C

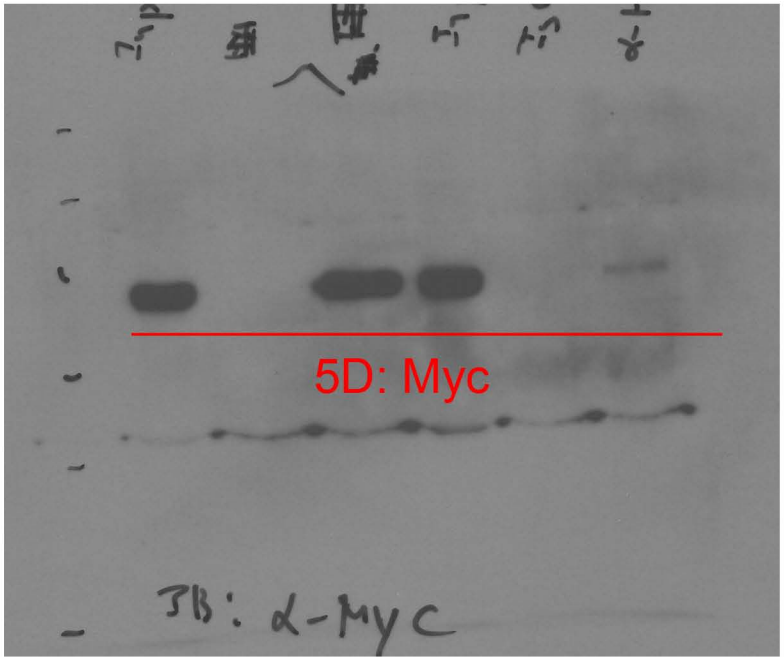

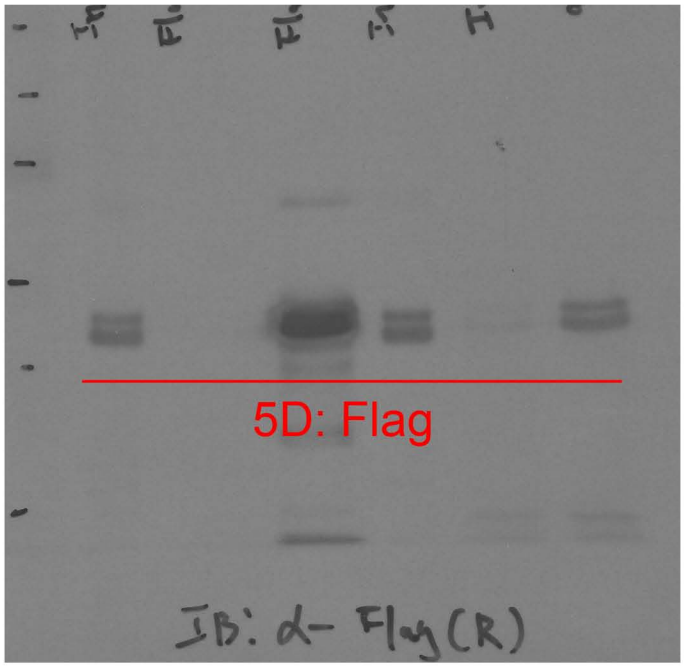

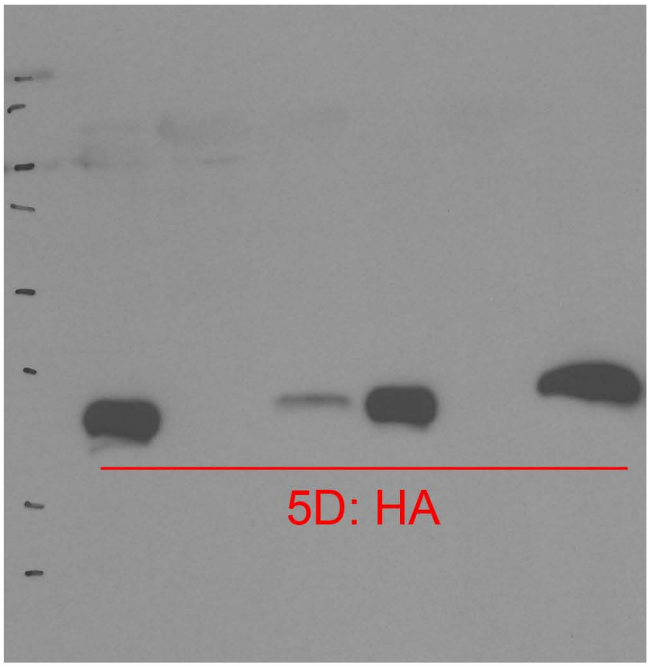

Full unedited gel for Figure 5D

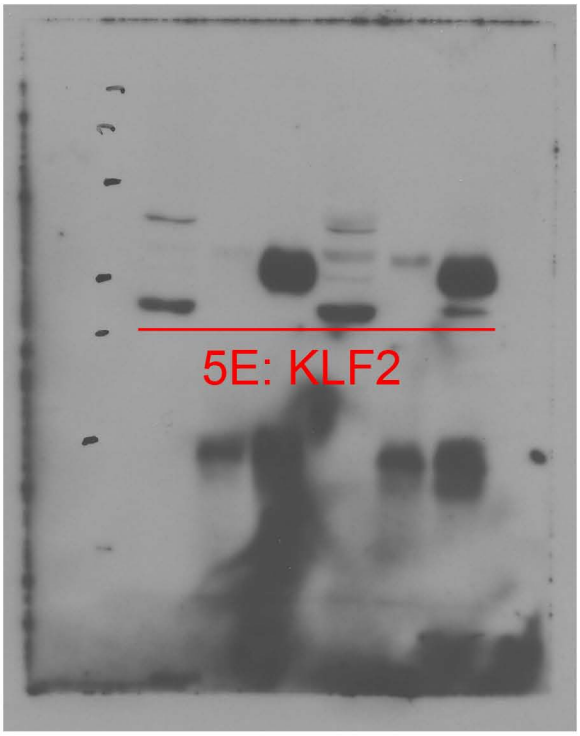

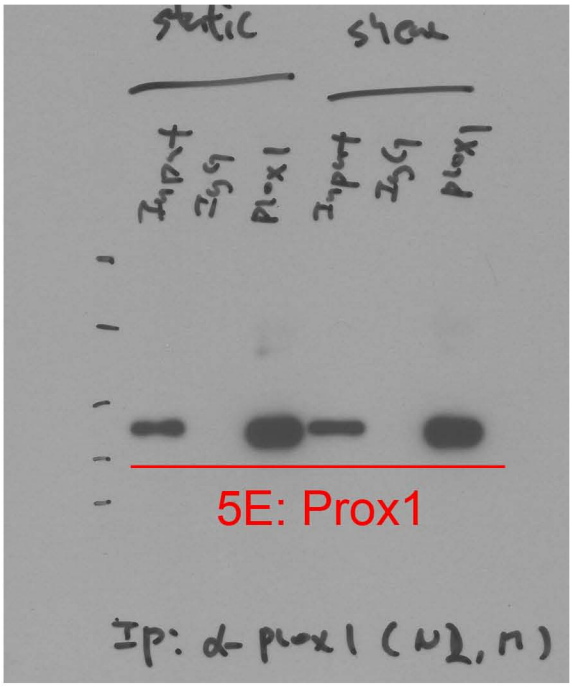

Full unedited gel for Figure 5E

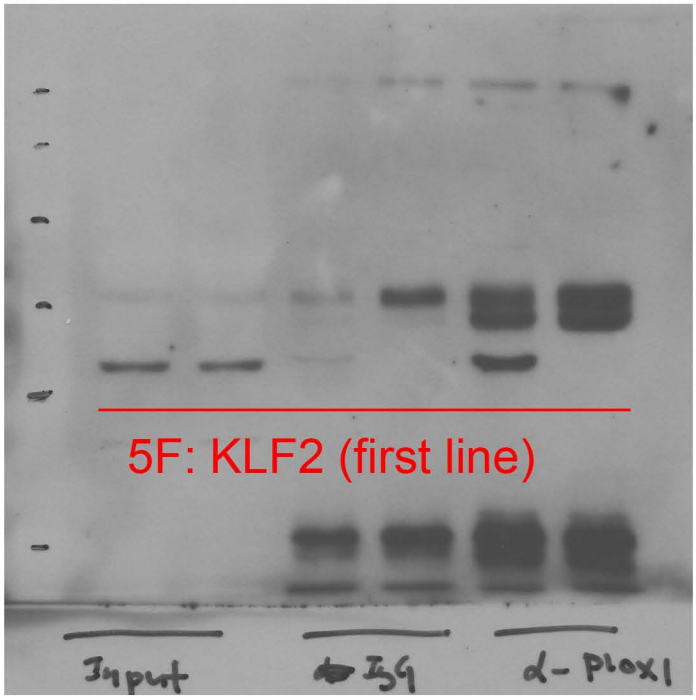

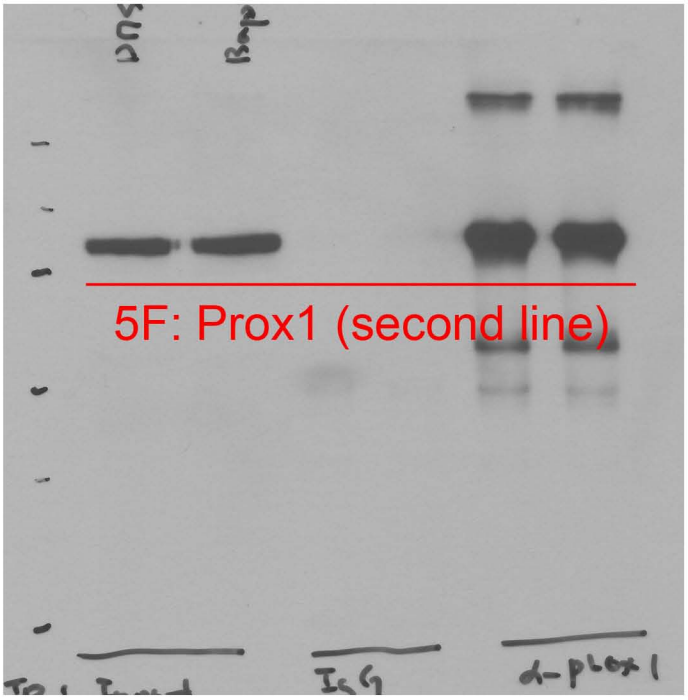

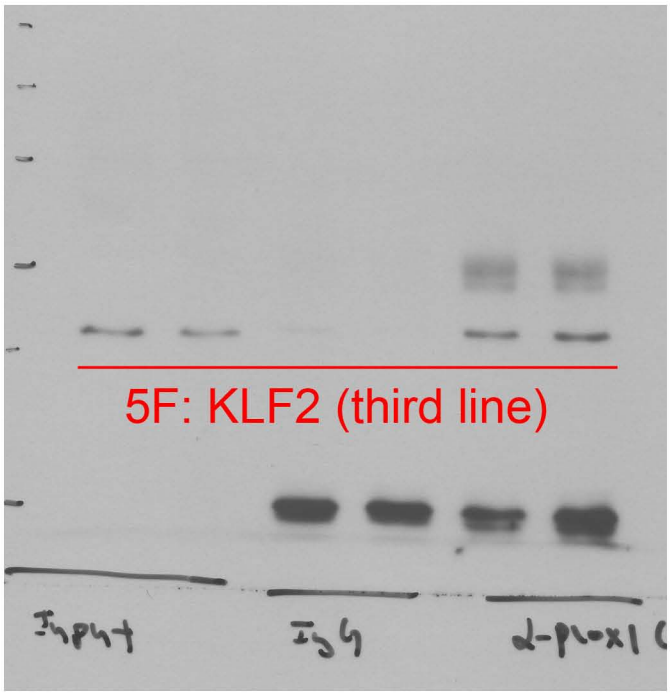

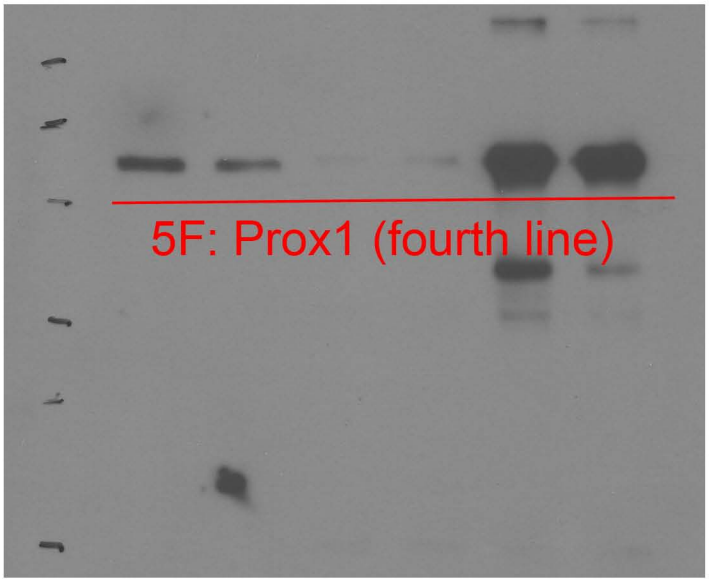

Full unedited gel for Figure 5F

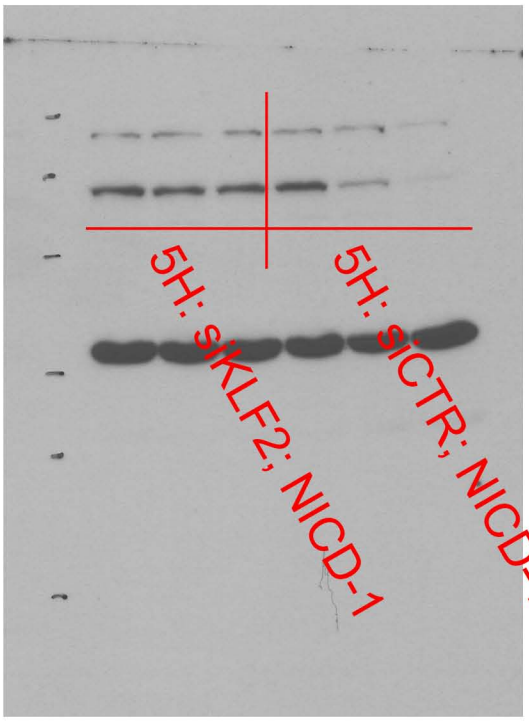

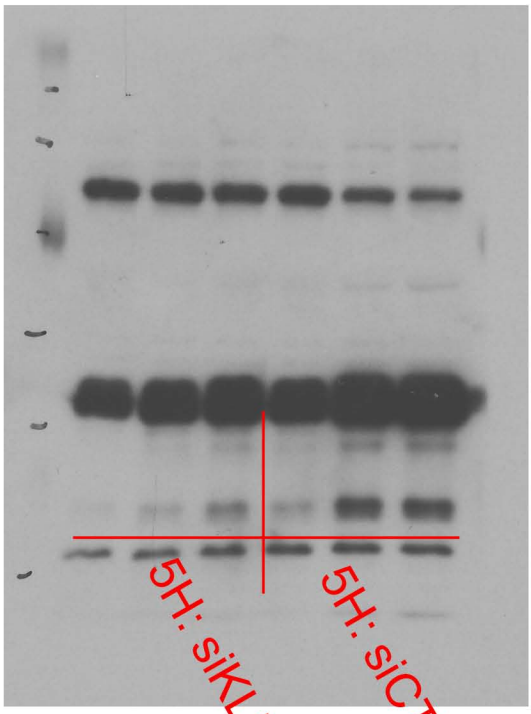

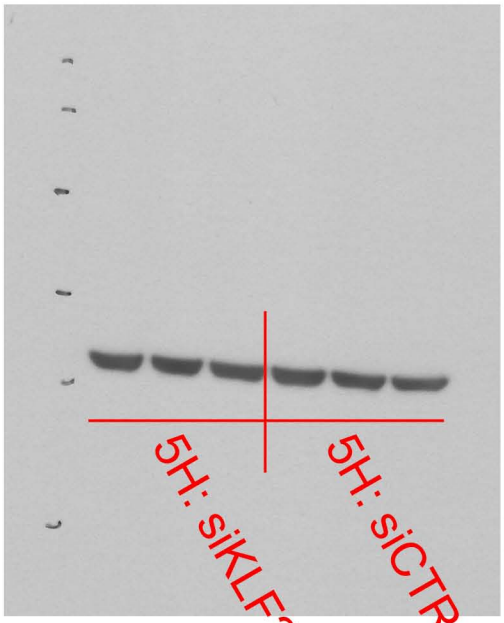

Full unedited gel for Figure 5H

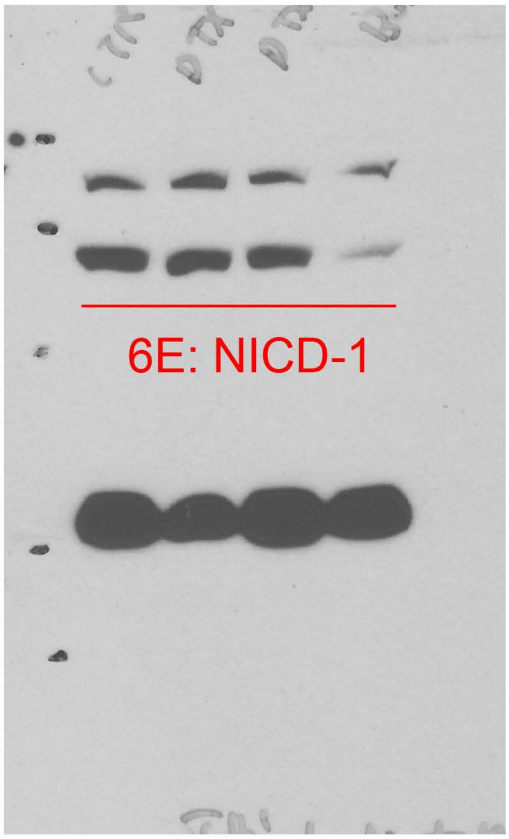

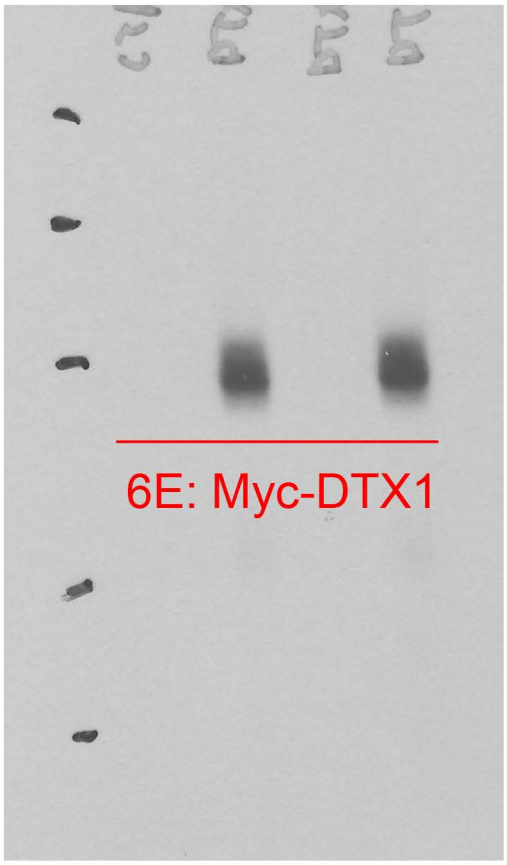

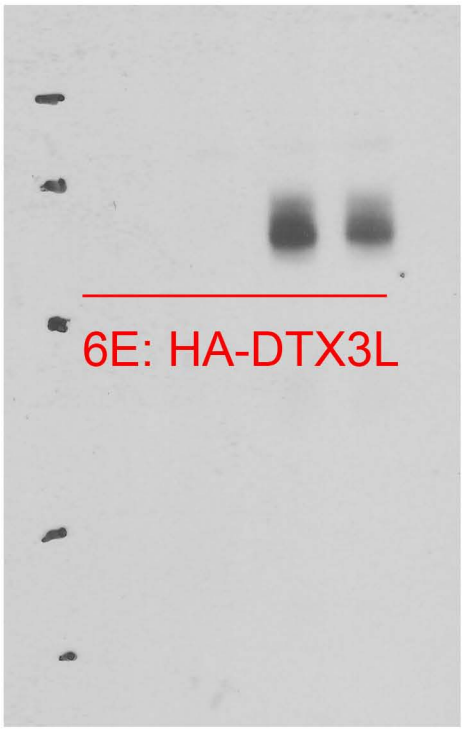

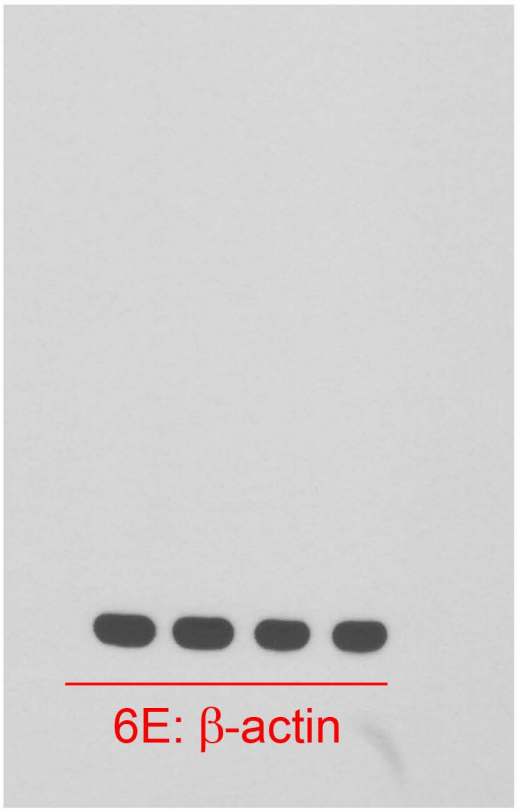

Full unedited gel for Figure 6E

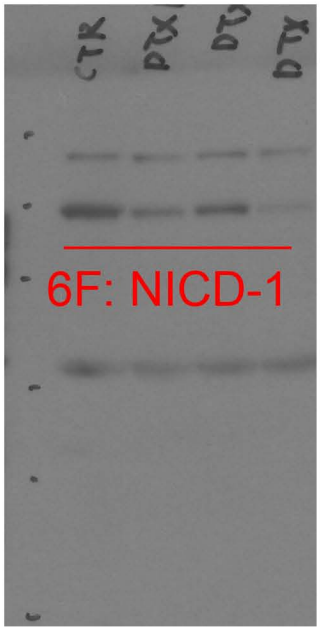

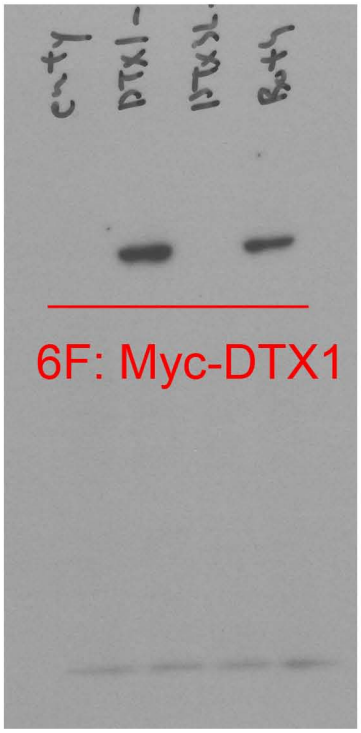

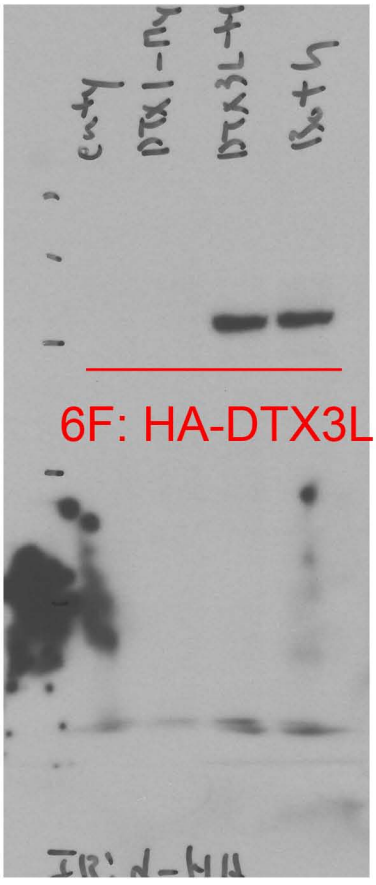

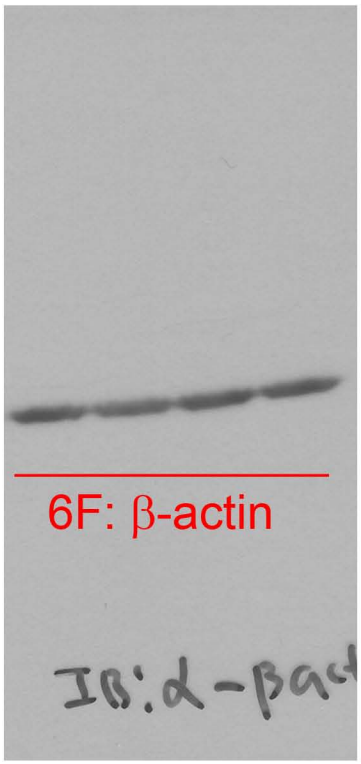

Full unedited gel for Figure 6F

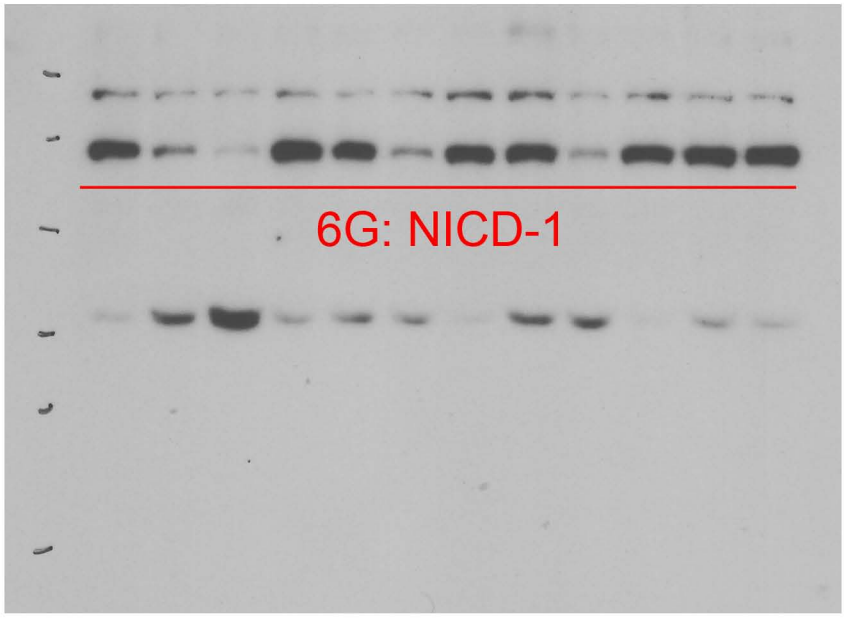

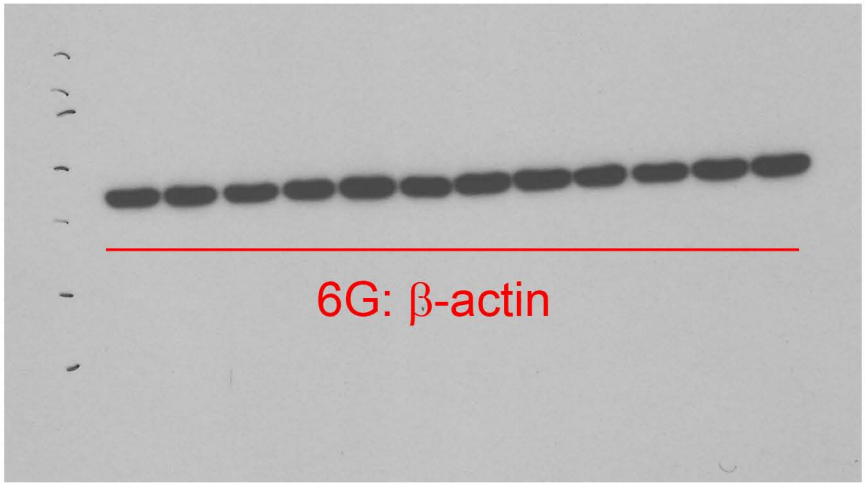

Full unedited gel for Figure 6G

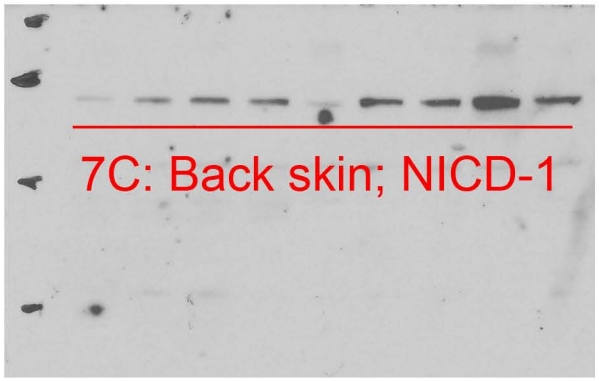

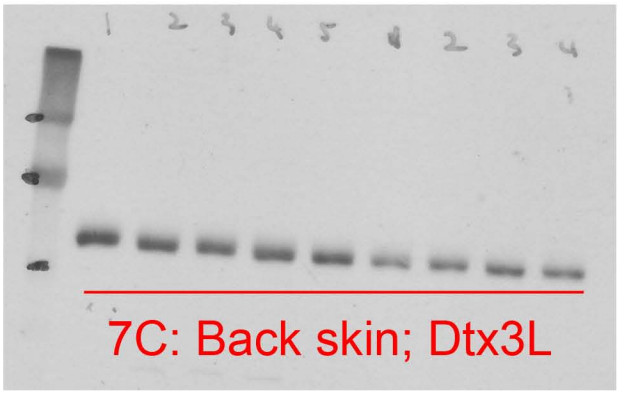

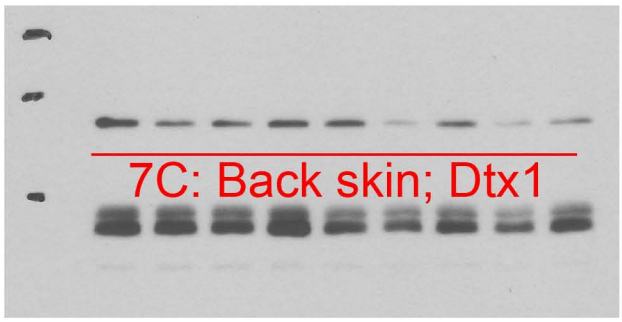

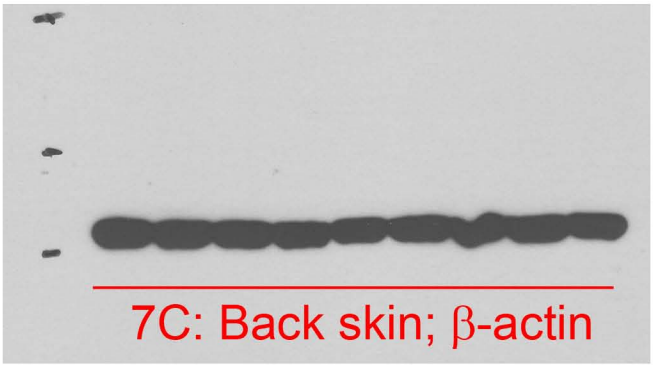

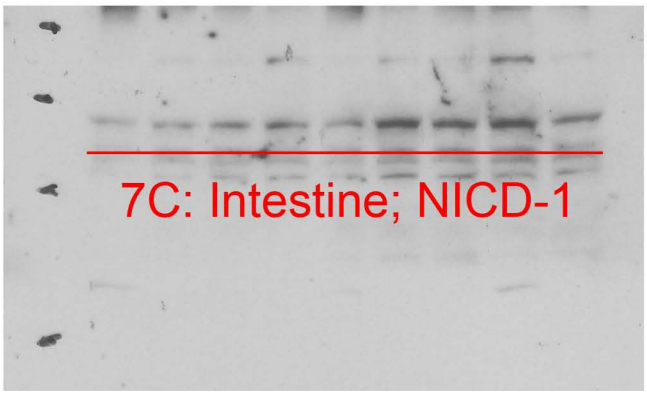

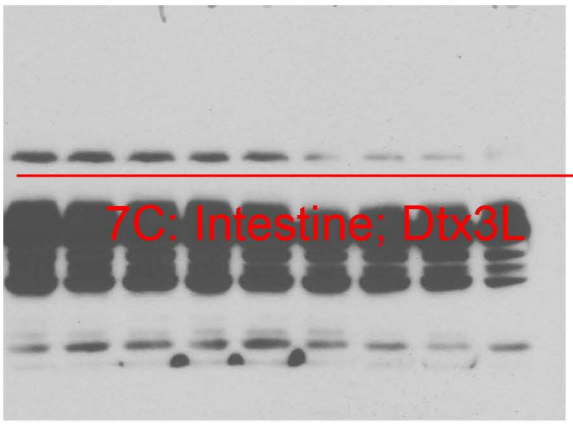

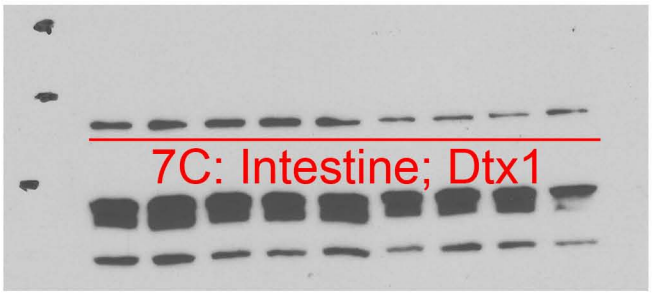

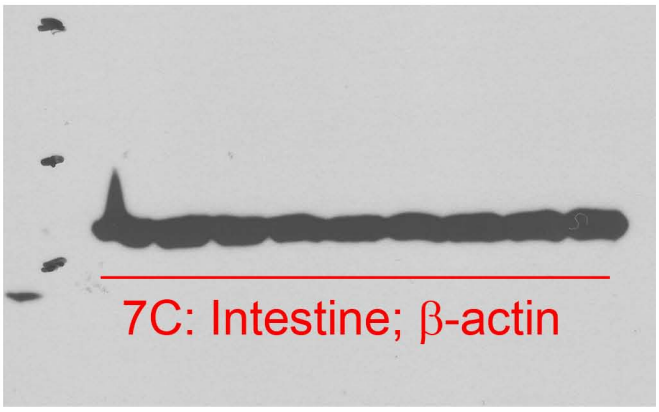

Full unedited gel for Figure 7C

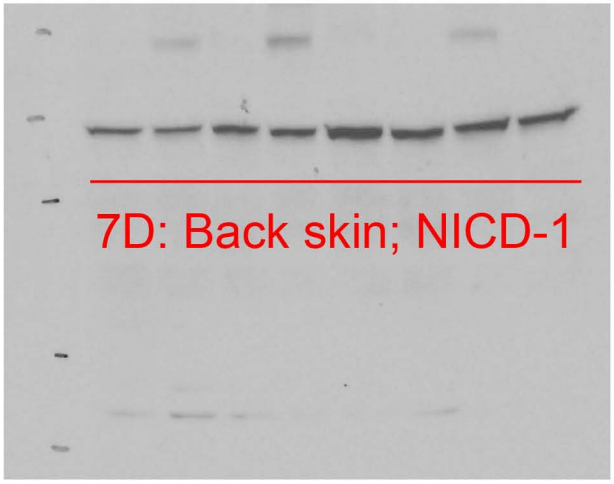

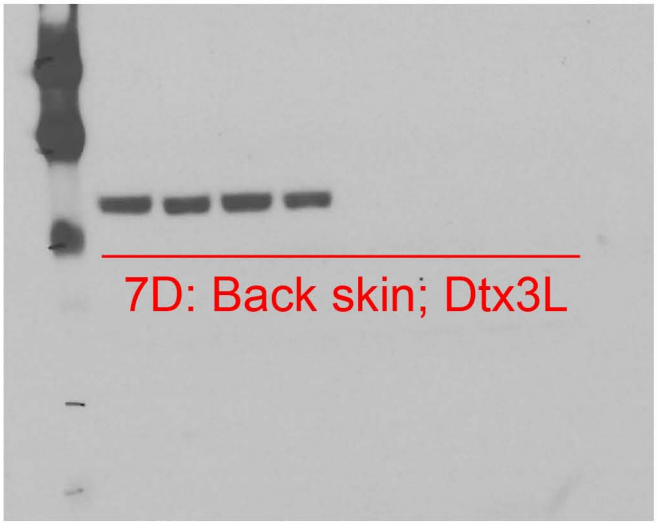

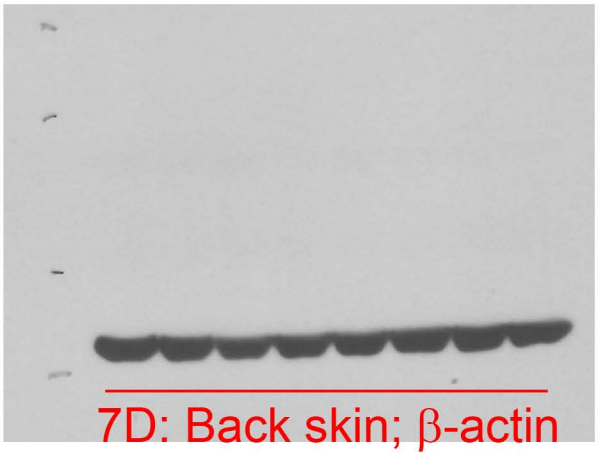

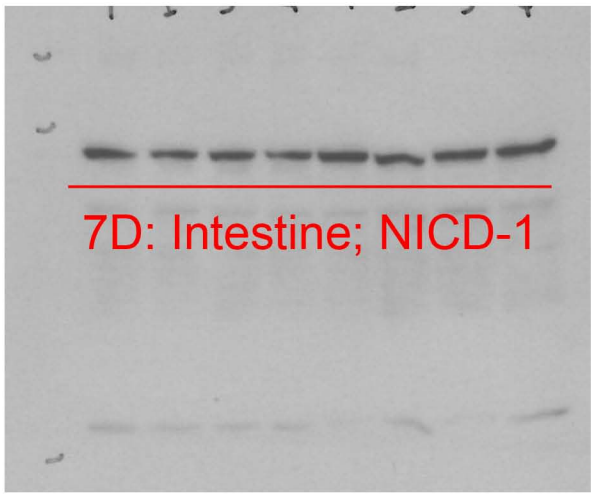

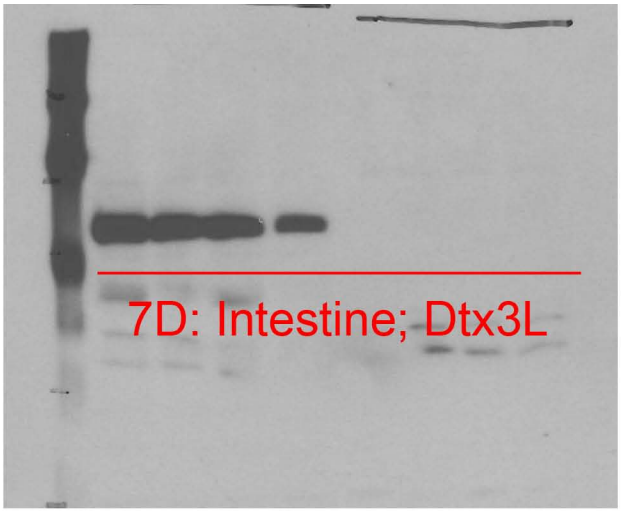

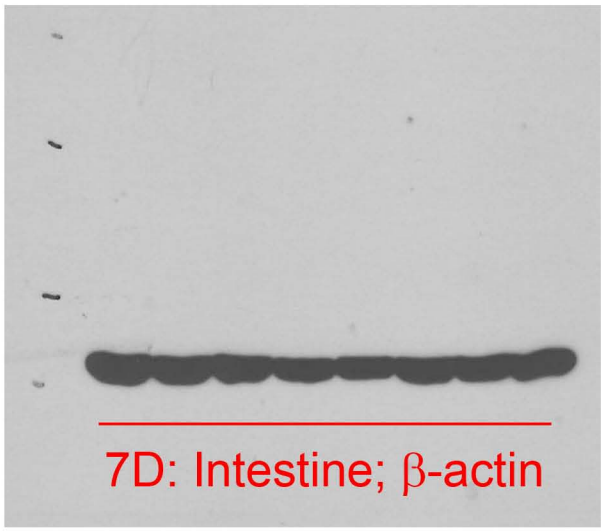

Full unedited gel for Figure 7D

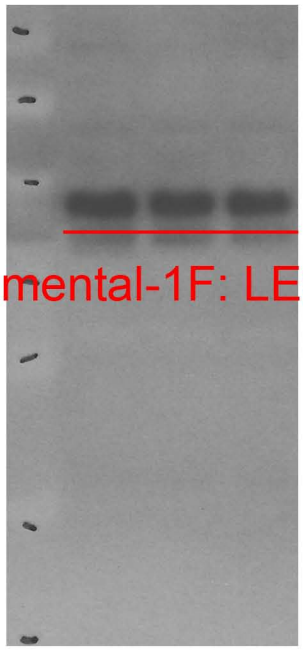

Supplemental-1F: LEC; NICD-4

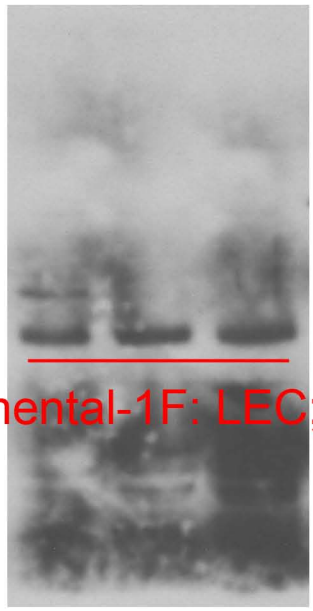

Supplemental-1F: LEC; β-actin

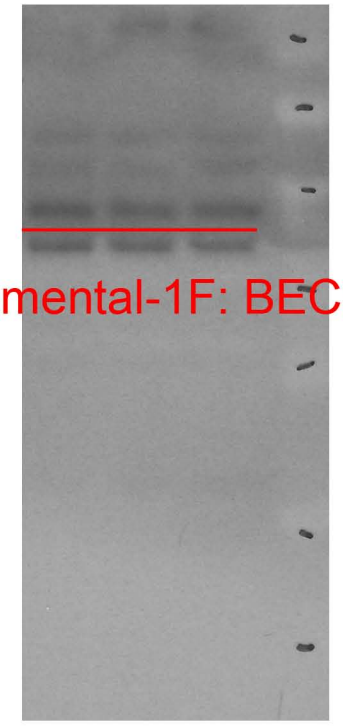

Supplemental-1F: BEC; NICD-4

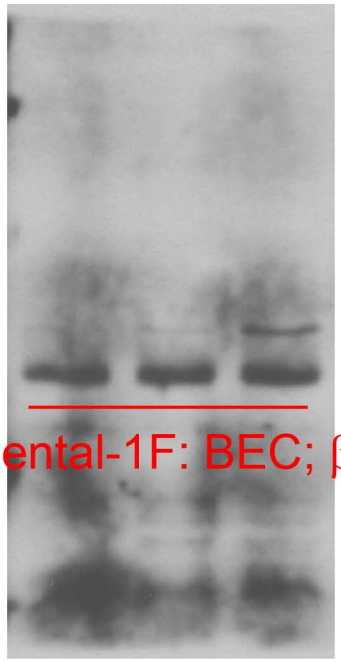

Supplemental-1F: BEC; β-actin

Full unedited gel for Supplemental Figure 1F

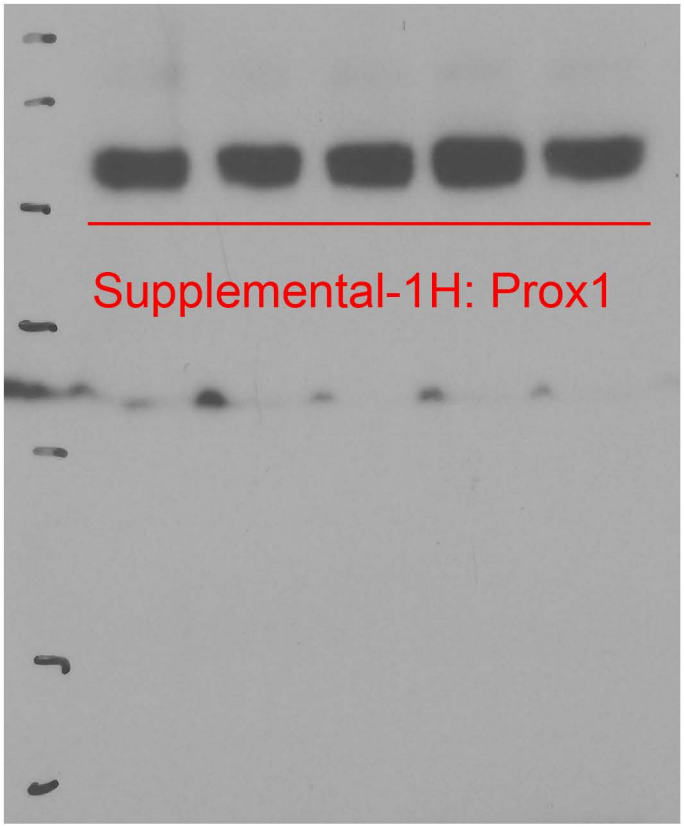

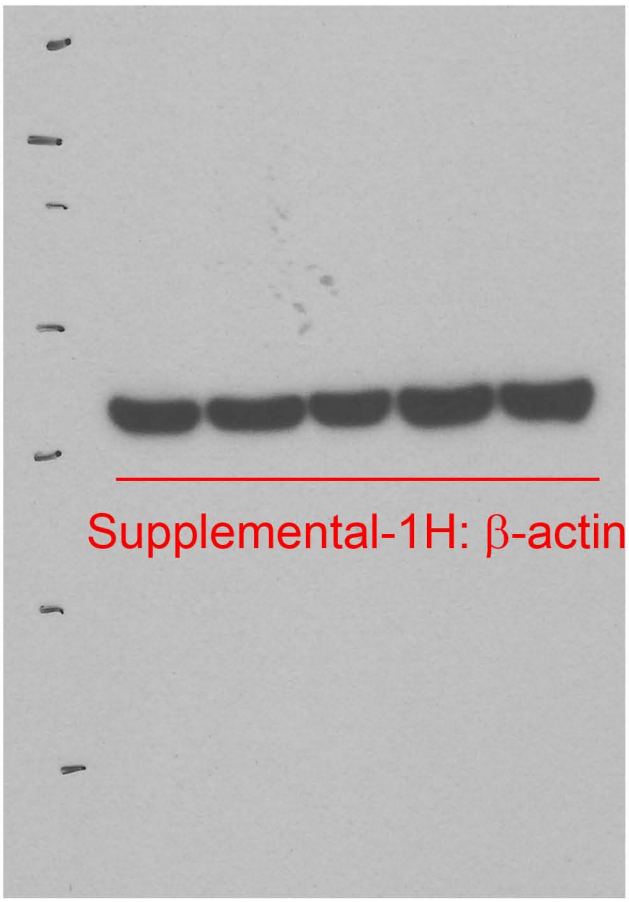

Full unedited gel for Supplemental Figure 1H

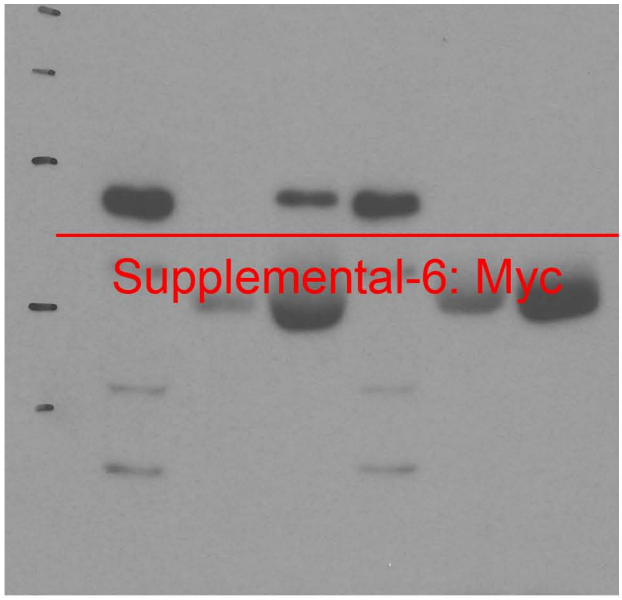

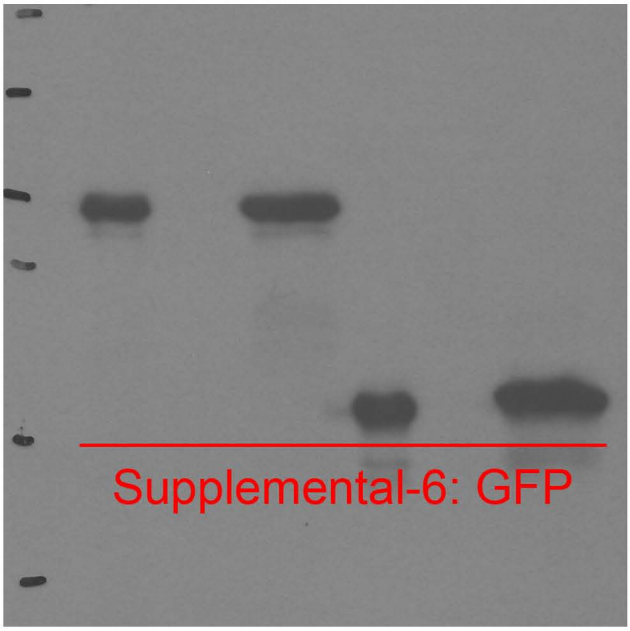

Full unedited gel for Supplemental Figure 6

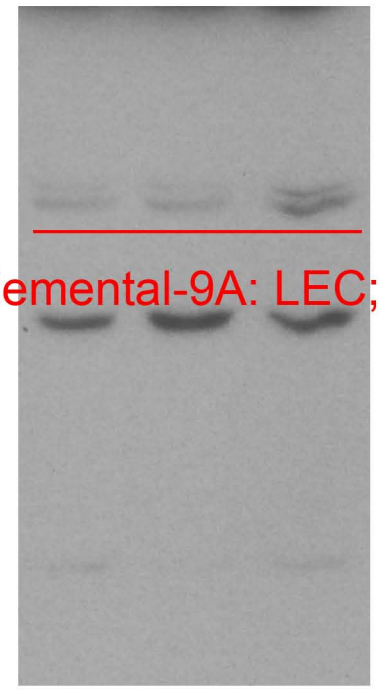

Supplemental-9A: LEC; DTX1

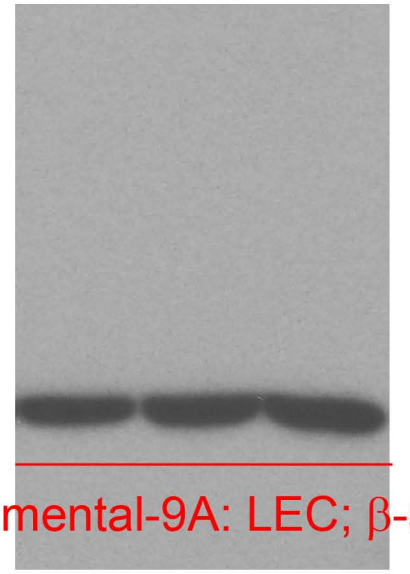

Supplemental-9A: LEC; β-actin

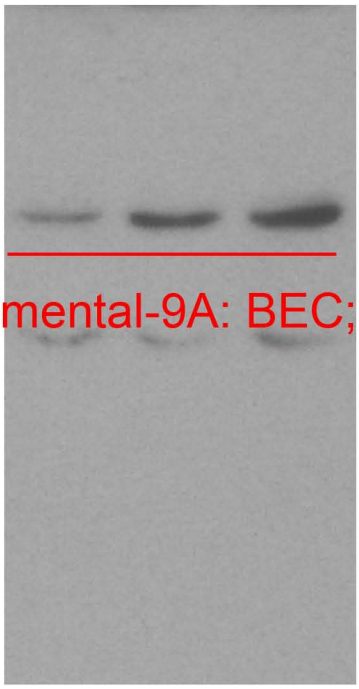

Supplemental-9A: BEC; DTX1

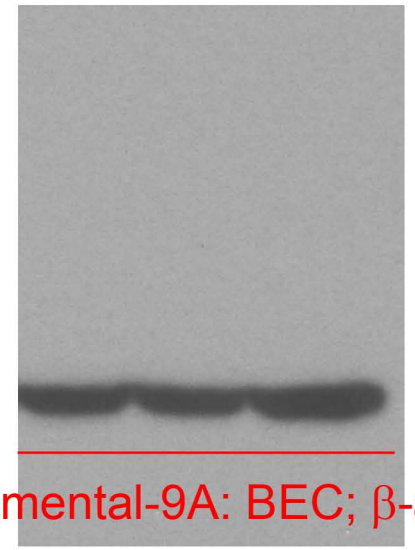

Supplemental-9A: BEC; β-actin

Full unedited gel for Supplemental Figure 9A

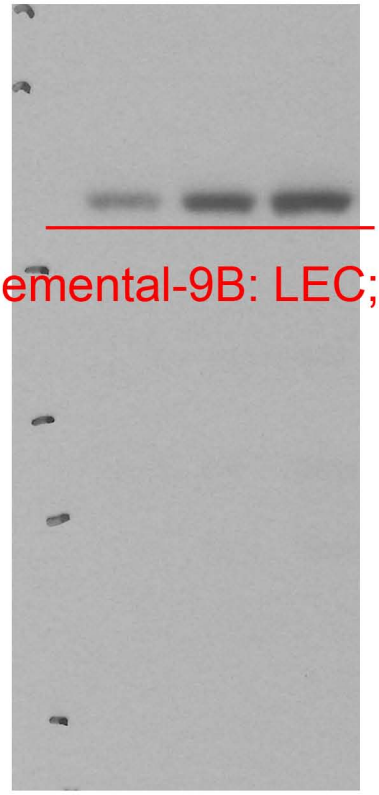

Supplemental-9B: LEC; DTX3L

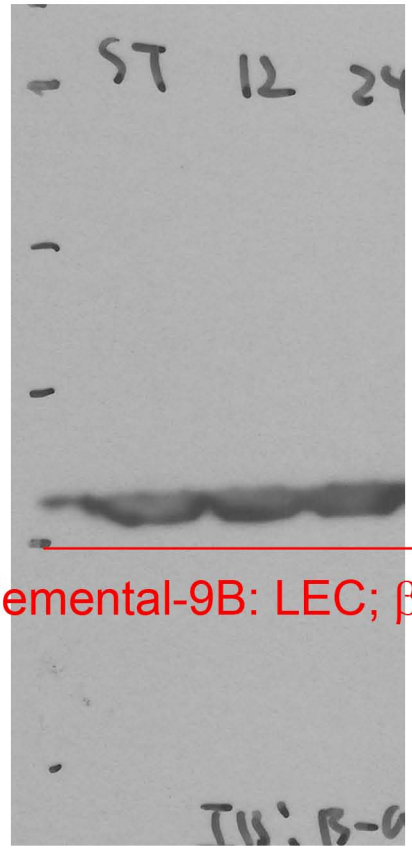

Supplemental-9B: LEC; β-actin

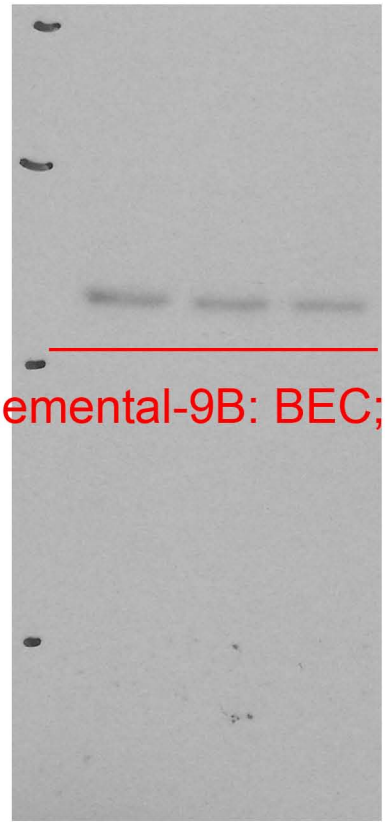

Supplemental-9B: BEC; DTX3L

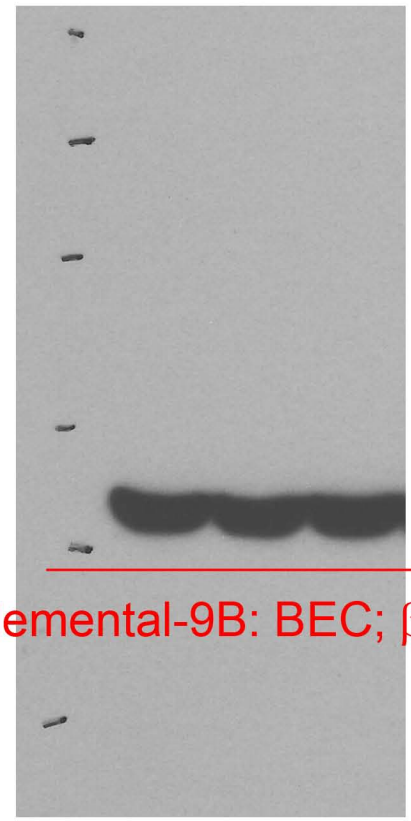

Supplemental-9B: BEC; β-actin

Full unedited gel for Supplemental Figure 9B